

Flow Instabilities of Dilute Surfactant Solutions in Elongational Deformations

zur Erlangung des akademischen Grades eines
DOKTORS DER INGENIEURWISSENSCHAFTEN (DR.-ING.)

von der KIT-Fakultät für Chemieingenieurwesen und Verfahrenstechnik des
Karlsruher Instituts für Technologie (KIT)
genehmigte

DISSERTATION

von
M. Sc. Steffen Michael Recktenwald
aus Landsweiler

Erstgutachter: Prof. Dr. Norbert Willenbacher
Zweitgutachter: Prof. Dr. Christian Wagner

Tag der mündlichen Prüfung: 18. Juni 2019

Preface

This thesis is mostly based on the manuscript *Heterogeneous flow inside threads of low viscosity fluids leads to anomalous long filament lifetimes* by Steffen M. Recktenwald, Simon J. Haward, Amy Q. Shen and Norbert Willenbacher, *Scientific Reports*, 9(1):7110, 2019 [1].

The major results described throughout this thesis were previously published in the aforementioned publication [1] and are extended by additional paragraphs to improve the comprehensibility and to provide additional background information here. In particular, Figs. 3.4, 4.2, 4.5, 4.6, 5.1, 5.5, 5.6, 5.7, 5.8, 5.10, 5.11, 5.12, 6.4, 6.5, 6.7, 7.1, and 8.4, which were part of the publication [1] are reproduced with permission from Springer Nature Publishing AG.

For the reason of better readability, tenses used in the publication [1] are maintained and the term *we* is used throughout this thesis.

Acknowledgements

In the fall of 2011, I participated in the lecture *Rheology and Rheometry* during my undergraduate studies at Karlsruhe. This was the first time I encountered the term *rheology* and I well remember my astonishment when the lecturer, Dr. Bernhard Hochstein, mentioned that fluids can have a *memory* - a fact that I did not understand in this first lesson but which fascinated me to begin my adventure in the field of *rheology*.

Seven years later, this thesis highlights the *zenith* of that endeavor and summarizes the main accomplishments of my time at the Karlsruhe Institute of Technology (KIT), Institute for Mechanical Process Engineering and Mechanics, in the Applied Mechanics (AME) group of Prof. Dr. Norbert Willenbacher during January 2015 and December 2018. I express my appreciation to the people who accompanied and supported me during my time in Karlsruhe.

- Principally, I wish to dedicate this work to my family - my wife Jana and my parents Margrit and Nikolaus. No words can express my deepest gratitude for their support.
- I am greatly indebted to my colleagues with whom I have been privileged to work. During my four years in the AME group, I had the chance to enjoy the company of a lot of interesting people, pursuing their PhD. I will miss the lunches, coffee breaks and fun times at conferences with Ceren Yüce, Katharina Hartung, Annika Völp, Moritz Weis and Ronald Gordon, and I am grateful for all the good memories with my dear office colleagues Annika Hodapp, David Menne and Walter Oswald in R217. Especially, I'd like to thank my colleague Johanna Roether, who did not only patiently listen to my research problems in the lab but who always had a sympathetic ear for me in our flat in the evenings or at our favorite bar. Furthermore, I thank Dr. Bernhard Hochstein for arousing my interest in rheology and for helping me on countless technical as well as organizational questions over the years. *Merci* to Dr. Claude Oelschlaeger, whose experience with surfactant solutions helped me particularly during the beginning of my PhD. It was a great pleasure and a unique experience to work in such a professional, yet always friendly environment - I am grateful to have been a part of the AME family!
- Prof. Dr. Norbert Willenbacher offered me the opportunity to perform my research in his institute and to become a part of the AME group. I thank him for the mentoring and for supervising this thesis. I am especially grateful for the freedom he provided during my PhD, to pursue the aspects of research that interested me

the most. Furthermore, he initiated and supported my research stay in Japan - an experience that significantly broadened my scientific as well as my personal horizon. Thank you, Norbert!

- I gratefully acknowledge Prof. Dr. Christian Wagner from Saarland University for his interest in my work and for kindly taking charge as the second reviewer of my thesis. I am looking forward to fruitful future projects!
- Between September and November 2017, I spent a three-month internship in the Micro/Bio/Nanofluidics Unit of Prof. Amy Shen at the Okinawa Institute of Science and Technology (OIST), Japan. I am very grateful to have been a part of Shen Unit and it was a great opportunity to learn new experimental methods in a unique research environment in beautiful Okinawa. I felt very welcomed as a member of the group from the first moment, and it was an extraordinary experience to work with people from all over the globe. Particularly, I am thankful for the help and input of Dr. Simon Haward during my time at OIST and thereafter. His enthusiasm for research improved my scientific approaches substantially.
ありがとうございます
- Last but not least, I appreciate the help of my students Kevin Tedjokusuma, for helping with CaBER experiments, Estelle Nasr, for performing filament stretching and falling drop measurements, and Driss Kaddar, for his MATLAB skills. Furthermore, I am thankful to Lukas Böni from ETH Zürich for generously providing a hagfish mucus sample.

This project was funded by the Deutsche Forschungsgemeinschaft under DRG grant number WI3138/22-1.

The three month research internship at the Okinawa Institute of Science and Technology (OIST), in the Micro/Bio/Nanofluidics Unit of Prof. Amy Shen from September 2017 to November 2017, was financially supported by the Karlsruhe House of Young Scientists (KYHS), Karlsruhe Institute of Technology, via the Research Travel Grant.

Abstract

Formation and breakup of fluid threads are pervasive in nature and technology. Water dripping from a leaking faucet forms a slender fluid thread, which quickly disintegrates into separate drops, while honey dripping from a spoon or melted cheese sometimes form long filaments. In many industrial applications, such as atomization, spraying, jetting and dripping processes, high extensibility of fluid filaments and extended filament lifetimes are commonly observed as a consequence of fluid viscoelasticity. In contrast, threads of low viscous Newtonian fluids like water rupture quickly. However, in this study we observe unusually long filament lifetimes, on the order of several minutes, of low viscosity fluids that cannot be explained by conventional approaches, based on their material properties such as viscosity and surface tension. We study this phenomenon, focusing on the formation and breakup of filaments of dilute surfactant solutions as model systems, and demonstrate how a unique banding instability inside liquid threads can lead to extremely long filament lifetimes and to the formation of remarkably long threads.

Surfactants are omnipresent in our everyday life due to their unique ability to spontaneously self-assemble into various complex mesoscopic structures. In our lungs, pulmonary surfactants adsorb to the air-water interface of the alveoli and reduce the surface tension to enable gas exchange. Furthermore, surfactants are used in many home and personal care products, such as soap, shampoo, cosmetics, and detergents, as well as in sophisticated industrial applications such as drag reducing agents and as fracture fluids in enhanced oil and gas recovery. Many of these applications and processes exhibit complex flow fields with strong elongational components, where structural transitions and flow instabilities can occur, thus leading to a dramatic change of the flow behavior.

In this study, we use dilute surfactant solutions as model systems to investigate such phenomena in elongational flow fields. Dilute surfactant solutions with low surfactant concentration, but well above the first critical micelle concentration, and low concentration of salt as additive consist of small, rigid, rodlike aggregates and their behavior in shear flow is well documented. In steady shear experiments, such systems can exhibit a zero shear viscosity close to that of water and no measurable elasticity. However, beyond a critical shear rate and critical total deformation, dilute surfactant solutions show a shear-thickening transition, where the viscosity increases by more than one order of magnitude due to the formation of so-called shear-induced structures. In the characteristic S-shaped regime of the non-monotonic flow curve, a flow instability emerges, where multiple bands, bearing different stresses and internal structures at one imposed shear rate, are stacked along the vorticity direction. Hence this type of flow instability is termed vorticity banding. Although the flow behavior of dilute surfactant

solutions is well understood experimentally as well as theoretically in shear flow, little is known about flow instabilities of these systems in extensional flows.

Here, we focus on uniaxial elongation as well as on planar extension of surfactant solutions, using a combination of microfluidic devices and various optical detection techniques. In uniaxial extension, we employ capillary breakup elongational rheometry (CaBER) as well as filament stretching and dripping-onto-substrate (DoS) experiments, in order to investigate the macroscopic filament breakup of these low viscosity fluids. In CaBER and DoS experiments, we observe unusually long filament lifetimes of several minutes, orders of magnitudes larger than expected. This phenomenon is independent of stretching parameters as well as interfacial tension between the surfactant solutions and the surrounding medium. Further, these fluids form remarkably long filaments, with a length greater than 10 cm, in filament stretching experiments.

In an effort to shed light on the origin of the long filament lifetime and length, we employ particle image velocimetry (PIV) on horizontally stretched filaments, covering a broad surfactant and salt concentration. At small concentrations, an unexpected flow behavior emerges inside the filament. We discover a heterogeneous distribution of the axial velocity in the filament cross-section, with multiple flow bands in opposing axial direction. This anomalous flow occurs randomly in the whole filament cross-section and leads to an additional flow from the reservoir at the filament ends back into the filament, besides the expected surface tension driven flow from the filament towards its ends, resulting in huge global filament lifetimes. Increasing the surfactant and salt concentration leads to a uniform flow, with a homogeneous flow profile and a centrally located stagnation point, as expected for thinning viscoelastic threads. Employing this unique experimental method, we construct flow instability maps for some of the most studied surfactant systems and demonstrate that unusually long filament lifetimes, reported in recent literature, are due to a heterogeneously banded flow inside the filaments.

We further study this elongational flow instability using an optimized-shape cross-slot extensional rheometer (OSCER), combined with PIV and birefringence imaging techniques. The dilute surfactant solutions that exhibit a heterogeneously banded flow during uniaxial thinning also show a time-dependent flow instability in planar elongation. At a critical elongation rate, a single localized birefringent strand emerges, which starts to split into several bands, indicating multiple stresses at one global strain rate. This is the first experimental observation of such a multivalued relation between stress and deformation rate in extension that was recently predicted numerically. Subsequently, the flow field transitions from a steady symmetric towards a steady asymmetric state over time. The critical elongation rate and the critical total strain for this transition in OSCER measurements are also experienced by the solution during the initial step stretch in CaBER experiments.

Ultimately, we relate the critical conditions for the onset of a flow instability in extension to the hysteretic flow curve of the surfactant solutions in shear. Here, we find that the critical strain rate in OSCER experiments is in the shear-thickening regime of the flow curve, where a vorticity banding instability leads to a multivalued relation between stress and shear rate in the underlying constitutive flow curve. Thus, we reveal a new banding instability - termed *extensional vorticity banding* - that arises

in elongational flows and demonstrate that the occurrence of a flow instability in such solutions is a generic phenomenon, independent of flow kinematics.

This new paradigm offers a more general, unifying framework for future theoretical work and new numerical simulation approaches will be stimulated in that interdisciplinary field between fluid mechanics, physical chemistry and process engineering. The observed flow instability also sets new limits for evaluation of extensional viscosity or relaxation times from filament stretching experiments, employed to study technical processes such as drag reduction or fiber spinning, but also biophysical phenomena such as stretching and unraveling of DNA. Beyond the detailed investigations on surfactant solution behavior, we show that biopolymer solutions such as saliva and hagfish slime also exhibit heterogeneously banded flow during uniaxial extension. This indicates that this generic phenomenon applies to a broad range of materials, relevant for many different topical areas of physics, chemistry, and biology.

Zusammenfassung

Die Bildung und der Zerfall von Fluidfilamenten sind allgegenwärtige Prozesse in Natur und Technik. Wasser, welches von einem undichten Wasserhahn tropft, bildet einen feinen Flüssigkeitsfaden, der schnell in einzelne Tropfen zerfällt. Dahingegen bilden von einem Löffel tropfender Honig oder geschmolzener Käse lange Fäden. In vielen industriellen Anwendungen, wie beispielsweise bei der Zerstäubung, beim Versprühen und bei Bedüsung- oder Tropfprozessen, sind hohe Dehnbarkeiten von Flüssigkeitsfilamenten und lange Filamentlebenszeiten normalerweise als Konsequenz der Viskoelastizität des Fluides zu beobachten. Im Gegensatz dazu zerfallen Filamente aus niedrig viskosen, Newtonischen Fluiden wie Wasser rasch. In dieser Arbeit beobachten wir jedoch ungewöhnlich lange Filamentlebenszeiten von mehreren Minuten bei niederviskosen Flüssigkeiten. Diese können allerdings nicht mit den üblichen Ansätzen, basierend auf den Materialeigenschaften des Fluides (Viskosität und Oberflächenspannung), erklärt werden. Wir untersuchen dieses Phänomen, wobei wir den Fokus auf die Bildung und den Zerfall von Filament aus verdünnten Tensidlösungen als Modellsysteme legen und zeigen, wie eine neuartige Strömungsinstabilität in Flüssigkeitsfäden zu extrem langen Filamentlebensdauern und zur Bildung von außergewöhnlich langen Fäden führt.

Tenside sind aufgrund ihrer einzigartigen Eigenschaft, sich spontan in einer Vielzahl komplexer mesoskopischer Strukturen anzuordnen, in unserem Alltag weit verbreitet. In unseren Lungen adsorbieren pulmonale Tenside an die Luft-Wasser Grenzfläche der Alveolen und reduzieren hierdurch die Oberflächenspannung, um den Gasaustausch zu ermöglichen. Des Weiteren werden Tenside in Haushalts- und Kosmetikartikeln, wie Seife, Shampoo, Kosmetika und Waschmittel, sowie in hochentwickelten industriellen Anwendungen zur Verminderung des Strömungswiderstandes und in der Tertiären Öl- und Gasförderung, eingesetzt. Viele dieser Anwendungen und Prozesse weisen komplexe Strömungsfelder mit ausgeprägten Dehnanteilen auf, welche zu strukturellen Änderungen und Strömungsinstabilitäten im Fluid führen können, und somit das Fließverhalten dramatisch verändern.

In dieser Arbeit benutzen wir verdünnte Tensidlösungen als Modellsysteme, um solche Phänomene in Dehnströmungen zu untersuchen. Verdünnte Tensidlösungen mit niedriger Tensidkonzentration und niedriger Konzentration an Salz als Zusatzstoff bestehen aus kleinen, stäbchenförmigen Aggregaten, deren Fließverhalten in Scherung gut dokumentiert ist. In stetigen Scherexperimenten zeichnen sich solche Systeme durch eine Nullscherviskosität ähnlich wie die von Wasser und keine messbare Elastizität aus. Jedoch zeigt sich bei einer kritischen Scherrate und einer kritischen Gesamtdeformation scherverdickendes Verhalten. Hierbei steigt die Viskosität aufgrund der Bildung von scherinduzierten Strukturen über mehr als eine Größenordnung an. Im charakteris-

tischen s-förmigen Regime der nicht-monotonen Fließkurve tritt eine Fließinstabilität auf. Dabei entstehen bei einer Scherrate mehrere Bänder mit verschiedenen Spannungen und inneren Strukturen, die entlang der sogenannten *vorticity* Richtung geschichtet sind. Diese Strömungsinstabilität wird *vorticity banding* genannt. Obwohl das Fließverhalten von verdünnten Tensidlösungen in Scherung experimentell sowie theoretisch gut verstanden ist, sind Fließinstabilitäten dieser Systeme in Dehnströmungen weitestgehend unerforscht.

Im Mittelpunkt dieser Arbeit steht daher die uniaxiale sowie die planare Dehnbeanspruchung von Tensidlösungen. Hierbei werden mikrofluidische Apparate, sogenannten *microfluidics*, mit zahlreichen optischen Untersuchungsmethoden kombiniert. In uniaxialer Dehnung werden die *capillary breakup elongational rheometry* (CaBER) sowie *dripping-onto-substrate* (DoS) Experimente eingesetzt, um die makroskopische Filamentbildung und den anschließenden Zerfall dieser niedrig viskosen Fluiden zu untersuchen. In CaBER und DoS Messungen werden ungewöhnlich lange Fadenlebensdauern von mehreren Minuten beobachtet, mehrere Größenordnungen länger als erwartet. Dieses Phänomen ist unabhängig von den Verstreckparametern, sowie der Grenzflächenspannung zwischen Tensidlösung und umgebender Phase. Weiterhin formen diese Fluide außergewöhnlich lange Läden in Fadenzug-Experimenten.

Um die Ursache der langen Fadenlebensdauer und der großen Filamentlänge aufzuklären, wenden wir die sogenannte *particle image velocimetry* (PIV) Methode auf horizontal verstreckte Filament an und decken eine breite Tensid- sowie Salzkonzentration ab. Bei kleinen Konzentrationen tritt hierbei ein überraschendes Strömungsverhalten im Filament auf. Wir entdecken im Filamentquerschnitt eine heterogene Geschwindigkeitsverteilung, mit mehreren Strömungsschichten in entgegengesetzte Richtung. Dieses ungewöhnliche Fließen tritt zufällig im gesamten Fadenquerschnitt auf und führt zu einem Rückströmen von den Reservoirs am Ende des Filaments zurück in den Faden. Dies findet neben dem, aufgrund der Oberflächenspannung zu erwarteten, Strömen vom Filament in die Reservoirs statt und resultiert in ungewöhnlich langen Filamentlebenszeiten. Wird die Tensid- oder die Salzkonzentration erhöht, führt dies zu einem gleichmäßigen Fließen. Hier bildet sich ein homogenes Strömungsprofil mit einem zentralen Stagnationspunkt in der Filamentmitte aus, wie erwartet für die Verjüngung viskoelastischer Fäden. Mit Hilfe dieser einzigartigen Messmethode konstruieren wir Instabilitätsdiagramme für einige der bekanntesten Tenside und zeigen, dass ungewöhnlich lange Filamentlebenszeiten auf ein heterogenes Strömen im Faden zurückzuführen sind.

Des Weiteren untersuchen wir diese Dehn-Fließinstabilität mittels eines sogenannten *optimized-shape cross-slot extensional rheometer* (OSCER), in Kombination mit PIV sowie mit Methoden zur Visualisierung der Doppelbrechung. Verdünnte Tensidlösungen, welche ein heterogenes Fließen während der uniaxialen Verjüngung im Filament aufweisen, zeigen hier eine zeitabhängige Strömungsinstabilität in planarer Dehnung. Bei einer kritischen Dehnrate entsteht ein doppelbrechender Strang, welcher sich in mehrere einzelne Stränge aufspaltet. Dies weist auf mehrere Spannungen bei einer globalen Dehnrate hin. Diese erste experimentelle Beobachtung eines solchen mehrwertigen Zusammenhangs zwischen Spannung und Deformationsrate in Dehnung wurde kürzlich aufgrund numerischer Berechnungen vorhergesagt. Des Weiteren kommt es zu einem zeitabhängigen Übergang des stetigen, symmetrischen Strömungsfeldes hin

zu einem stetigen asymmetrischen Zustand. Die kritische Dehnrate und die kritische Gesamtdehnung für diesen Übergang im OSCER werden auch bei der Fadenverstreckung in CaBER Experimenten erreicht.

Letztendlich verknüpfen wir diese kritischen Bedingungen für das Auftreten einer Strömungsinstabilität in Dehnung mit der hysteretischen Fließkurve der Tensidlösungen in Scherung. Dabei stellt sich heraus, dass die kritische Dehnrate in OSCER Experimenten im scherverdickendem Regime der Fließfunktion liegt. Hier führt die *vorticity banding* Instabilität ebenfalls zu einer mehrwertigen Beziehung zwischen Spannung und Scherrate. Wir decken somit eine neue Fließinstabilität in Dehnung auf – das sogenannte *extensional vorticity banding* – und zeigen, dass das Auftreten einer Strömungsinstabilität in solchen Lösungen ein generisches Phänomen ist, das unabhängig von der Strömungskinematik auftritt.

Dieses neue Paradigma liefert eine generalisierte, vereinheitlichende Betrachtungsweise für zukünftige theoretische Arbeiten. Zudem werden hierdurch neue numerische Simulationen im interdisziplinären Spannungsfeld zwischen Strömungsmechanik, Physikalischer Chemie und Verfahrenstechnik angeregt. Die entdeckte Fließinstabilität setzt auch neue Limitierungen für die Bestimmung der Dehnviskosität sowie der Dehnrelaxationszeit aus Fadenverstreck-Experimenten. Diese werden häufig angewendet um sowohl technische Prozesse, wie beispielsweise die Minderung des Strömungswiderstandes oder das Faserspinnen, zu studieren, als auch, um biophysikalische Phänomene, wie die Verstreckung und das Entschlaufen von DNA Molekülen, zu untersuchen. Neben den detaillierten Untersuchungen der Tensidlösungen, zeigen wir außerdem, dass Biopolymerlösungen, wie Speichel oder Schleimaalsekret, während uniaxialer Dehnung ebenfalls heterogenes Fließen im Faden zeigen. Dies deutet darauf hin, dass dieses generische Phänomen für eine breite Klasse von Materialien gilt und somit relevant ist für viele verschiedene Forschungsbereichen der Physik, Chemie und Biologie.

Contents

Acknowledgements	iii
Abstract	v
Zusammenfassung	ix
1 Introduction	1
2 Theoretical Background	5
2.1 Surfactants - from single molecules to micellar aggregates	5
2.2 Flow and deformation of surfactant solutions	7
2.2.1 Shear rheology	8
2.2.2 Elongational deformation	13
2.2.3 Flow instabilities in surfactant solutions	20
2.3 Conclusions	24
2.3.1 Research objectives, scope and limitations	25
3 Materials	27
3.1 Surfactant systems and sample preparation	27
3.2 Shear rheological characterization	28
3.2.1 Steady shear measurements	28
3.2.2 Shear-induced structure formation	29
3.2.3 Linear viscoelastic properties of dilute surfactant solutions	31
3.3 Conclusions	32
4 Filament Formation and Breakup in Uniaxial Extension	33
4.1 Experimental	33
4.1.1 Capillary breakup elongational rheometry	33
4.1.2 Dripping-onto-substrate and filament stretching experiments	34
4.2 Results and discussion	35
4.2.1 Filament thinning in CaBER	35
4.2.2 Influence of stretching conditions and surrounding phase on filament thinning behavior	37
4.2.3 Formation of long surfactant filaments	39
4.3 Conclusions	42

5	Flow Inside Thinning Surfactant Filaments	45
5.1	Experimental	45
5.1.1	Flow field measurements during horizontal filament thinning	45
5.1.2	Homogeneous uniaxial elongation of viscoelastic fluids	47
5.2	Results and discussion	51
5.2.1	Heterogeneous flow of dilute solutions	51
5.2.2	Uniform extension of high concentrated solutions	54
5.2.3	Flow behavior phase diagrams	57
5.3	Conclusions	59
6	Planar Elongational Deformation of Surfactant Solutions	63
6.1	Experimental	63
6.1.1	The OSCER - flow in planar elongation	63
6.1.2	Stagnation point flow of Newtonian fluids	65
6.2	Results and discussion	67
6.2.1	Time-dependent flow instability of dilute solutions	67
6.2.2	Elastic flow instability of high concentrated solutions	71
6.3	Conclusions	74
7	Discussion - Flow Instabilities of Dilute Surfactant Solutions in Different Flow Kinematics	75
8	Summary and Outlook	79
8.1	Future prospects	81
8.2	Flow inside biopolymeric fluid filaments	83
9	Bibliography	87
	Appendix	103

1 Introduction

When you put a drop of saliva between your thumb and index finger, then slowly pull your fingers apart, a slender fluid thread forms. This filament starts to thin, eventually forming a periodic pattern of small beads connected by small threads, before it finally breaks. This simple experiment shows how complex fluids like saliva, which contain naturally occurring polymers that cause viscoelasticity, respond to stretching or elongational deformation. The breakup of complex fluid threads is a dynamical process, omnipresent in nature and highly relevant for many technological operations such as atomization and spraying [2], electrospinning [3], or roll-coating [4].

The progressive thinning of free fluid filaments in uniaxial extension was extensively studied in the past decades. Generally, filament thinning is driven by capillarity and resisted by inertia as well as viscous and elastic stresses inside the filament. Experimental techniques, such as the capillary breakup elongational rheometer (CaBER), are commonly used to study fluid response to elongational deformations. During uniaxial extension, polymer solutions and other viscoelastic fluids exhibit slow thinning processes and prolonged filament lifetimes up to several seconds, due to stretching of polymer chains and growth of extensional stresses inside the filament. On the other hand, low viscosity inelastic fluids such as water do not form long living filaments - instead, the fluid thread quickly breaks.

However, in this thesis, we study the breakup of low viscosity surfactant solutions and report a surprising phenomenon, as shown in Fig. 1.1. Here, a drop of aqueous surfactant solution, with a low shear viscosity close to water and no measurable viscoelasticity, drips from a nozzle and forms a remarkably long filament with a length much greater than 10 cm. This stunning phenomenon does not arise as a consequence of viscoelasticity of the solution as for other soft matter materials such as highly concentrated surfactant or polymer solutions. Another striking feature of such dilute surfactant solutions is the slow thinning process during CaBER measurements, where fluid threads exhibit unusually long filament lifetimes on the order of several minutes, as reported in recent studies [5, 6].

From CaBER experiments, fundamental fluid properties such as the extensional viscosity and extensional relaxation time are derived based on the assump-



Figure 1.1: Formation of a long surfactant filament, dripping from a nozzle.

tion of homogeneous elongation. However, flow instabilities can change the flow behavior dramatically and are ubiquitous during deformation of a wide variety of complex fluids including granular matter, suspensions, emulsions, foams, polymer solutions and melts, as well as aqueous surfactant solutions [7, 8, 9, 10, 11]. Particularly, flow instabilities of surfactant solutions in shear were extensively studied [12, 13], since these systems are pervasive in our everyday life. They are found in many home and personal care products, such as soap, cosmetics, shampoo and detergents [14], but also in sophisticated industrial applications such as drag reducing agents to reduce turbulence in petroleum pipelines [15, 16, 17, 18], and as fracture fluids in enhanced oil and gas recovery, where surfactant solutions are pumped into porous rocks [19, 20].

In solutions, surfactant molecules can self-assemble into various morphologies, depending on surfactant type and concentration, temperature and salinity [12]. Additives, such as salt, can promote anisotropic micellar growth, resulting in the formation of long, semi-flexible wormlike micelles (WLM) that entangle and cause viscoelasticity at high surfactant and salt concentrations. These solutions are often used as model systems to study instabilities of complex fluids, mainly focusing on their flow behavior in shear. On the other hand, surfactant solutions with low surfactant and salt concentrations, such as the sample shown in Fig. 1.1, consist of small rod-shaped micellar aggregates [21]. In shear flow, these solutions are known to exhibit flow-induced structural changes that lead to dramatic changes of the flow behavior as well as to flow instabilities. However, little is known about such phenomena in extension, despite the omnipresence of elongational flow fields in nature as well as in many technical processes and applications. So far, knowledge about the flow-induced structure buildup of dilute surfactant solutions and related banding instabilities particularly in extensional flow fields still remains vague, which allows us to discover a novel flow instability.

In this thesis, the generic observation shown in Fig. 1.1 motivates us to fill this gap in the literature by probing the extensional flow behavior of low viscosity fluids. Therefore we examine the macroscopic filament breakup as well as the microscopic flow behavior in uniaxial and planar elongation of dilute surfactant solutions as model systems that are known to exhibit various kinds of instabilities in shear flow. These were extensively discussed in numerous scientific publications from an experimental as well as a theoretical point of view. In an effort to understand how low viscosity fluids, such as the sample shown in Fig. 1.1, can form unusually long filament lengths and lifetimes, orders of magnitude larger than expected, we employ a unique experimental setup combining microfluidic devices and various optical detection techniques.

Structure of the thesis

This thesis is composed of the seven following chapters and will progressively elucidate the origin of the unusual flow behavior of dilute surfactant solutions in extension.

- Chapter 2 provides a brief introduction of the structure of micellar aggregates and the anisotropic growth of micelles. A detailed state-of-the-art understanding, regarding the flow behavior of surfactant systems in shear as well as in extension is presented. We review the most important rheological features, including banding instabilities, of surfactant solutions that contain short, rodlike or long, wormlike micelles. Finally, we define the research objectives of this thesis that are covered in the following chapters.
- In chapter 3, we present the materials used in this work. The flow behavior of these surfactant solutions in shear is discussed, focusing on steady shear measurements and on the shear-induced structure buildup in dilute solutions.
- Chapter 4 shows the results regarding the macroscopic filament formation and breakup of surfactant solutions in uniaxial extension. Here, the CaBER method is briefly introduced and the influence of stretching conditions and surrounding phase on the filament thinning behavior of dilute surfactant solutions is discussed.
- A novel experimental method to examine the flow behavior inside thinning fluid filaments is presented in chapter 5. We describe this approach in detail and study the flow inside a well-characterized, viscoelastic polymer thread. Finally, we employ this method to study the flow kinematics in surfactant solutions, covering a broad surfactant and salt concentration, and revealing a unique banding instability in dilute surfactant systems.
- In chapter 6, we use an optimized microfluidic cross-slot in combination with various optical detection techniques to further study microstructural transitions occurring in this extensional flow instability.
- Finally, we combine our results from the previous chapters and discuss the unique flow instability arising in various flow fields in chapter 7, in an effort to provide a more unifying view of such phenomena in different flow kinematics.
- Chapter 8 summarizes the main conclusions of this work and provides an outlook for further studies, including preliminary results regarding the flow behavior in biopolymeric filaments.

2 Theoretical Background

This chapter provides a theoretical introduction and a state-of-the-art understanding of the topics covered in this thesis. A brief overview of micellar aggregation is presented, focusing on the anisotropic growth and the formation of rodlike and wormlike micelles. Subsequently, the flow behavior of these solutions in shear and elongational flow fields is discussed. Here, the most important rheological features in bulk measurements as well as in microfluidic devices are reviewed. Eventually, an overview of potential instabilities in surfactant solutions in shear and extensional flows is given.

2.1 Surfactants - from single molecules to micellar aggregates

The term surfactant is a widely used blend of *surface active agent*, which literally means that surfactants reduce the free energy of surfaces or interfaces [23]. Surfactants are amphiphilic molecules, consisting of a hydrophilic end, the so-called *headgroup*, and a hydrophobic chain, known as *tail* (Fig. 2.1(a)). While the hydrophobic part generally consists of a hydrocarbon chain, the surfactant headgroup can either be neutral or charged, where in the latter case anionic, cationic and zwitterionic surfactants systems exist. Ionic surfactants are the most well-known and best studied surfactant systems. They contain an oppositely charged counterion that can diffuse upon dissolution, as shown in Fig. 2.1(b).

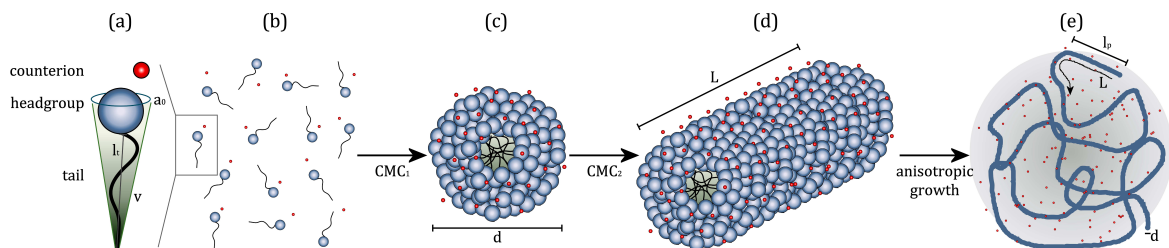


Figure 2.1: Schematic of morphological transitions of ionic surfactants, based on [22]. (a) Surfactant molecule, consisting of hydrophilic headgroup (with occupied surface area a_0), counterion and hydrophobic tail (length l_t and volume v). (b) Surfactant molecules in solution below CMC_1 . (c) Spherical micelles (diameter d) form at $CMC_1 < c_{\text{surf}} < CMC_2$. (d) Transition from spherical to rigid, rodlike micelles with length L above CMC_2 . (e) Further anisotropic growth of semi-flexible, wormlike micelles with persistence length $l_p \ll L$.

In a solution, surfactant molecules can self-assemble into various morphologies, including globular micelles, short, rodlike micelles, long, wormlike micelles (WLM), vesicles, bilayers and lamellar structures [24]. The spontaneous self-assembling of surfactant molecules in a solution is a remarkable ability and the first idea of micellization was reported in 1913 by McBain [25]. Later, in 1948 Debye [26] proposed the first molecular theory of micellar formation, with two competing energy contributions: Repulsive interactions between ionic headgroups on the micellar surface and attractive van der Waals interactions between surfactant tails in the micellar core. The main driving force for aggregation is to minimize the free energy of the system. Upon aggregation the standard free energy difference $\Delta\mu_g^0$ between a surfactant molecule in an aggregate (size g) and a single, dispersed one can be decomposed, based on molecular considerations: removal of the hydrophobic tail from contact with water into the micellar core; packing constraints of the tail, since the hydrophilic headgroup remains at the micellar surface; creation of an interface between the hydrophobic domain and water; steric and electrostatic repulsion between headgroups at the micelle surface [24]. The interplay between these effects and the minimization of the energy of a micelle determines the formation of micellar aggregates with equilibrium sizes above a *critical micelle concentration* CMC.

Above the first critical micellar concentration CMC_1 , surfactant molecules form spherical micelles (Fig. 2.1(c)). In order to minimize the contact area of hydrophobic tail and water, the surfactant tails form a compact, hydrocarbon micellar core, while the surfactant headgroups and the corresponding counterions form the polar shell at the aggregate-water interface. The diameter d of these spherical micelles is limited by the length of the surfactant tail l_t . Micellar aggregation depends on many parameters, such as surfactant concentration, addition of salt, temperature or geometry of the surfactant molecule [12]. Geometrical relations can be described by the hydrocarbon chain volume v , the hydrocarbon tail length, l_t and the optimal surface area per molecule at the hydrocarbon-water interface a_0 [27]. The packing parameter $\text{PP} = v/a_0l_t$ is often used to determine aggregate morphology and spherical micelles form for $\text{PP} \leq 1/3$. However, the packing parameter does not account for environmental conditions, such as salinity which can change a_0 of ionic surfactants and lead to closer packed micelles. Thus, the packing parameter has to be taken with caution [28].

Upon increase of surfactant concentration, a transition from spherical to short, rodlike micelles occurs at the second critical micellar concentration CMC_2 , as shown in Fig. 2.1(d). These small micelles have a contour length L that is much smaller than the persistence length $L \ll l_p$. The persistence length l_p determines the flexibility of a polymeric chain [29] and in the case of $L \ll l_p$, rodlike micelles behave like small, rigid objects. Rodlike micellar solutions exhibit distinct rheological properties, such as shear-thickening, shear-induced structure formation and banding instabilities in shear flow [12, 13, 30, 31, 32], which is discussed in more detail in chapter 2.2.

Further increase of surfactant concentration leads to a growth of micellar length L in the semidilute regime and promotes anisotropic growth of semiflexible wormlike micelles (WLM) with $L \gg l_p$, as shown in Fig. 2.1(e). These long micellar aggregates are held together by weak physical interactions and can break and reform, depending on characteristic timescales [33, 34]. Further, WLM can entangle, which causes viscoelas-

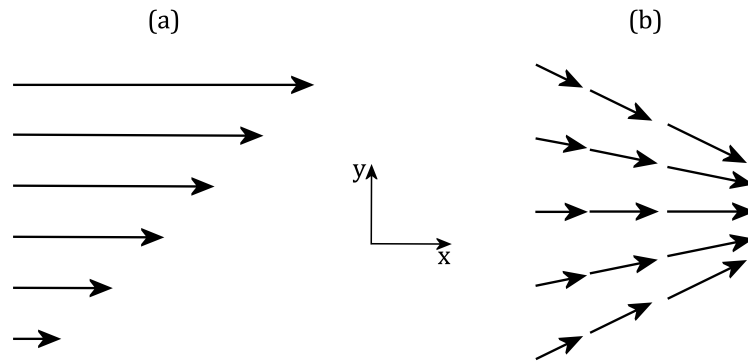


Figure 2.2: Schematic vector representation of (a) a shear flow, e.g. between two parallel plates, and (b) an elongational flow field, e.g. in a converging channel.

ticity similar to polymer solutions, and consequently these systems were termed *living polymers*. WLM micelles were extensively studied and are widely used as additives in home and personal care products [14], as drag reducing agents [15, 16, 17, 18] or as fracture fluids in enhanced oil and gas recovery [19, 20].

The geometrical relations between the surfactant head and tail, together with the constraint that the radius of a micelle cannot exceed l_t , lead to the formation of elongated wormlike micelles for $1/3 \leq PP \leq 1/2$ [27, 35]. However, certain additives can also promote the anisotropic growth of ionic micellar aggregates. Particularly, small molecules of oppositely charged, strongly binding counterions, such as salicylate, tosylate or chlorobenzoate, which all contain an aromatic phenyl group, result in the formation of WLM at lower critical micelle concentrations. These counterions are incorporated in the polar shell, resulting in a reduction of electrostatic headgroup repulsion and leading to screened WLM aggregates. At a constant surfactant concentration c_{surf} in the dilute concentration regime above CMC_1 , micellar morphology can be tuned by the addition of salt. The amount of added salt is often expressed as molar salt/surfactant ratio $R = c_{\text{salt}}/c_{\text{surf}}$. Upon increase of R , flow behavior and rheology of surfactant solutions dramatically changes, which is discussed in the flowing for rodlike and wormlike micelles.

2.2 Flow and deformation of surfactant solutions

Rheology studies the deformation and flow of matter and helps to predict the flow behavior of fluids in different flow kinematics. Detailed descriptions of the fundamentals and principles of rheology and rheological measurements are available in textbooks [36, 37]. From a fluid mechanical point of view, fluid deformation in simple flow fields can be divided into shear flows and elongational flows.

Shear deformation generates a flow with parallel streamlines, resulting in a transversal velocity gradient dv_x/dy perpendicular to the flow direction x , as schematically shown in Fig. 2.2(a). Here, vorticity ensures that fluid microstructures are rotated away from the principal axes of stretching [38]. Rotational rheometers are commonly

employed to study the linear and non-linear material response in a well-defined, stationary, laminar shear flow field.

However, many industrial applications and processes, such as atomization and spraying [2], electrospinning [3], or roll-coating [4], often involve complex flow fields with strong extensional components and flow behavior in elongation can strongly deviate from that in shear. Elongation corresponds to converging or diverging streamlines, thus generating a longitudinal, streamwise velocity gradient dv_x/dx , with respect to the flow direction x , as schematically shown in Fig. 2.2(b). Extensional flows are irrotational and extremely efficient at unraveling flexible macromolecules, such as DNA, or orienting rigid molecules [38]. Different techniques, such as contraction and expansion flows, filament stretching, capillary breakup or stagnation point flows are generally employed to study the elongational flow behavior of complex fluids.

Here, we review the most characteristic flow behavior of rodlike and wormlike surfactant solutions, focusing on classical shear rheometry as well as measurements in elongational flow fields. Besides the bulk rheological measurements, we further review the flow behavior of these surfactant solutions in microfluidic devices under confined flow conditions.

2.2.1 Shear rheology

Among the rich variety of phenomena in shear flow of aqueous surfactant solutions, the shear-thickening transition even at very low surfactant concentrations is one of the most puzzling features. This phenomenon was first reported by Rehage and Hoffmann [30] for a 0.9 mM cetylpyridinium salicylate (CPySal) system and has received much interest due to potential applications in drag reduction.

Figure 2.3 illustrates this effect for a representative 30 mM dilute solution of cationic surfactant hexadecyltrimethylammonium bromide (CTAB) with the salt sodium salicylate (NaSal), at a salt/surfactant ratio $R = c_{\text{salt}}/c_{\text{surf}} = 0.35$. In Fig. 2.3(a) the transient shear viscosity η^+ is shown as a function time t for four different shear rates $\dot{\gamma}$, similar to the original experiments by Rehage and Hoffmann [30]. At small shear rates, e.g. $\dot{\gamma} = 4 \text{ s}^{-1}$, the viscosity is independent of time and defines the zero shear viscosity $\eta_0 \approx 3 \text{ mPa s}$. Upon increase of shear rate beyond the critical shear rate $\dot{\gamma}_c$, e.g. $\dot{\gamma} = 30 \text{ s}^{-1}$, the viscosity again starts at η_0 but suddenly increases after an induction period at a critical time t_c by more than one order of magnitude. Subsequently, the viscosity plateaus at $\eta \approx 40 \text{ mPa s}$ for $t > 200 \text{ s}$, exhibiting large oscillations in the recorded stress signal [40, 41]. Further increase of shear rate results in an earlier onset of shear-thickening, thus the induction period and t_c decreases with increasing shear rates [42, 43, 44], as shown in the inset graph in Fig. 2.3(a). Additionally, the induction period can depend on surfactant concentration [45], flow geometry [46] or temperature [42]. Scaling the critical shear rate with the critical time required for the onset of shear-thickening, results in a constant critical deformation $\gamma_c = t_c * \dot{\gamma}_c \approx 1000$. Note that for shear rates smaller than the critical shear rate $\dot{\gamma}_c$, the viscosity does not increase even for $\gamma \gg \gamma_c$.

In Fig. 2.3(b) the plateau values of the quasi-stationary viscosity are plotted as a function of shear rate. This typical shear-thickening flow curve shows the characteristic

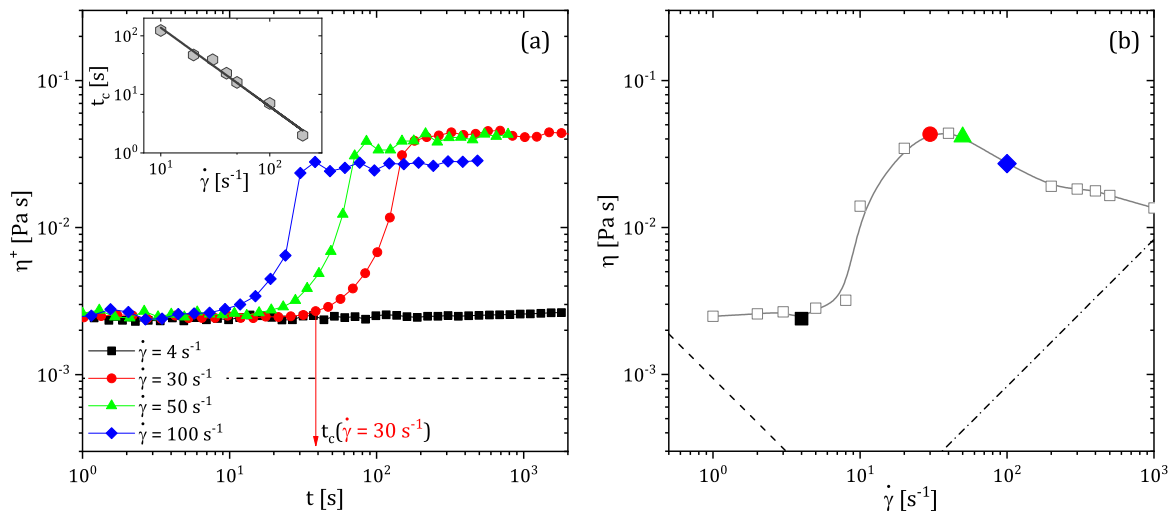


Figure 2.3: Shear rheology of a 30 mM CTAB/NaSal, $R = 0.35$ solution. (a) Transient shear viscosity η^+ as a function time for four different shear rates $\dot{\gamma}$. Shear-thickening sets in above a critical shear rate at a critical time t_c , as shown for $\dot{\gamma} = 30 \text{ s}^{-1}$. The inset shows the critical time as a function of shear rate. (b) Steady shear viscosity η as a function of shear rate for the same sample shown in (a). Viscosity values are averaged after the induction period in the stationary regime, as shown for the colored symbols, which correspond to the plateau values in (a). Dashed lines in (a) and (b) represent the lower torque limit of the rheometer. Dashed-dotted line in (b) indicates the onset of secondary flows due to inertia [39].

increase in viscosity at $\dot{\gamma}_c \approx 10 \text{ s}^{-1}$, followed by a shear-thinning regime at higher shear rates $\dot{\gamma} > 50 \text{ s}^{-1}$. Although, experiments are performed in the lower detection limit of the rheometer (dashed black lines in Fig. 2.3(a) and (b)) due to the relatively low viscosity of the solution, shear-thickening should not be mistaken as an occurrence of secondary flows, which set in at higher shear rates as predicted theoretically [39] (see dashed-dotted line in Fig. 2.3(b)). The flow curve in Fig. 2.3(b) is obtained under strain-controlled conditions. Experiments under controlled stress condition show a re-entrant, S-shaped flow curve with a hysteretic regime [44, 47], which is discussed in chapter 3.2 in more detail.

The shear-thickening transition is linked to the formation of a more viscous, shear-induced structure (SIS) or shear-induced phase (SIP) [30, 48]. Various experimental techniques were employed to study the SIS formation, including bulk shear rheology and flow-induced birefringence measurements (FIB) [15, 42, 44, 47, 48, 49, 50, 51, 52], small-angle light scattering (SALS) [45, 53, 54] and small-angle neutron scattering (SANS) [55, 56, 57, 58, 59], or particle image velocimetry (PIV) [44, 60] and different mechanisms were reported to explain the SIS phenomenon. Berret *et al.* [55] investigated very dilute hexadecyltrimethylammonium p-toluenesulfonate (CTAT) solutions using shear rheometry as well as small-angle neutron scattering and proposed the coexistence of a purely viscous state with short micelles and a strongly viscoelastic network of entangled micellar aggregates. Hu *et al.* [42] observed high flow-induced birefringence and strongly nonlinear viscoelasticity accompanying the shear-induced transition. They suggested that surfactant molecules self-assemble to form new struc-

tures resulting in shear-induced coagulation. Liu and Pine [45] observed the formation of fingerlike gel structures, growing from the inner wall in a Couette cell, eventually spanning the whole cell gap. These structures retract and regrow dynamically over time, leading to large fluctuations in the stress signal. On the other hand, Cates and Candau [61] presented a different scenario based on the linking and delinking of large micellar rings to explain the shear-thickening transition.

We summarize the most important features of the SIS formation according to the minimal scenario suggested for this transition by Lerouge and Berret [13]:

1. Shear-thickening occurs in dilute surfactant solutions that can self-assemble into cylindrical, rodlike micelles.
2. Under rest, the solution exhibits a viscosity close to that of the solvent water.
3. In steady shear experiments, the viscosity increases at a critical shear rate and after an induction period, due to the formation of viscoelastic shear-induced structures (SIS).
4. In the shear-induced state, the solution exhibits strong anisotropic scattering and birefringence, corresponding to a highly aligned state of shear-induced structures.
5. Shear-thickening is associated with uniaxial micellar growth of rodlike aggregates in response to flow-induced alignment.
6. The shear-induced state is transient and the surfactant solution will eventually revert to an isotropic state after cessation of flow.

The surfactant solution shown in Fig. 2.3 is in the dilute concentration regime and consists of small, rodlike micelles. Upon further addition of salt at the same surfactant concentration, anisotropic growth starts and long wormlike micelles form. These dilute WLM solutions also exhibit shear-thickening as previously shown for equimolar CTAB/NaSal and CPyCl/NaSal solutions [40, 41, 54, 56]. However, these viscoelastic systems exhibit shear-thinning behavior prior to shear-thickening, with a zero shear plateau orders of magnitude larger than the viscosity of the solvent, in striking contrast to the dilute solutions with low salt content, as exemplified in Fig. 2.3.

Increasing the amount of salt or surfactant further, yields to the formation of WLM solutions without shear-thickening behavior. These systems show a zero shear viscosity, up to six orders of magnitude higher than that of the solvent, depending on sample composition, followed by pure shear-thinning behavior, where wormlike micelles align with the flow field at high shear rates. The rheology of WLM solutions was thoroughly examined in steady shear as well as in oscillatory shear measurements over the past decades [51]. At high concentrations, WLM entangle into a transient network, thus promoting viscoelasticity. To release stresses, two relaxation mechanisms are present in WLM solutions. First, the long micellar chains can diffuse along their own contour length in a reptation-like motion similar to polymer solutions with a characteristic time scale λ_{rep} . However, unlike covalently bound polymer chains, WLM are dynamical aggregates, constantly breaking and reforming. This second, additional relaxation mechanism is described by the breakage time λ_{break} . In the slow retraction

limit ($\lambda_{\text{rep}} \ll \lambda_{\text{break}}$), the dominant stress relaxation mechanism is the reptation of linear, unbranched, polydispers WLM, resulting in a non-exponential stress decay [34, 62]. On the other hand, in the fast breaking limit ($\lambda_{\text{rep}} \gg \lambda_{\text{break}}$), micelles break and reform within the reptation timescale [28]. Here, the rheological behavior of these *living polymers* can be described by the Maxwell model, characterized by an exponential stress decay with a single relaxation time $\lambda = \sqrt{\lambda_{\text{rep}}\lambda_{\text{break}}}$. The mechanical Maxwell model describes the viscoelastic fluid properties by connecting the elastic (G_0) and viscous (η_0) contributions in series. For deformations faster than the relaxation time, the fluid behaves like a Hookean solid $\tau = G_0\gamma$, with constant plateau modulus G_0 relating the shear stress τ to the shear strain γ . If instead the deformation is slower than the relaxation time, the fluid behaves like a viscous liquid $\tau = \eta_0\dot{\gamma}$ with a zero shear viscosity η_0 and deformed by a deformation rate $\dot{\gamma} = d\gamma/dt$ [36]. The Maxwell model combines these two extremes and the elastic storage modulus G' and the viscous loss modulus G'' can be calculated as a function of frequency ω according to:

$$G'(\omega) = \frac{\omega^2\lambda^2}{1 + \omega^2\lambda^2}G_0 \quad , \quad G''(\omega) = \frac{\omega\lambda}{1 + \omega^2\lambda^2}G_0 \quad , \quad \lambda = \frac{\eta_0}{G_0} \quad (2.1)$$

Here, λ is the single relaxation time. To measure the relaxation time and the viscoelastic properties of WLM solutions, oscillatory shear measurements are employed, by deforming the fluid with a small-amplitude sinusoidal deformation within the linear viscoelastic regime (LVE) and measure the fluids response. Storage and loss modulus are calculated from the phase angle between stress and strain signals. Figure 2.4 shows an small-amplitude oscillatory shear (SAOS) measurement of a viscoelastic 30 mM CTAB/NaSal, $R = 7.67$ surfactant solution. Storage modulus G' and loss modulus G'' are plotted as a function of angular frequency ω at a strain amplitude of $\gamma_0 = 0.01$, well within the LVE regime. Additionally, G' and G'' are calculated according to Eq. 2.1 and plotted as black and red lines, respectively. For frequencies $\omega \leq 10$ rad/s, the viscoelastic behavior can be perfectly described by the Maxwell model, with slopes of 1 and 2 for G' and G'' , respectively. One method to derive a shear relaxation time in Fig. 2.4 is from the cross-over frequency of storage and loss modulus $\lambda_s \equiv \lambda = 1/\omega_c$, which yields for the specific sample in Fig. 2.4 $\lambda_s \approx 4$ s. Note that the longest shear relaxation time in the terminal regime can also be obtained according to $\lambda = \lim_{\omega \rightarrow 0} G'/(G''\omega)$. However, since the terminal regime is not accessible at low R , we choose the cross-over frequency to determine the shear relaxation time λ_s . With increasing ω , G' exhibits a plateau (G_0), while G'' deviates from Maxwellian behavior and passes through a minimum, which can be linked to the breaking time of micelles. Subsequently, G'' increases at higher frequencies (not shown), associated with faster relaxation processes, e.g. of Rouse modes [62].

Hitherto, the rheological properties of shear-thickening, dilute solutions that contain rodlike micelles, and shear-thinning, viscoelastic systems of wormlike micelles in bulk shear flow have been discussed. However, bulk rheometrical measurements are limited in terms of accessible shear rates and complications such as secondary flow, viscous heating or edge fracture might arise [39]. One possibility to overcome these limitations are controlled, miniaturized flow channels on the micrometer length-scale, so-called microfluidics, with negligible inertia contribution and without the influence of surface tension.

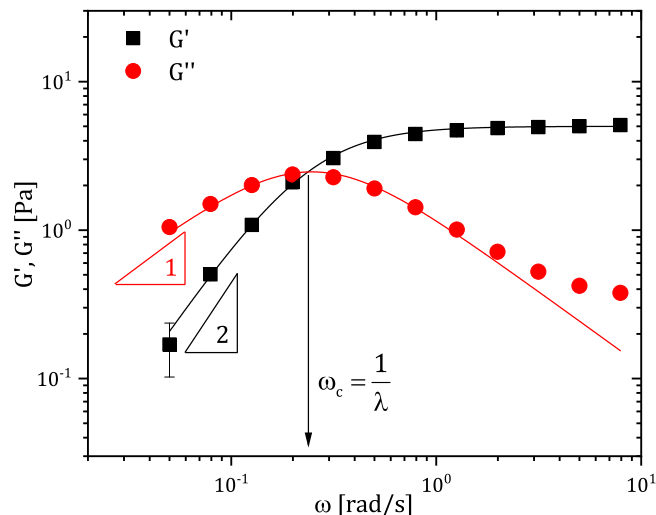


Figure 2.4: Storage modulus G' and loss modulus G'' as a function of angular frequency ω determined from SAOS measurements of a 30 mM CTAB/NaSal, $R = 7.67$ WLM solution. The black and red lines represent a Maxwell fit of the experimental data according to Eq. 2.1. The characteristic frequency ω_c is determined at the cross-over of G' and G'' .

With the advent of microfluidics as a versatile tool to examine fluids at small length-scales and high shear rates, surfactant solutions were studied in a vast number of different confined microfluidic flow geometry in recent years. Comprehensive reviews with detailed descriptions of microfluidic techniques and their applications are available [63, 64, 65]. Most of the studies of surfactant solutions in microfluidics focused on the flow behavior and flow instabilities of viscoelastic, shear-thinning WLM solutions in shear flow [66, 67, 68, 69, 70, 71, 72, 73] and contraction or expansion flows [69, 73] with mixed flow kinematics, where extensional forces dominate at the channel center-line. A detailed review of microfluidic flow of wormlike micellar solutions is provided by Zhao *et al.* [74].

One remarkable phenomenon that arose in microfluidic studies is the emergence of a stable, long-lived flow-induced structured phase (FISP), in contrast to the reversible SIS in bulk shear flow that disintegrate soon after the flow stops. Vasudevan *et al.* [75] used semi-dilute CTAB/NaSal precursor solutions, flowing through a packed bed of glass beads and reported the formation of a stable gel, as probed by cryogenic transmission electron microscopy (cryo-TEM). The microfluidic design resulted in deformation rates on the order of $\mathcal{O}(10^5 - 10^6 \text{ s}^{-1})$. Using fluorescent Nile Red dye, which bound to the micelles, Cheung *et al.* [76] showed that flow through a similar array of microposts resulted in local concentration variations and that the stable FISP had a higher micelle concentration than the original precursor solution. The same 50 mM CTAB/NaSal, $R = 0.32$ solution was investigated by Cardiel *et al.* [77] in a microfluidic channel with micropost arrays. The authors observed the formation of a stable FISP with entangled, branched, and multiconnected micellar bundles, as evidenced by electron microscopy. They proposed a transition from rodlike micelles in the precursor solution to a micellar network with nanosized pores, induced by the spacial confinement as well as by high strains $\mathcal{O}(10^3)$ and strain rates $\mathcal{O}(10^3 \text{ s}^{-1})$ between the microposts.

In summary, aqueous surfactant solutions exhibit a plethora of unique rheological features in bulk as well as microfluidic shear flow. Depending on sample composition, surfactant solutions can exhibit pure Newtonian flow behavior at very low surfactant and salt concentrations (below CMC_1), shear-thickening in solutions of rodlike micelles and shear-thinning in WLM systems. These characteristics were extensively studied and detailed reviews of surfactant solution behavior in shear flow are available [12, 13]. However, compared to the numerous investigations in shear, the elongational properties of surfactant solutions have received considerably less attention up to now, since experiments that generate a pure extensional flow field are generally more challenging. In the next chapter, a thorough description of the flow behavior of surfactant solutions undergoing extensional deformation is provided.

2.2.2 Elongational deformation

Despite the omnipresence of flow fields with strong elongational components, the flow behavior of surfactant solutions in extension is still poorly understood. Early investigations of wormlike surfactant solutions were based on experiments using opposed jet [78, 79, 80, 81, 82, 83] and four-roll mill devices [84, 85, 86] to generate extensional flow fields.

Prud'homme and Warr [78] were the first to study the response of wormlike micellar solutions in an elongational flow field. They used an opposed jet device to probe equimolar solutions of the surfactant tetradecyltrimethylammonium bromide (TTABr) with the salt sodium salicylate (NaSal) in an uniaxial flow field. The authors observed three different regimes of elongational viscosity with increasing elongation rate. First, at low rates a plateau in elongational viscosity was found, corresponding to the Newtonian response. As the elongation rate increased, an elongational-thickening of the solution, accompanied by strong alignment of the micelles in the direction of the flow up to a critical strain rate, was observed, in contrast to the shear-thinning behavior of the solution in shear flow. Increasing the elongation rate even further, resulted in a decrease in elongational viscosity, due to scission of wormlike micelles and rapid end cap formation. This mechanism was confirmed by Chen and Warr [80], using light scattering measurements that indicated first an increase of micellar radius of gyration, followed by a decrease with increasing elongation rate. Similar results were found for other surfactant systems using similar opposed jet devices [79, 81, 82]. Müller *et al.* [83] investigated the flow of cetyltrimethylammonium p-toluenesulfonate (CTAT) solutions in an opposed jet device as well as flowing through porous media, covering a broad concentration regime. They examined the response of different solutions that exhibited Newtonian, shear-thickening or shear-thinning flow behavior. While samples showing shear-thickening did not show extensional-thickening in the strong elongational flow field between the opposing jets, these solutions displayed a substantial increase in apparent viscosity beyond a critical apparent shear rate flowing through porous media as a result of a synergistic effect of shear and relatively weak elongation [83].

In a series of publications, Kato *et al.* [84, 85, 86] studied the rheological properties of aqueous CTAB/NaSal solutions in steady planar elongational flow using a four-roll mill device. The authors measured the flow-induced birefringence and calculated the planar elongational viscosity, using the stress-optical rule (SOR) [87]. They claimed

Trouton ratios of $Tr = \eta_e/\eta_0 \approx 4$ (with the elongational viscosity η_e) in both the Newtonian and the elongational thinning region. Further, they observed turbid regions in the elongational flow field of the four-roll mill, caused by structural changes inside shear-thickening surfactant solutions.

However, all the devices mentioned above generate an unknown prestrain history, including a considerable amount of shearing. In order to overcome these disadvantages, two experimental techniques have emerged as versatile tools for measuring the response of a fluid in a pure uniaxial extensional flow field and to determine fundamental fluid properties such as elongational viscosity η_e and relaxation time λ_e : the filament stretching extensional rheometer (FiSER) and the capillary breakup elongational rheometer (CaBER).

Both methods are based on the uniaxial thinning of a cylindrical fluid specimen of height h_0 and diameter D_0 , stretched in axial direction z . In a FiSER experiment, the upper plate continuously moves upward with a predetermined velocity profile, stretching the sample such that the fluid is subjected to a strong uniaxial extensional deformation [38]. In contrast, in a CaBER experiment, the upper plate is not constantly moving upward, but is separated during an initial step stretch to a certain distance, creating an unstable liquid bridge. Subsequently, the thinning fluid filament is monitored in the capillary-driven, uniaxial elongational flow between stationary plates.

The velocity gradient tensor for a homogeneous, shear-free, irrotational, uniaxial extensional flow is given by

$$\nabla v = \frac{1}{2}\dot{\varepsilon}(t) \begin{pmatrix} -1 & 0 & 0 \\ 0 & -1 & 0 \\ 0 & 0 & 2 \end{pmatrix} \quad (2.2)$$

with elongation rate $\dot{\varepsilon}(t)$. For a steady flow in Eulerian and Lagrangian sense, the fluid is stretched with a constant elongation rate, i.e. $\dot{\varepsilon}(t) = \dot{\varepsilon}_0$. In a FiSER experiment the plates can be separated with an exponentially increasing separation profile, thus the filament height $h(t)$ increases exponentially during stretching, according to Eq. 2.3. Consequently, the diameter $D(t)$ thins over time with a constant elongation rate $\dot{\varepsilon}_0$ (Eq. 2.4) and a linearly increasing logarithmic Hencky strain $\varepsilon(t)$ (Eq. 2.5).

$$h(t) = h_0 \exp(\dot{\varepsilon}_0 t) \quad (2.3)$$

$$D(t) = D_0 \exp\left(-\frac{1}{2}\dot{\varepsilon}_0 t\right) \quad (2.4)$$

$$\varepsilon(t) = \dot{\varepsilon}_0 t = -2 \ln\left(\frac{D(t)}{D_0}\right) \quad (2.5)$$

In CaBER experiments, the fluid is stretched from an initial height h_i to a final height h_f . Here, the fluid can spatially rearrange and select an own time scale of subsequent, capillary-driven filament thinning, generally resulting in a time-dependent elongation rate [38, 88]. A detailed description of the CaBER method is presented in chapter 4.1.

Both FiSER and CaBER were used to study the response of surfactant solutions in uniaxial extension. Rothstein [89] investigated the transient extensional rheology of wormlike micelle solutions, using a filament stretching rheometer. He used a series of CTAB/NaSal solutions, covering a surfactant concentration regime of $25 \leq c_{\text{surf}} \leq 100$ mM and a salt/surfactant ratio of $0.5 \leq R \leq 2$. Flow-induced birefringence was measured, by passing light of a known polarization state and frequency through the sample and measuring the resulting polarization change [89]. The shear-thinning WLM solutions showed strain-hardening in transient uniaxial elongation that was well-described by a (Finitely-Extensible Non-linear Elastic) FENE-PM model [90] with two relaxation modes. Further, these WLM filaments were found to fail through a dramatic rupture near the axial mid plane at a critical stress, nearly independent of strain rate.

Similar results were found by Bhardwaj *et al.* [91, 92] for equimolar CTAB/NaSal solutions ($10 \leq c_{\text{surf}} \leq 150$ mM) as well as CPyCl/NaSal solutions ($50 \leq c_{\text{surf}} \leq 200$ mM, $R = 0.5$), dissolved in a brine of 100 mM NaCl. The authors argued that the dramatic filament failure stems from local scission of individual WLM chains. Further Bhardwaj *et al.* [91] used a pre-shearing device, attached to a filament stretching rheometer, and found that pre-shear before stretching delayed the onset of strain-hardening. They argued that pre-shear before filament stretching might break down the wormlike micelles, reducing their size, thus resulting in a reduction of strain-hardening.

Chellamuthu and Rothstein [93] measured the effect of branching on the extensional rheology of a series of wormlike micelle solutions. Linear and branched WLM solutions of sodium oleate (NaOA) and octyltrimethylammonium bromide (OTAB) ($2 \leq c_{\text{surf}} \leq 8$ w%, $R = 2.33$) were used and showed single mode Maxwell behavior in the linear viscoelastic regime. It was confirmed through cryo-transmission electron microscopy imaging that the maximum in shear viscosity corresponds to the transition from linear entangled to branched micelles, as demonstrated in previous studies [94, 95]. This structural change is accompanied by a reduction of degree of strain-hardening of the extensional viscosity. The Trouton ratio decayed from $Tr \approx 1000$ to $Tr \approx 3$ with increasing surfactant concentration, which was attributed to an additional stress relief mechanisms available to branched micelles. Here, branching points are able to slide along the length of the micelles, leading to so-called *ghost-like* crossings of micellar entanglement points [93].

Moreover, the capillary breakup elongational rheometer was used to study the surface-tension driven, uniaxial thinning of surfactant solutions [5, 6, 91, 92, 93, 96, 97]. Yesilata *et al.* [96] probed the nonlinear shear and extensional flow dynamics of wormlike micellar solutions based on erucyl bis(2-hydroxyethyl) methylammonium chloride (EHAC) with the addition of iso-propanol (25 w%) and the salt ammonium chloride NH_4Cl , covering a surfactant concentration of $18 \leq c_{\text{surf}} \leq 90$ mM and salt/surfactant ratios of $2.65 \leq R \leq 15.89$. These samples exhibited strong extensional thickening with the apparent Trouton ratios increasing by more than two orders of magnitude. The extensional relaxation time λ_e was derived from the exponentially decaying regime of the filament diameter and was compared with the shear relaxation time λ_s , derived from SAOS measurements. The authors found that the relaxation time in extensional flow was a factor of three lower than in shear flow. Similar low ratios of λ_e/λ_s were found for CTAB/NaSal solutions at $c_{\text{surf}} < 50$ mM [92]. Here, increasing the surfac-

tant concentration resulted in a plateau of $\lambda_e/\lambda_s \approx 1$ for $c_{\text{surf}} \geq 50$ mM. In contrast, solutions of CPyCl/NaSal started at similar small ratios λ_e/λ_s , but monotonically increased with increasing surfactant concentration. Similar to FiSER measurements, strain-hardening was also observed in CaBER experiments [91, 92, 93, 96, 97]. However, Bhardwaj *et al.* [91] showed that pre-shearing WLM solutions before CaBER measurements leads to a faster strain-hardening with larger steady-state extensional viscosities, as compared to FiSER measurements, demonstrating the sensitivity of these self-assembling systems to pre-conditioning. Recently, Omidvar *et al.* [98] used CaBER as well as dripping-onto-substrate (DoS) techniques to detect wormlike micellar microstructure in a 100 mM CPyCl/NaSal solution with $0.52 \leq R \leq 0.9$ that showed a transition from linear to branched micelles with increasing R . Additionally, they used 3 wt% OTAB/NaOA solutions (corresponding to approximately 120 mM), exhibiting a transition from linear to shorter linear micelles with increasing concentration of OTAB. Omidvar *et al.* [98] showed that at a given zero shear viscosity, branched wormlike micelles exhibit longer filament lifetimes t_{fil} , i.e. the time when the fluid threads ruptures, than linear wormlike micelles. The filament lifetime scaled differently with zero shear viscosity in these two systems. Hence, filament thinning in CaBER provides a criterion to distinguish between these two types of microstructural transitions in wormlike micelles, confirming earlier work of Sachsenheimer *et al.* [5]. Further, extensional relaxation times measured in CaBER experiments were smaller than obtained by the DoS technique, which was attributed to strong nonlinear effects, such as flow-induced micellar breakage during the step-strain in CaBER experiments.

Kim *et al.* [97] investigated a 100 mM CTAB/NaSal, $R = 0.5$ solution in 100 mM NaCl brine, using CaBER. They examined the role of geometric configurations by varying the final height $3.91 \leq h_f \leq 6.37$ mm and the plate diameter $3.18 \leq D_0 \leq 6$ mm, while keeping the initial height $h_i = 1$ mm constant. An increase of λ_e/λ_s with increasing final aspect ratio $\Lambda_f = h_f/D_0$ was observed, eventually reaching a plateau value of $\lambda_e/\lambda_s \approx 1$ for $\Lambda_f > 1.4$. The authors argued that initial conditions in CaBER experiments should not have a dominant effect on the microstructural relaxation processes at long times due to the absence of larger differences between the relaxation times, but that variations of Λ_f can give rise to initial regimes of apparent extensional thinning, associated with the rearrangement of the liquid bridge [97].

The extensional response of wormlike surfactant solutions was also simulated numerically [99, 100, 101, 102]. The constitutive, two-species VCM modeling approach was proposed by Vasquez, Cook, and McKinley [99] and incorporates scission and recombination of living polymer chains. Simulations show that stretching WLM filaments beyond a critical extension rate leads to a dramatic rupture event as a result of the scission of the entangled wormlike chains. The VCM model covered many of the experimentally observed features during filament stretching and capillary breakup of viscoelastic wormlike micelle solutions [92, 100].

So far, previous investigations mainly focus of extensional flow of viscoelastic, shear-thinning surfactant solutions, consisting of long, wormlike micelles. Solutions containing short, rodlike micelles were considerably less examined. Sachsenheimer *et al.* [5] probed the extensional response of WLM systems as well as short, rodlike micelles of a series of CTAB and CPyCl solutions, covering surfactant concentrations of $5 \leq c_{\text{surf}} \leq$

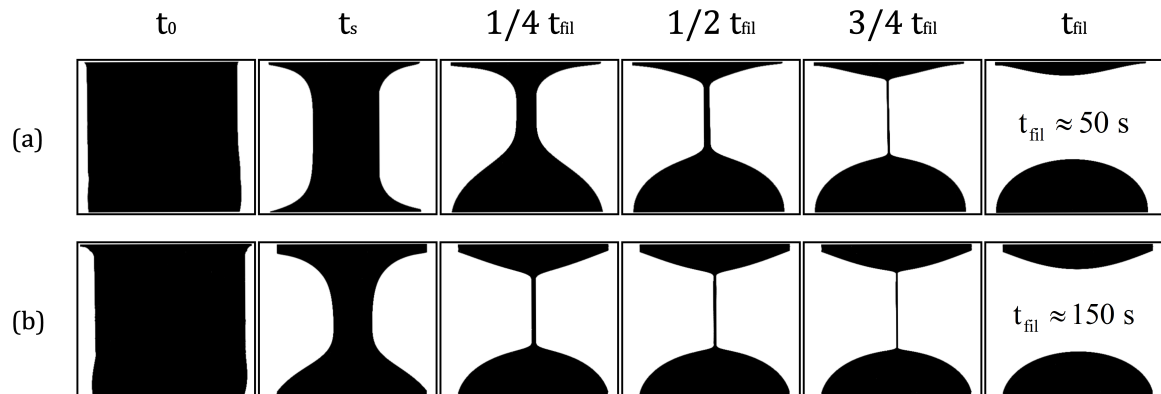


Figure 2.5: Series of images, showing the filament shape of (a) a 30 mM CTAB/NaSal, $R = 7.67$ and (b) a 10 mM CTAB/NaSal, $R = 0.5$ solution, probed by CaBER. The plate diameter, initial and final height, and strike time are $D_0 = 6$ mm, $h_i = 1.5$ mm, $h_f = 6$ mm, and $t_s = 40$ ms, respectively. The upper plate is in its initial position h_i at t_0 and reached the final displacement h_f at t_s . The filament lifetime t_{fil} is determined when the filament ruptured and is inserted for both fluids in the last picture.

25 mM and $5 \leq c_{\text{surf}} \leq 100$ mM, respectively. They used different non-penetrating and penetrating counterions, including NaSal ($0.4 \leq R \leq 10$) and determined the filament lifetime t_{fil} as well as the elongational relaxation time in CaBER experiments. At high surfactant and salt concentrations, filament thinning was controlled by the equilibrium shear modulus G_0 and the breakage time λ_{break} and relaxation time ratios $\lambda_e/\lambda_s \approx 1$ were found. For high surfactant concentrations and low R , $\lambda_e/\lambda_s < 1$ was observed similar to solutions of covalently bound polymers [5]. Furthermore, the authors were able to reveal a distinct difference between solutions of linear and branched micelles, by relating the dependence of filament lifetime on the zero shear viscosity of the solution. At low surfactant concentrations and salt/surfactant ratios, Sachsenheimer *et al.* [5] were the first to observe unusually long filament lifetimes in the order of $\mathcal{O}(10^3)$ s and $\lambda_e/\lambda_s \approx 10$ for low surfactant concentrations c_{surf} , irrespective of R . This stunning feature is even more puzzling, since these dilute solutions can exhibit low shear viscosities close to water, with no measurable elasticity, yet show longer filament lifetimes than highly viscoelastic WLM solutions.

To highlight this unique phenomenon, we discuss the extensional flow behavior of these dilute surfactant solutions here, similar to the investigations by Sachsenheimer *et al.* [5]. Figure 2.5 shows consecutive images of the filament shape of (a) a highly viscoelastic 30 mM CTAB/NaSal, $R = 7.67$ and (b) a dilute 10 mM CTAB/NaSal, $R = 0.5$ surfactant solution, as probed by CaBER. Additionally, we plot the filament diameter over time for both solutions in Fig. 2.6. Note that $t = 0$ in Fig. 2.6 corresponds to $t = t_s$ in Fig. 2.5. After the upper plate reached the final height at t_s , both solutions show very different filament shapes at the start of the actual CaBER experiment as well as different thinning behavior over time. For the viscoelastic solution in Fig. 2.5(a), a thick thread of diameter $D_1 \approx 2$ mm is formed at $t = 0$. The early thinning is controlled by gravitational sagging [38], characterized by the dimensionless Bond number $Bo = \rho g D / \Gamma > 0.2$, with fluid density ρ and surface tension Γ . Subsequently, the

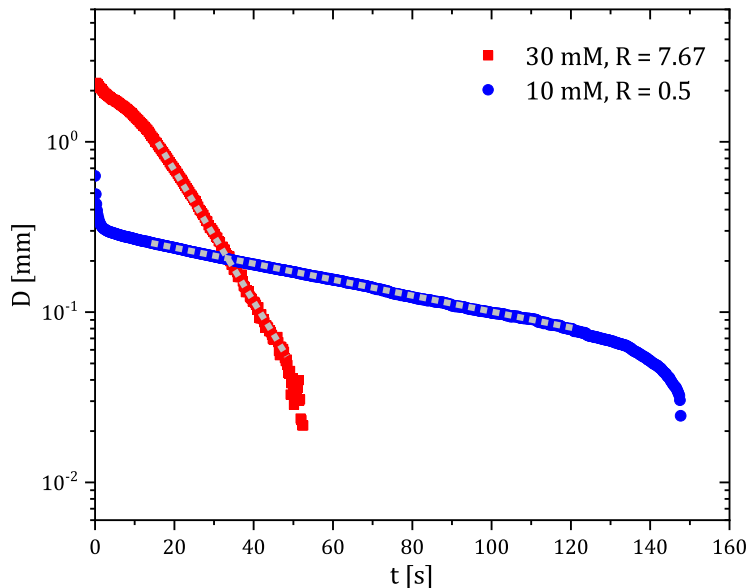


Figure 2.6: Diameter as a function of time for a 30 mM CTAB/NaSal, $R = 7.67$ (red squares) and a 10 mM CTAB/NaSal, $R = 0.5$ (blue circles) solution, probed by CaBER. The data and experimental conditions correspond to Fig. 2.5. Gray dashed lines represent an exponentially decrease of filament diameter with time.

filament shows a cylindrical shape, as shown in Fig. 2.5 at $t \geq 1/2 t_{\text{fil}}$, corresponding to a exponentially decreasing diameter in Fig. 2.6, indicated by the dashed gray line. In this regime, the capillary driven thinning is mainly resisted by elastic forces inside the fluid thread [103] that stem from stretching of WLM with respect to the principal axis of extension, i.e. the axial filament direction z . Eventually, the filament ruptures at a filament lifetime of $t_{\text{fil}} \approx 50$ s. This solution exhibits a zero shear viscosity of $\eta_0 \approx 18$ Pa s and strong viscoelastic properties, as shown in Fig. 2.4.

In contrast, the dilute 10 mM CTAB/NaSal, $R = 0.5$ surfactant solution shows a very distinct thinning behavior. At the beginning of filament thinning, the filament diameter drastically drops to $D_1 \approx 0.3$ mm, as shown in Fig. 2.6. However, the filament does not break, but forms a perfectly cylindrical shape (see. Fig. 2.5 for $t \geq 1/4 t_{\text{fil}}$), that subsequently thins exponentially, as indicated by the dashed gray line in Fig. 2.6. This thinning period is expanded over an interval of more than 100 s, followed by a late Newtonian regime for $t > 120$ s before the filament ruptures at $t_{\text{fil}} \approx 150$ s. This dilute surfactant solution consist of small rodlike micelles, in contrast to the wormlike micellar solution in Fig. 2.5(a), and exhibits a zero shear viscosity of merely $\eta_0 \approx 3$ mPa s, similar to the dilute sample shown in Fig. 2.3.

For this dilute solution, the shear relaxation time can not be determined through SAOS measurements. Therefore, Sachsenheimer *et al.* [5] introduced the filament lifetime ratio $t_{\text{fil}}/t_{\text{fil,N}}$ that compares the determined lifetime in CaBER experiments t_{fil} with the theoretical filament lifetime $t_{\text{fil,N}}$ calculated from the zero shear viscosity of the solution assuming Newtonian flow behavior [104, 105]. For the sample in Fig. 2.5(b) as well as for the surfactant systems with low surfactant and salt concentration investigated by Sachsenheimer *et al.* [5], filament lifetime ratios of $t_{\text{fil}}/t_{\text{fil,N}} > 10^3$ can be

observed.

In order to explain such high filament lifetime ratios as well as high λ_e/λ_s , Sachsenheimer *et al.* [5] were the first to propose an elongation-induced structure (EIS) buildup inside the uniaxially thinning surfactant filament, similar to SIS in shear flow. The authors observed, that a minimum zero shear viscosity $\eta_0 \approx 2-3$ mPa s and a minimum initial diameter $D_1 \approx 0.3$ mm were required to create such long lasting filaments. Additional FiSER experiments suggested, that a minimum total strain of $\varepsilon \approx 1$ was required for EIS buildup in solutions with surfactant concentrations $0 \leq c_{\text{surf}} \leq 30$ mM and $0.2 \leq R \leq 1.6$.

Similar to the investigations by Sachsenheimer *et al.* [5], Omidvar *et al.* [6] explored the sensitivity of extensional flow to wormlike micellar structure. They used aqueous CTAT solutions, covering a concentration regime of $0.7 \leq c_{\text{surf}} \leq 7$ wt% (corresponding to approximately $15 \leq c_{\text{surf}} \leq 154$ mM) and employed a combination of transmission electron microscope (TEM) imaging, shear rheology and capillary breakup extensional rheometry. At surfactant concentrations of $0.7 \leq c_{\text{surf}} \leq 1.1$ wt% ($15 \leq c_{\text{surf}} \leq 24$ mM), the solutions showed shear-thickening and pronounced filament lifetimes, resulting in extremely high Trouton ratios on the order of $\mathcal{O}(10^5)$. The authors calculated extensibility parameters based on bulk rheological data from elongation and shear measurements and argued that cylindrical micelles aggregated into bigger wormlike micelles during uniaxial deformation. The calculated finite extensibility parameters corresponded to WLM with length of hundreds of micrometer and Omidvar *et al.* [6] attributed this to EIS formation in dilute CTAT solutions.

However, direct evidence for the elongation-induced structure buildup in uniaxial extension as reported by Sachsenheimer *et al.* [5] and Omidvar *et al.* [6] in low concentrated surfactant solutions is still missing. In contrast, the formation of EIS was directly observed during planar elongation of higher concentrated surfactant solutions. Okawara *et al.* [106] studied the pressure loss and the rheo-optical behavior of CTAB/NaSal solution through two-dimensional slots and capillaries. Surfactant solutions with $c_{\text{surf}} = 0.5$ mM and $c_{\text{surf}} = 30$ mM were used, covering a salt/surfactant ratio of $0.5 \leq R \leq 10$. With increasing flow rate through the slots, they observed a sudden increase of pressure loss, attributed to the formation of flow-induced structures (FIS). In this regime, vortices and a contraction flow upstream of the slot entrance were generated, induced by FIS formation. Further, for the particular sample 30 mM CTAB/NaSal, $R = 7.7$, Okawara *et al.* [107] used a flow channel with a hyperbolic nozzle that generates a constant elongation rate along the channel center line [108, 109, 110] and employed small-angle light scattering (SALS) to examine the FIS formation. Butterfly-type and streak-type combined pattern occurred in SALS measurements, in the regime where FIS emerge. With increasing elongation rate the streak-type pattern degenerated, indicating a partial collapse of FIS. Moreover, Okawara *et al.* [107] concluded that the flow-induced structure formation depended not only on the strain rate but also on the total strain experienced by the surfactant solution. For similar 30 mM CTAB/NaSal solutions with high salt/surfactant ratios $1 \leq R \leq 9$, Takahashi and Sakata [111] performed turbidity and flow-induced birefringence measurements to probe flow-induced structural changes in surfactant solutions. They used a two-dimensional squeeze flow cell to generate a constant elongation rate

in a planar elongational flow field with central stagnation point. Opaque regions were observed in the center plane, where elongation dominates, and at the corners of the flow field, where shear forces dominate, during squeeze flow. Opacity was caused by EIS in the middle of the planar elongation flow field and by SIS at the corners. Takahashi and Sakata [111] further found that SIS at the corners appeared earlier than EIS in the center plane, but the strain required to generate EIS is considerably smaller than the critical strain for SIS. However, Sachsenheimer *et al.* [5] did not report high filament lifetime ratios $t_{\text{fil}}/t_{\text{fil,N}}$ and no unusually long filament lifetimes for these highly concentrated solutions in CaBER measurements and did therefore not propose an EIS build-up in uniaxial elongation for the highly concentrated surfactant solutions investigated in planar elongation by Okawara *et al.* [106, 107] and Takahashi and Sakata [111].

Despite these investigation, knowledge about the proposed mechanism for EIS formation still remains vague and the phenomenon of long living filaments of highly dilute surfactant solutions remains unexplained on a mesoscopic length scale. Furthermore, microstructural transitions, such as SIS and EIS formation, can cause flow instabilities that change the flow behavior dramatically. However, the relation between the emergence of EIS and flow instabilities in elongational flows is still missing.

2.2.3 Flow instabilities in surfactant solutions

Flow instabilities are ubiquitously observed during deformation of many materials and are characterized by a transition from a homogeneous to a non-homogeneous state of flow when submitted to shear. Banding phenomena, where the non-homogeneous flow is characterized by a localization of high shear, were first reported during the deformation of solids, such as metals, alloys and geological samples over a century ago [112]. In solid mechanics, narrow regions of high shear γ emerge as a consequence of a material instability, resulting from non-monotonic constitutive relations [113].

Similar phenomena are also found in complex fluids, including granular matter, suspensions, emulsions, foams, polymer solutions and melts, as well as aqueous surfactant solutions [7, 8, 9, 10, 11]. Among these systems, surfactants are often used as model systems to study transitions from a homogeneous towards a non-homogeneous flow [12, 13] and we therefore review the most important flow instabilities of surfactant solutions in shear as well as extensional flows in the following.

Instabilities in shear flow

Flow instabilities arise when a homogeneous, steady flow becomes unstable and splits above a critical shear rate or shear stress into multiple coexisting bands, bearing different apparent viscosities and different internal structures [7, 114]. Generally, banding is related to a non-monotonic relationship between shear stress τ and shear rate $\dot{\gamma}$ [7, 115, 116, 117] and transitions are due to the strong coupling between internal structure of the fluid and flow [13]. Flow can change the mesoscopic structure of the fluid, which feeds back on the flow and leads to the separation into coexisting macroscopic bands with different structures [117]. In simple shear flow, such as in a Couette cell, banded structures can occur along the gradient and the vorticity direction and consequently transitions are referred to as gradient banding and vorticity banding [116],

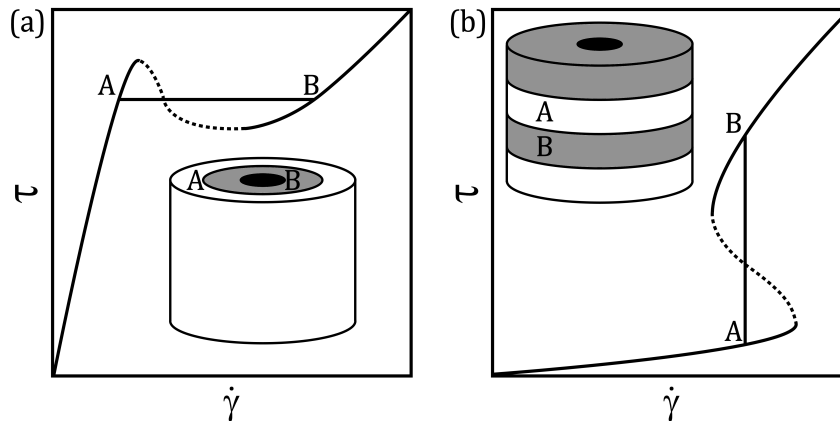


Figure 2.7: (a) Schematic illustration of a constitutive curve for a gradient banded flow. Inset shows a schematic of different morphologies A and B bearing different shear rates at one constant shear stress inside a Couette geometry, where the inner cylinder (black circle) rotates. (b) Schematic of a vorticity banded flow. A and B indicate bands, bearing different shear stresses at one shear rate. Dashed lines represent negative slope of shear rate $\dot{\gamma}$ versus shear stress τ in (a) and vice versa in (b).

respectively. Depending on surfactant and salt concentration, surfactant solutions can exhibit gradient or vorticity banding instabilities. Figure 2.7 schematically shows constitutive flow curves for (a) a gradient banding and (b) a vorticity banding fluid. The insets represent corresponding morphologies A and B inside a Couette cell.

The gradient banding phenomenon, often termed shear banding, was intensively studied in wormlike micellar systems over the last decades both experimentally [10, 40, 52, 117, 118, 119, 120, 121, 122, 123, 124, 125, 126, 127, 128, 129, 130, 131, 132, 133, 134] as well as theoretically [115, 135, 136, 137, 138, 139, 140, 141] and is expected for semi-dilute surfactant solutions [13]. Rehage and Hoffman [114] were the first to report the rheological signature of a shear-banding wormlike micellar solution, by measuring the steady shear stress τ as a function of shear rate $\dot{\gamma}$ for a 100 mM CPyCl/NaSal, $R = 0.6$ solution. Here, we schematically reproduce their results in Fig. 2.7(a) to discuss the constitutive flow curve of a gradient banded flow. Here, the flow curve $\tau(\dot{\gamma})$ is composed of a stress plateau between two critical shear rates (at A and B), connecting two stable branches of high and low viscosity. For shear rates below the first critical shear rate at A, a homogeneous flow with slightly oriented WLM is expected. Increasing the shear rate above this critical value of shear rate at A results in an unstable flow with two coexisting phases at one shear stress: a fluid phase with aligned micelles at the inner rotating cylinder (see B in Fig. 2.7(a)) and a more viscous phase (see A in Fig. 2.7(a)). This stress plateau can extend over several decades of shear rate. Upon further increase of shear rate, WLM strongly align in the whole gap and a homogeneous flow is recovered [13].

In order to shed light on the microstructure and dynamics during the shear banding transition, various methods were employed in combination with bulk rheometry, including particle image velocimetry (PIV) [120, 142, 124] nuclear magnetic resonance (NMR) [119, 130] flow-induced birefringence (FIB) measurements [52, 134] and small-

angle neutron scattering [132, 143]. For semi-dilute systems, Manneville *et al.* [120] used PIV measurements to reveal discontinuous velocity profiles $v_x(y)$ across the gap of the Couette cell, for shear rates corresponding to the stress plateau. These profiles were composed of two linear regions, supporting different local shear rates in two coexisting bands, with high fluctuations of the flow field inside the high shear band [142]. Decruppe *et al.* [118] were the first to characterize the structure of the banded state by employing flow birefringence experiments. They reported the evolution of a highly birefringent band for concentrated CTAB solutions ($c_{\text{surf}} = 600$ mM) that nucleated on the moving inner cylinder of a Couette cell at the first critical shear rate. For concentrated samples, this new phase exhibited long range orientation, indicating an isotropic-to-nematic phase transition. This band broadened with increasing shear rate, until it filled the whole gap at the second critical shear rate. For semi-dilute solutions, the surfactant concentration is too low for such a phase transition [144]. Instead, shear-induced concentration fluctuations result in coexisting shear bands that consist of a fluidic phase, with strongly aligned micelles, and a more viscous phase with nearly isotropic entangled microstructure [145]. Time-resolved rheo-optical measurements on semi-dilute micellar solutions revealed that the interface between the coexisting bands along the vorticity direction was unstable, where turbid and non-turbid bands were separated by an undulating interface [121].

Besides the detailed studies of the gradient banding phenomenon, WLM system can also exhibit banding instabilities in vorticity direction. Although this feature was studied experimentally [7, 31, 53, 54, 56, 116, 117, 146, 147, 148, 149, 150, 151, 152], as well as theoretically [116, 135, 153], comparatively less is known about this instability. The constitutive flow curve of a vorticity banding flow curve is shown in Fig. 2.7(b). This non-monotonic, S-shaped flow curve exhibits a hysteretic regime with a multi-valued stress at one applied shear rate - a necessary condition for the existence of a stationary vorticity banded state [116]. In the hysteretic regime, i.e. a shear-thickening transition, bands with different internal microstructures (A and B in the inset in Fig. 2.7(b)) are stacked along the vorticity direction, i.e. the axial direction in a Couette cell.

A series of publications studied the rheology and banding instabilities of a semi-dilute micellar solution [53, 54, 56, 148]. They used an equimolar 40 mM CPyCl/NaSal solution that exhibited a complex flow curve: with increasing shear rate, the solutions showed a consecutive Newtonian flow behavior with a zero shear viscosity of $\eta_0 \approx 0.7$ Pa s, a shear-thinning regime, a sudden increase in viscosity due to SIS, followed by another shear-thinning regime. In the shear-thickening regime, clear and turbid rings were observed, stacked along the vorticity direction in a Couette cell, as probed by direct visualization and SALS measurements. SANS measurements showed that both bands contain strongly aligned structures [56]. Furthermore, huge oscillations in the measured quantities over time were observed during shear-thickening, demonstrating that the solutions never equilibrated and that SIS were formed and destroyed continuously over time. Similar fluctuations were observed for a CTAB/NaSal solution ($c_{\text{surf}} = 50$ mM, $R = 2$) that also showed shear-thickening [40]. Fielding [147] suggested that structuring in vorticity direction can also be triggered by a linear instability of one-dimensional gradient shear banded flow. Moreover, this vorticity banding phenomenon is not limited to surfactant solutions, but was also observed for dispersions of rodlike colloids in shear flow [154, 155].

Instabilities during elongational deformation

The flow behavior of complex fluids can be substantially different during elongational deformation than in shear flow, thus giving rise to unique flow instabilities in extension. Such phenomena were previously studied using microfluidic cross-slots, focusing on WLM solutions [156, 157, 158, 159]. Cross-slots consist of bisecting channels with two opposing inlets and two opposing outlets [160]. These geometries generate a planar elongational flow field with a centrally located stagnation point, similar to a four-roll mill device. However, microfluidic cross-slots enable to study instabilities in extension at high strain rates while inertia effects remain negligible due to the small channel length scales.

Surfactant solutions were first investigated in a microfluidic cross-slot by Pathak and Hudson [156]. They used a 30 mM CTAB/NaSal, $R = 8$ as well as a 100 mM CTAB/NaSal, $R = 0.6$ surfactant solution and employed PIV and FIB measurements to study the rheo-optical properties of WLM solutions in a planar elongational flow field. With increasing elongation rate $\dot{\epsilon}$ they observed the evolution of birefringence and transmittance bands due to the alignment of WLM in the extensional flow field. Increasing the flow rate further resulted in a broadening of the birefringent band and an asymmetric flow field developed, induced by the strong elasticity of the solutions.

Haward and McKinley [158] used similar CPyCl/NaSal solutions with $33 \leq c_{\text{surf}} \leq 100$ mM at a constant salt/surfactant ratio $R = 0.6$ and investigated the effect of surfactant concentration and ionic environment on the elongational flow behavior of WLM solutions. Employing PIV and measurement of the pressure drop as well as flow-induced birefringence they found that with increasing flow rate, the flow field transitioned from a steady symmetric to a steady asymmetric configuration with the emergence of a birefringent strand at a first critical Weissenberg number, which compares the elongation rate of the flow field with the fluid relaxation rate $Wi = \dot{\epsilon}\lambda$. If $\dot{\epsilon} > \lambda$, deformable microstructures, such as WLM and polymers, align and stretch in the flow field. Further increase of elongation rate resulted in a three dimensional, time dependent flow at a second critical Wi . Both critical Weissenberg numbers depended on the Reynolds number Re , which relates the inertial forces to the viscous forces of the fluid. Covering a broad range of flow rates, Haward and McKinley [158] established a stability diagram in Weissenberg-Reynolds number space for viscoelastic flows of complex fluids in a cross-slot geometry. Focusing on a 100 mM CPyCl/NaSal, $R = 0.6$, Haward *et al.* [159] reported similar results and additionally observed an increase of apparent extensional viscosity with elongation rate in the steady regime. They further found that in the asymmetric flow regime, upstream lip vortices develop in the inlet channels.

The first study regarding the flow behavior of more dilute surfactant solutions in a planar elongational cross-slot was performed by Dubash *et al.* [157]. They used two strongly viscoelastic, shear-thinning (100 mM, $R = 0.32$ and 75 mM, $R = 0.32$) as well as two weakly viscoelastic, slightly shear-thickening (75 mM, $R = 0.24$ and 50 mM, $R = 0.32$) CTAB/NaSal solutions. For the shear-thinning WLM solutions, flow transitioned from a steady symmetric to a steady asymmetric and eventually to an unsteady flow with increasing elongation rate, as reported before [156, 158, 159]. In contrast, the two shear-thickening samples did not exhibit a steady asymmetric

flow regime. Instead flow transitioned directly from the symmetric to the unsteady asymmetric branch and the authors argued that this is due to inertial effects ($Re \mathcal{O}(10)$). They further found that the critical Weissenberg numbers for the transitions increased with increasing elasticity number $El = Wi/Re$. However, Dubash *et al.* [157] did not report any correlation between flow-induced structuring and the observed flow instability in extension.

Recently, Dutta and Graham [161] presented a mechanistic constitutive model for surfactant solutions with flow-induced structure formation. The model predicts a multivalued stress at one global deformation rate in both shear and uniaxial extension, as schematically shown in Fig. 2.7(b). Although their predictions in extension matched the viscosity measurements obtained in early experiments by Prud'homme and Warr [78] in a opposed jet device, experimental evidence for a multivalued relation between stress and strain rate in extension is still missing.

2.3 Conclusions

Surfactant molecules have the ability to self-assemble in aqueous solution into various morphologies. The rheological behavior of long, semi-flexible aggregates, so called wormlike micelles, is particularly well documented. In bulk shear experiments WLM systems exhibit shear-thinning at sufficient surfactant and salt concentration and can undergo a transition from a homogeneous to an unstable flow at a critical shear rate or shear stress. This shear banding instability is characterized by a shear stress plateau in bulk rheometry, where the flow splits into multiple coexisting bands along the gradient direction, bearing different internal structures. Further, WLM solutions show strain hardening in extensional flows, as probed by FiSER and CaBER experiments. In planar extension, using microfluidic cross-slots, these systems show an elastic instability with the emergence of a birefringent strand, indicating micellar orientation in the extensional flow field. Here, a transition from a steady symmetric to a steady asymmetric flow is observed.

On the other hand, dilute surfactant solution that consist of short, rigid, rodlike micelles display a distinctly different rheological behavior. In shear experiments, dilute surfactant solutions exhibit a Newtonian flow regime with a zero shear viscosity close to water, followed by a shear-thickening region with a drastic increase of viscosity by more than one order of magnitude. This phenomenon is attributed to a shear-induced structure (SIS) formation that can lead to banding in vorticity direction in shear experiments. In uniaxial free-surface flow, e.g. CaBER experiments, filament lifetimes of several minutes can be observed, orders of magnitude larger than expected. In order to explain this phenomenon, a elongation-induced structure (EIS) buildup was proposed without further evidence, leading to a growth of micellar length and to the formation of a viscoelastic network. Experiments of similar shear-thickening surfactant solutions in planar extension show a transition from a steady symmetric to an unsteady asymmetric flow field. However, these solution are weakly viscoelastic in contrast to solutions that show unexpected long filament lifetimes in CaBER experiments.

2.3.1 Research objectives, scope and limitations

Although, the flow behavior of surfactant solution was thoroughly investigated in the past decades as summarized above, some aspects and questions still remain unanswered. In an effort to fill this remaining knowledge gap, we address the following aspects in this work:

- The most puzzling observation clearly is the anomalously long filament lifetime of dilute surfactant solution in CaBER experiments, as reported by Sachsenheimer *et al.* [5] and Omidvar *et al.* [6]. We therefore want to answer the question: How can such low viscosity solutions form such stable filaments, orders of magnitude larger than expected and does a viscoelastic, elongation-induced network of long micelles form inside the filament?
- Additionally, under which conditions do long lasting filaments form in CaBER experiments? More precisely, what are the necessary requirements in term of geometrical (D_0 , h_i , h_f) and stretching (t_s) parameters in CaBER experiments? Further, what is the influence of the surrounding phase, e.g. the surface tension (Γ), on the filament lifetime of these dilute surfactant solution? Do long lasting filaments form during other free-surface flows, e.g. filament stretching or dripping-onto-substrate experiments?
- Is the phenomenon of long filament lifetimes related to a flow instability during extensional deformation? If this hypothesis holds, what are the critical conditions in terms of elongation rate and total strain for this instability to arise in an elongational flow?
- Further, can we relate the observations in extension to the flow behavior in shear to provide a unifying framework for flow instabilities of dilute surfactant solutions in different flow kinematics? Is this phenomenon limited to surfactant solutions, or does it also govern the breakup of other low viscosity fluid filaments?

A plethora of surfactant systems were studied in the past, in various combinations with different salts and additives [12]. Here, we focus our investigations on four most commonly studied surfactant/salt mixtures and cover a broad range of surfactant concentration and salt/surfactant ratio. Furthermore, rheological features such as the onset of shear-induced structure buildup depend dramatically on environmental conditions, such as temperature [162]. However, these effects are not investigated here and all experiments are performed at $T = 20^\circ\text{C}$.

Structural transitions are often studied using SALS and SANS methods. However, these techniques generally involve comparatively large beamsizes (e.g. $2 \times 2 \text{ mm}^2$ for SANS) and require long acquisition times. The transient nature of filament thinning processes with thin fluid thread (e.g. $D < 1 \text{ mm}$) does not allow to employ such methods. Therefore, we characterize flow-induced structural transitions in extension using a planar cross-slot in combination with flow-induced birefringence imaging techniques, which allows us to detect changes in micellar orientation with high spatial $\mathcal{O}(10^{-3} \text{ m})$ and temporal $\mathcal{O}(10^{-3} \text{ s})$ resolution.

3 Materials

Chapter 3 provides a brief introduction of the investigated surfactant systems and their most important shear rheological properties. First, we examine the steady shear behavior of surfactant solutions, covering a broad range of surfactant and salt concentrations. Second, we focus on a representative dilute CTAB/NaSal solution, exhibiting shear-induced structure buildup. We then briefly address the pivotal question if very dilute surfactant solutions, such as the chosen representative sample, exhibit any elastic properties in small-amplitude oscillatory shear measurements.

3.1 Surfactant systems and sample preparation

In this thesis, we study the shear and elongational flow behavior of aqueous surfactant solutions, using the four commonly studied cationic surfactants hexadecyltrimethylammonium bromide (CTAB), hexadecylcetylpyridinium chloride (CPyCl), hexadecyltrimethylammonium chloride (CTAC) and hexadecyltrimethylammonium p-toluene sulfonate (CTAT). The molecules of these surfactants consist of the same hydrophobic tail, but have different headgroups and different counterions, or charged counter-molecules in the case of CTAT (see Fig. 3.1(a) and (b)).

At low concentrations, these systems form short, rodlike micelles and show shear-thickening behavior due to shear-induced structure buildup [30, 31, 32]. Depending on surfactant and salt concentration, they may also exhibit banding phenomena in shear flow [12, 13]. At higher surfactant and salt concentration all four of the systems can form long, semi-flexible, wormlike micelles. Furthermore, the formation of elongation-induced structures was proposed for CTAB [5] and CTAT [6] at low surfactant and salt concentration in uniaxial extension as well as for CTAB at high surfactant and salt concentration in planar elongational flows [106, 107, 111].

The salt sodium salicylate (NaSal) is added to solutions containing CTAB, CPyCl and CTAC, to enhance the anisotropic growth of micelles. Samples of CTAT are prepared with the addition of the salt sodium p-toluenesulfonate (NaTos) (see Fig. 3.1(c) and (d)). Materials are purchased as powders (Sigma Aldrich and Carl Roth) and are used without further purification. Aqueous solutions are prepared by dispersing weighted quantities of surfactant and salt in ultrapure water, covering surfactant concentrations of $5 \leq c_{\text{surf}} \leq 100$ mM and a broad salt/surfactant ratio $0 \leq R = c_{\text{salt}}/c_{\text{surf}} \leq 50$, depending on the surfactant system. Samples are shaken thoroughly for five days to assist dissolution. Subsequently, the solutions are stored at 20°C for one week to ensure the formation of equilibrium micellar structures.

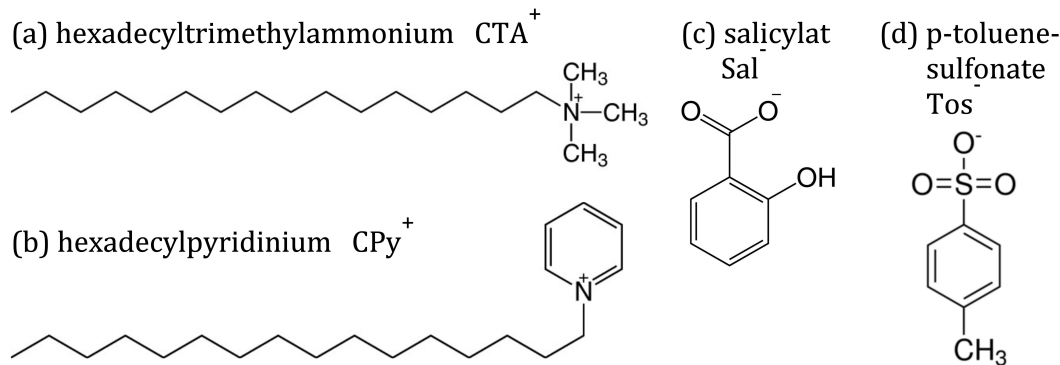


Figure 3.1: (a) and (b) Cationic surfactant molecules with the same hydrophobic tail but different hydrophilic headgroups, used in this study. (c) and (d) Structures of anionic salt ions.

In most parts of this thesis, we focus on a 10 mM CTAB/NaSal, $R = 0.5$ solution and on a 30 mM CTAB/NaSal, $R = 7.67$ solution, as representative examples for the flow behavior of surfactant solutions at low and high concentrations, respectively. A large variety of investigated surfactant systems shows similar properties in shear and elongational flows.

3.2 Shear rheological characterization

3.2.1 Steady shear measurements

Steady shear experiments are performed using a stress-controlled rotational rheometer (MCR 501, Anton Paar), equipped with a coaxial cylinder fixture (CC27, inner radius $R_i = 13.330$ mm, radii ratio $\delta = R_a/R_i = 1.0849$). We measure in controlled rate (CR) and controlled stress (CS) mode, increasing (up ramp) or decreasing (down ramp) the applied shear rate or shear stress, respectively. This allows for investigation of possible hysteresis phenomena in the shear-thickening regime of the flow curve [13, 41]. All measurements are performed at 20°C.

In our study, we cover a broad surfactant concentration of $5 \leq c_{\text{surf}} \leq 100$ mM and a salt/surfactant ratio $0 \leq R \leq 50$, depending on the surfactant system. Figure 3.2(a) exemplifies the dependency of the distinctive shear rheological behavior of surfactant solutions on the salt/surfactant ratio R . The figure shows the steady shear viscosity η of a series of 30 mM CTAB/NaSal solutions with different R as a function of shear rate $\dot{\gamma}$. Additionally, the zero shear viscosity η_0 is derived from steady shear experiments and plotted over the salt/surfactant ratio for a series of CTAB/NaSal solutions in Fig. 3.2(b). Here, the shape of the η_0 over R curve is directly related to the micellar morphology [21].

At small amounts of salt (e.g. $R = 0.2$ in Fig. 3.2(a)) the surfactant solution consists of small, globular micelles and exhibits purely Newtonian behavior with a viscosity close to that of water. For CTAB, spherical micelles form between the critical micelle concentrations $\text{CMC}_1 \approx 1$ mM and $\text{CMC}_2 \approx 270$ mM in the absence of additives [163].

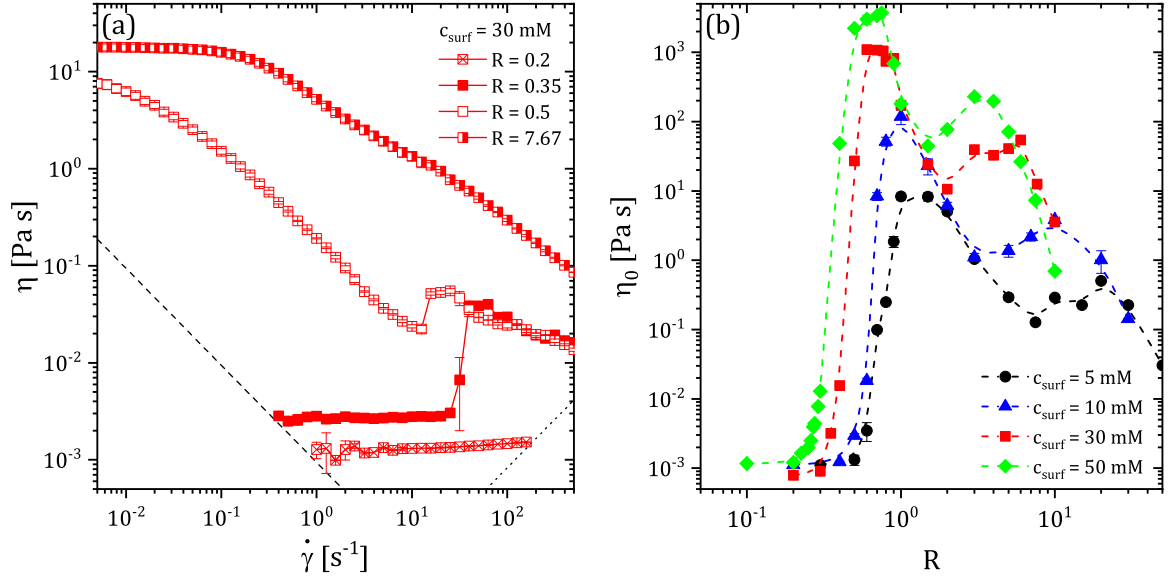


Figure 3.2: (a) Steady shear viscosity as function of shear rate for 30 mM CTAB/NaSal solutions with different salt/surfactant ratios. The dashed and the dashed-dotted black lines represent the minimum torque limit of the rheometer and the critical shear rate for the onset of secondary flows [39], respectively. (b) Dependency of zero shear viscosity on salt/surfactant ratio for four different CTAB/NaSal systems.

Increasing the salt content only slightly to $R = 0.35$ leads to the formation of short, rigid, rodlike micelles. This transition increases the low shear viscosity merely by a factor of two but changes the behavior at larger shear rates dramatically. At a critical shear rate $\dot{\gamma}_c \approx 30 \text{ s}^{-1}$ the viscosity increases by more than one order of magnitude due to shear-induced structure buildup. Upon further increase of shear rate, the viscosity passes through a maximum and subsequently shear-thinning sets in. At this critical salt/surfactant ratio, the addition of further NaSal screens the electrostatic repulsion of neighboring charged headgroups and promotes the anisotropic growth of long, semi-flexible wormlike micelles [22, 74]. These WLM entangle and promote viscoelasticity, thus leading to a sudden increase in the η_0 over R curve (Fig. 3.2(b)). These WLM solutions show shear-thinning behavior, prior to shear-thickening, as shown for 30 mM CTAB/NaSal, $R = 0.5$ in Fig. 3.2(a). The characteristic shape of the zero shear viscosity as a function of salt/surfactant ratio with its two maxima results from further changes of the micellar structures with increasing R [21, 164]. Solutions with high amounts of salt (e.g. $R = 7.67$ in Fig. 3.2(a)) consist of entangled and branched WLM and exhibit a Newtonian plateau, followed by a purely shear-thinning regime.

3.2.2 Shear-induced structure formation

Figure 3.3 shows the flow curve of a representative dilute, shear-thickening surfactant solution. We plot the shear stress τ as a function of shear rate $\dot{\gamma}$ for CR and CS, as well as for up and down ramp measurements. Here, three flow regimes can be distinguished in upward sweeps and in CR mode. First, at low rates, shear stress increases linearly with increasing shear rate, indicating Newtonian behavior with a

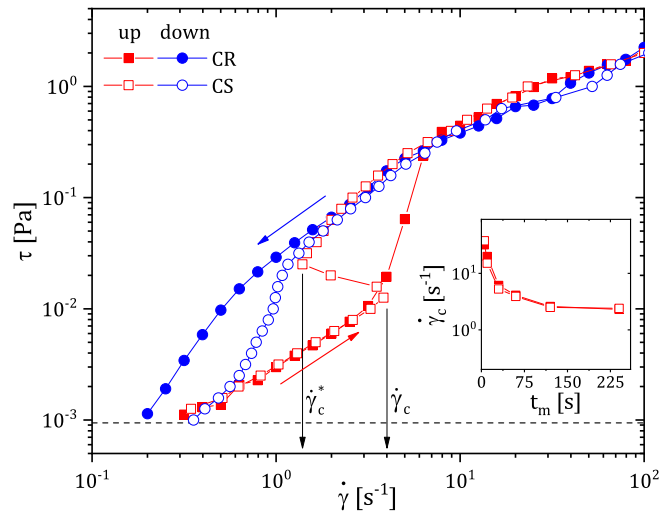


Figure 3.3: Steady shear data for a 10 mM CTAB/NaSal, $R = 0.5$ surfactant solution. The measurement time per point is $t_m = 125$ s. The dashed line represents the minimum torque limit of the rheometer. The inset shows the dependence of the critical shear rate at which the system starts to shear-thicken $\dot{\gamma}_c$ as a function of t_m .

zero shear viscosity of $\eta_0 \approx 3$ mPa s. At a critical shear rate $\dot{\gamma}_c \approx 4$ s $^{-1}$, the viscosity increases and shear-thickening sets in. Subsequently, the viscosity passes through a maximum, followed by shear-thinning behavior at shear rates $\dot{\gamma} > 10$ s $^{-1}$. In CR mode down ramp measurements, we observe a hysteresis in the flow curve, i.e. the shear-thickening state is extended by more than one order of magnitude towards smaller shear rates, before approaching the Newtonian regime again. For 10 mM CTAB/NaSal, $R = 0.5$, this regime is not accessible within the torque limit of the rheometer.

The hysteresis in the flow curve is also found in measurements in CS mode (open symbols in Fig. 3.3). Here, a re-entrant behavior with an S-shaped flow curve is observed between $\dot{\gamma}_c^* = 1.3$ s $^{-1}$ and $\dot{\gamma}_c = 4$ s $^{-1}$ following the Newtonian plateau at low rates. Note that in transient shear experiments at $\dot{\gamma} > \dot{\gamma}_c$, the formation of shear-induced structures, and thus the increase in viscosity, occurs after an induction period t_{ind} [45]. This induction time decreases with increasing shear rate [42, 44], resulting in a constant critical total deformation $\gamma_c = t_{\text{ind}} * \dot{\gamma}_c$. For the 10 mM CTAB/NaSal, $R = 0.5$ solution, a critical total deformation of $\gamma_c \approx 5 \times 10^3$ [165] is required besides $\dot{\gamma}_c$ for the onset of shear-thickening. Thus, the total deformation has to be taken into account in order to obtain reliable values of the critical shear rate. Therefore, we perform steady shear measurements, using 10 measuring points per decade and employing different time intervals per shear rate for each measurement point t_m . The critical shear rate for shear-thickening $\dot{\gamma}_c$ decreases with increasing time per measurement point t_m until it plateaus for $t_m > 75$ s, shown in the inset in Fig. 3.3. We choose $t_m = 125$ s in sweep experiments, to ensure that the critical total deformation γ_c necessary for the onset of shear-thickening at $\dot{\gamma}_c$ is reached.

Shear-thickening behavior is found in many dilute surfactant systems, attributed to the formation of SIS and different mechanisms were reported to explain the SIS phenomenon [42, 55]. The resulting non-monotonic flow curve (as exemplified in

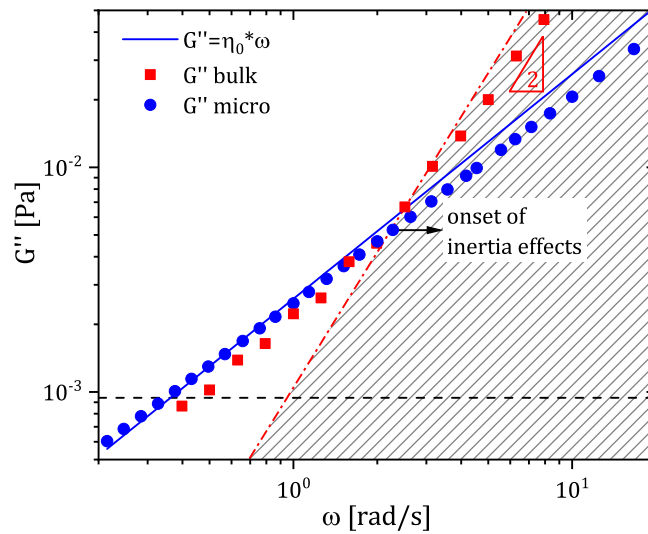


Figure 3.4: Loss modulus G'' of a 10 mM CTAB/NaSal, $R = 0.5$ solution determined through bulk SAOS measurements (red symbols) as well as using passive microrheology (blue symbols). The black dashed line indicates the minimum torque limit of the rheometer and the full blue line represents the viscous properties, calculated from the zero shear viscosity. The grey hatched area represents the onset of inertia effects and the red dashed-dotted line a slope of $\sim \omega^2$. *Reproduced with permission from Springer Nature [1].*

Fig. 3.3) is a necessary condition for the existence of a stationary vorticity banded state [7, 135, 153], where bands bearing different stresses are stacked along the vorticity direction, i.e. the axial direction in the Couette cell. Furthermore, these solutions show no apparent viscoelasticity in small-amplitude oscillatory shear (SAOS) measurements, as discussed in detail below.

3.2.3 Linear viscoelastic properties of dilute surfactant solutions

In an effort to determine the viscoelastic properties and a relaxation time for the dilute surfactant solutions in shear experiments, we employ SAOS as well as microrheological measurements. We perform SAOS experiments, using a strain amplitude of $\gamma_0 = 1\%$ in the linear regime and determine the elastic modulus G' and viscous modulus G'' in the frequency range of $0.1 \leq \omega \leq 50$ rad/s. Further, we perform passive microrheology by seeding the dilute surfactant solutions with 0.01 wt% of mono-disperse fluorescent polystyrene microspheres (Banglabs Inc.) of diameter $d_p = 0.96 \mu\text{m}$ and calculating the elastic and viscous modulus from the mean square displacement of the embedded particles, based on the generalized Stokes-Einstein relation [166, 167].

Figure 3.4 shows G'' as a function of ω obtained from bulk rheometry as well as microrheology. In both experiments, we do not observe any elastic response (i.e. G') and hence no characteristic cross-over of G' and G'' in the investigated frequency regime, within the experimental boundary conditions (see dashed black line for lower torque limit of the rotational rheometer). Additionally, we calculate G'' from the zero shear

viscosity as $G'' = \eta_0 \omega$ (full blue line). The viscous modulus from microrheology is close to G'' calculated from η_0 , indicating purely viscous behavior at small deformations. At higher frequencies (see grey hatched area in Fig. 3.4), G'' derived from SAOS measurements deviates from the microrheological results and the apparent modulus increases close to $G'' \sim \omega^2$ (red dashed-dotted line), indicating the onset of instrument-inertia effects in bulk measurements [39]. Hence, we cannot measure any elasticity for the representative very dilute 10 mM CTAB/NaSal, $R = 0.5$ solution and we do not find a characteristic relaxation time in the frequency range of $0.1 \leq \omega \leq 50$ rad/s. However, due to the complex microstructure of the solution, a non-zero relaxation time should exist and we estimate this relaxation time to be smaller than $\lambda \ll 0.02$ s, in accordance with microrheological measurements of similar low viscosity, shear-thickening, yet weakly elastic surfactant solutions [77].

3.3 Conclusions

The shear rheological properties of surfactant solutions strongly depend on surfactant concentration c_{surf} and salt/surfactant ratio R . At a constant surfactant concentration, the addition of penetrating salts such as NaSal leads to a pronounced anisotropic growth in micellar length, which dramatically influences the steady shear rheology. In the investigated surfactant concentration regime of $5 \leq c_{\text{surf}} \leq 100$ mM, solutions at very small R consist of small, globular micelles and show Newtonian flow behavior with a viscosity close to that of water. On the other hand, samples with high R exhibit a zero shear viscosity orders of magnitudes larger than that of water with a subsequent shear-thinning regime. These solutions consist of long, wormlike micelles that entangle and cause viscoelasticity.

One of the most puzzling phenomena is the shear-thickening effect of dilute surfactant solutions at small R . These solutions show a Newtonian flow regime at small shear rates with a zero shear viscosity close to that of water, e.g. $\eta_0 \approx 3$ mPa s for a 10 mM CTAB/NaSal, $R = 0.5$, followed by a sudden increase in viscosity by more than one order of magnitude. This shear-thickening transition arises at a critical shear rate as well as a critical total deformation and is characterized by a hysteretic flow curve. The shear rheological properties of these systems were investigated before and the shear-thickening was linked to SIS formation and to the emergence of a vorticity banding instability. However, the flow behavior of these systems in elongation remains largely unknown and is thoroughly investigated in this thesis.

4 Filament Formation and Breakup in Uniaxial Extension

In this chapter, we probe the uniaxial flow behavior of surfactant solutions. Therefore, we investigate the macroscopic formation and subsequent thinning of free surface surfactant filaments in CaBER experiments. Here, we examine the influence of interfacial tension and viscosity ratio between sample and surrounding phase, as well as geometrical and stretching conditions on the filament formation and breakup. Further, we introduce two additional filament stretching methods and demonstrate generically how dilute surfactant solutions form remarkably long filaments.

4.1 Experimental

4.1.1 Capillary breakup elongational rheometry

The capillary breakup elongational rheometer (CaBER) is commonly used as a versatile tool to study the elongational flow behavior of low viscosity and viscoelastic fluids. In principle, the evolution of an unstable liquid bridge over time is monitored to determine fundamental fluid properties such as extensional viscosity and relaxation time [168, 169, 170, 171, 172]. Necking and subsequent breakup of the fluid thread are driven by capillarity and resisted by inertia as well as by viscous and elastic stresses inside the fluid. Depending on the interplay between these forces, different modes of capillary thinning and breakup can arise (see McKinley [173] for a comprehensive review). The characteristic breakup of slender liquid filaments is considered a benchmark for the elongational flow properties of liquids and their kinematics are assumed to approximate an ideal homogeneous, uniaxial flow field inside the thinning filament.

Here, surfactant solution properties in uniaxial extension are probed using a commercial CaBER (Thermo Scientific). The setup is extended with an optical train, consisting of a high-speed camera (Fastcam-X 1024 PCI, Photron), a telecentric objective (TC4M 16, 1 \times , MaxxVision) and blue telecentric backlight illumination (TZb30, Vision & Control). In CaBER experiments, the sample is placed between two circular plates with diameter D_0 , separated by an initial height h_i . During a step stretch, the upper plate is moved upwards to a final height h_f within the strike time t_s , schematically shown in Fig. 4.1. Subsequently, the evolution of the minimal filament diameter $D_{\min}(t)$ over time is monitored and the apparent extensional viscosity and elongational relaxation time of the fluid can be derived based on the premise of homogeneous elongational deformation [103, 174, 175]. If a cylindrical filament is formed, such as in

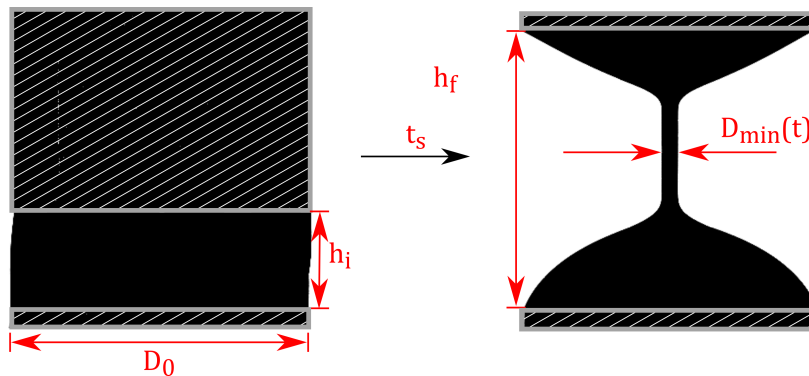


Figure 4.1: Schematic representation of the initial (left) and final (right) displacement during the step stretch in CaBER experiments. The two circular plates have a diameter of D_0 and are separated from an initial height h_i to a final height h_f within the strike time t_s . Hatched areas indicate the lower and upper plates.

Fig. 4.1, we use $D(t) \equiv D_{\min}(t)$. Choosing plates with a diameter of $D_0 = 6$ mm, an initial height of $h_i = 1.5$ mm and a final height of $h_f = 6$ mm, allows characterizing the thinning process of surfactant solutions in a broad range of surfactant and salt concentration [5]. If not mentioned otherwise, we use these parameters in the shown CaBER experiments. In order to examine the influence of stretching conditions on filament thinning, we further probe a broad range of geometrical configurations (i.e. $4 \leq D_0 \leq 8$ mm, $0.5 \leq h_i \leq 2$ mm and $4 \leq h_f \leq 14$ mm) as well as different stretching times (i.e. $40 \leq t_s \leq 5000$ ms). In our CaBER experiments, the diameter of the thinning fluid filament is monitored as a function of time and the filament lifetime t_{fil} , i.e. the time when the filament ruptures, is determined.

4.1.2 Dripping-onto-substrate and filament stretching experiments

To demonstrate the unique flow behavior of dilute surfactant solutions in uniaxial extension, we use two methods to create remarkably long filaments. First, we observe how a drop detaches due to gravity from a blunt needle with diameter $D_n = 1.65$ mm, forming a long filament while falling down. Second, a cylindrical piston with diameter D_p is immersed by depth H in a larger surfactant fluid reservoir and withdrawn from it by moving upwards with a constant velocity v_p , using a linear motor (Texture Analyzer TA.XTplus, Stable Micro System). We examine the filament formation and breakup using different cylindrical pistons with $4 \leq D_p \leq 8$ mm, different immersion depths $0 \leq H \leq 25$ mm (where in the case of $H = 0$ mm, the cylinder is just slightly in contact with the sample surface) and different piston velocities $1 \leq v_p \leq 10$ mm/s. The diameter as a function of time as well as the filament lifetime t_{fil} are recorded and are compared with the data obtained from CaBER measurements.

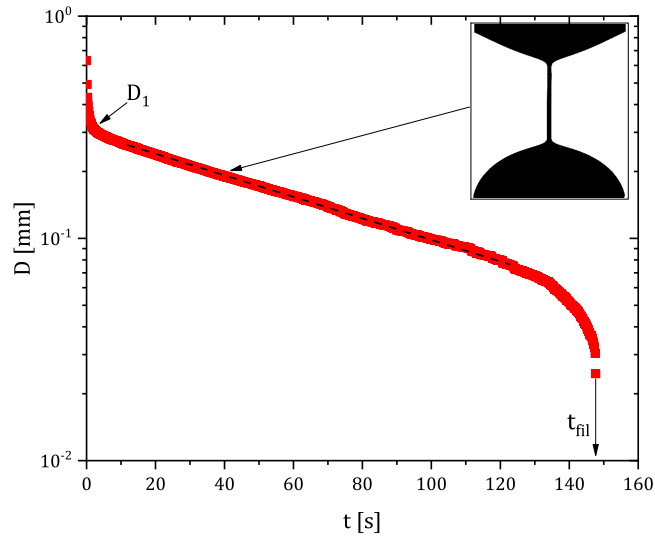


Figure 4.2: Filament thinning results of a 10 mM CTAB/NaSal, $R = 0.5$ surfactant solution as probed by CaBER. Diameter as a function of time with $h_i = 1.5$ mm, $h_f = 6$ mm and $t_s = 40$ ms in air. The inset picture shows a snapshot of the cylindrical filament at $t = 40$ s. *Reproduced with permission from Springer Nature [1].*

4.2 Results and discussion

4.2.1 Filament thinning in CaBER

Figure 4.2 shows the typical thinning behavior of low concentrated surfactant solutions in uniaxial elongation. Here, we plot the minimum filament diameter as a function of time. During the strike time t_s , the sample is stretched from the initial height h_i to the final height h_f . After the top plate reaches its final position h_f at $t = 0$, the filament thins rapidly up to a diameter of $D_1 \approx 0.3$ mm, forming a cylindrical thread (see insert in Fig. 4.2). This initial fast thinning is followed by a slow thinning period until the filament ruptures at t_{fil} . Although, this 10 mM CTAB/NaSal, $R = 0.5$ solution exhibits a low shear viscosity of merely $\eta_0 \approx 3$ mPa s with no apparent viscoelasticity as probed by SAOS measurements, the sample shows a remarkably long filament lifetime of $t_{\text{fil}} \approx 150$ s in uniaxial extension.

In Fig. 4.2, the filament diameter seems to decrease exponentially in the region between $10 \leq t \leq 120$ s, indicated by the dashed black line. This could be interpreted as an elasto-capillary thinning regime and one might naively derive an extensional relaxation time λ_e from the slope of the diameter over time curve based on the assumption that kinematics approximate an ideal homogeneous uniaxial flow field inside the thinning filament. However, as we will show in chapter 5, this is not the case for the dilute surfactant solution shown in Fig. 4.2 and we therefore do not calculate λ_e from CaBER data.

Further, we determine the filament lifetime ratio $t_{\text{fil}}/t_{\text{fil,N}}$ that compares the lifetime in CaBER experiments t_{fil} with the theoretical filament lifetime $t_{\text{fil,N}}$ calculated from the zero-shear viscosity of the solution assuming Newtonian flow behavior [104, 105].

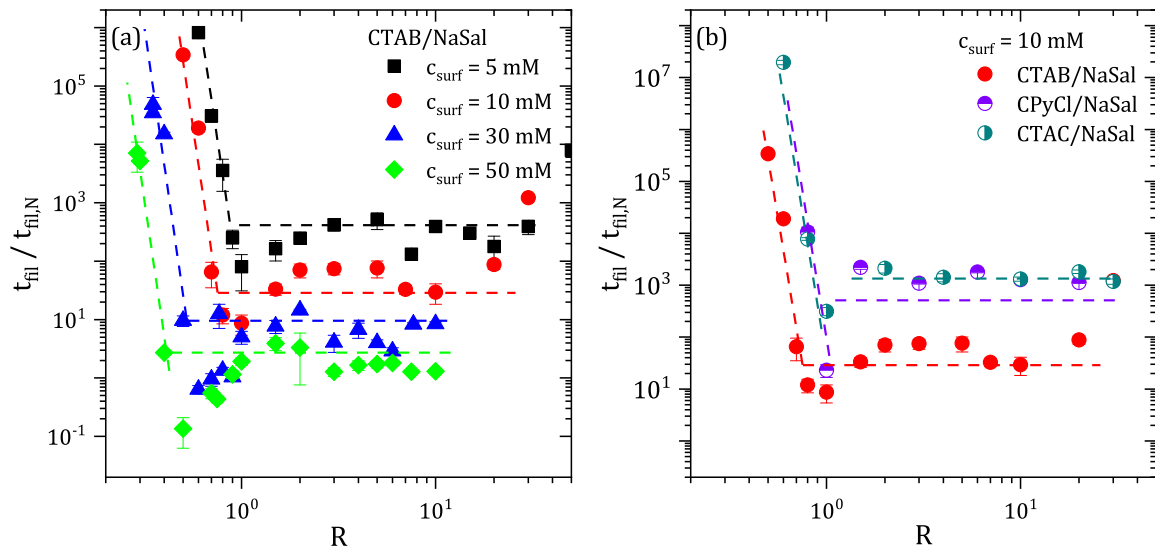


Figure 4.3: Filament lifetime ratio $t_{\text{fil}}/t_{\text{fil},N}$ as a function of salt/surfactant ratio R for (a) four different CTAB/NaSal systems and (b) for three different surfactant systems with $c_{\text{surf}} = 10$ mM.

For Newtonian fluids, the diameter decreases linearly over time (see Eq. 4.1), driven by surface tension Γ and resisted by viscous forces, i.e. the zero shear viscosity η_0 .

$$D(t) = D_1 - \Theta \frac{\Gamma}{\eta_0} t \quad (4.1)$$

D_1 in Eq. 4.1 is the diameter of the filament when the top plate reaches its final position h_f , and Θ is a numerical prefactor. Depending on whether inertia is neglected or not, different values of Θ were reported based on experimental observations as well as on numerical predictions [104, 105, 176, 177, 178]. In the case of negligible inertia $\Theta = 0.1418$ [104].

In our study, we find huge filament lifetime ratios for the investigated low concentrated solutions on the order of 10^3 to 10^8 , shown in Fig. 4.3. Upon increasing the salt/surfactant ratio R , the filament lifetime ratio $t_{\text{fil}}/t_{\text{fil},N}$ decreases dramatically until it plateaus. The absolute value of $t_{\text{fil}}/t_{\text{fil},N}$ in this plateau region increases with decreasing surfactant concentration c_{surf} (Fig. 4.3(a)), e.g. $t_{\text{fil}}/t_{\text{fil},N} \approx 400$ and $t_{\text{fil}}/t_{\text{fil},N} \approx 2$ for 5 mM CTAB/NaSal and 50 mM CTAB/NaSal, respectively. Further, the $t_{\text{fil}}/t_{\text{fil},N}$ curves are shifted towards smaller R values upon increase of surfactant concentration.

Long lasting filaments of low concentrated solutions were reported previously for CTAB/NaSal and CPyCl/NaSal solutions [5], as well as for CTAT solutions [6], and were attributed to the formation of elongation-induced structures. Our results extend this list by adding CTAC/NaSal as another system showing long t_{fil} and $t_{\text{fil}}/t_{\text{fil},N}$ at low salt and surfactant concentration (Fig. 4.3(b)), e.g. the 10 mM CTAC/NaSal $R = 0.6$ solution with a zero shear viscosity of $\eta_0 = 2$ mPa s exhibits a filament lifetime of $t_{\text{fil}} \approx 85$ s in CaBER experiments. A minimum zero-shear viscosity $\eta_0 \approx 2 - 3$ mPa s, a minimum initial diameter $D_1 \approx 0.3$ mm and a minimum total strain $\varepsilon \approx 5$ are required to create long lasting filaments.

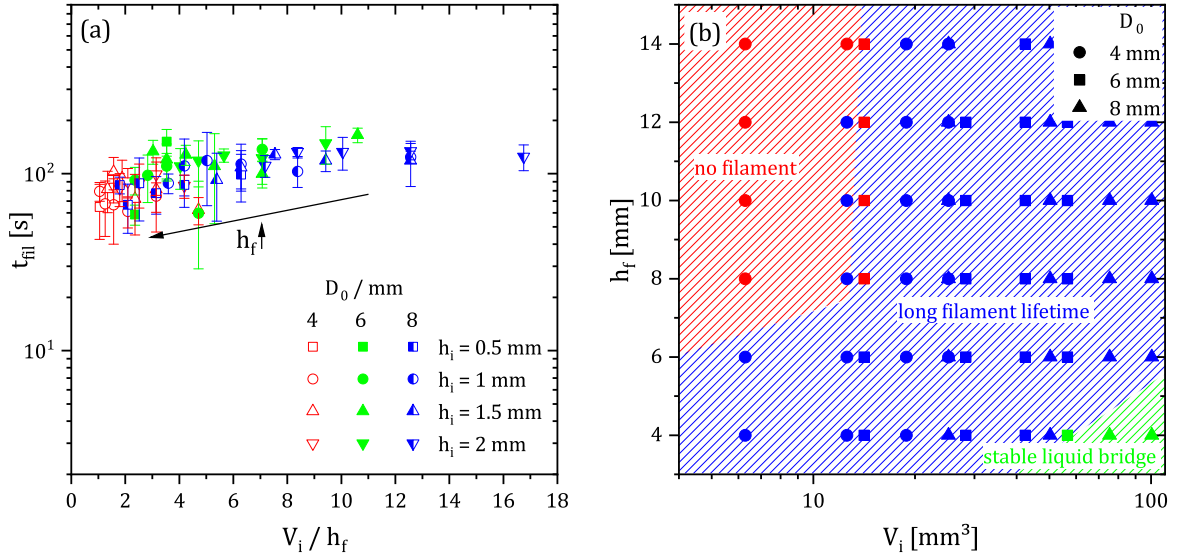


Figure 4.4: Influence of geometrical parameters in CaBER experiments on the formation of long living filaments. Results are shown for a 10 mM CTAB/NaSal, $R = 0.5$ dilute surfactant solution and a strike time of $t_s = 40$ ms is used. (a) Filament lifetime t_{fil} as a function of initial volume divided by final height for three different plate diameters D_0 and four different initial heights h_i . Final height varies between $4 \leq h_f \leq 14$ mm. (b) Occurrence of long filament lifetimes in the parameter space of h_f and V_i . Different shaped symbols represent different initial plate diameters D_0 . Red, blue and green symbols and hatched areas indicate when no filaments form, when long filament lifetimes are observed, and when a stable liquid bridge is formed.

4.2.2 Influence of stretching conditions and surrounding phase on filament thinning behavior

Geometric configurations can have an influence in the breakup process of liquid filaments. Here, we investigate the filament thinning behavior in CaBER experiments varying the initial height $0.5 \leq h_i \leq 2.5$ mm, the final height $4 \leq h_f \leq 14$ mm and the plate diameter $4 \leq D_0 \leq 8$ mm, while the strike time is kept constant at $t_s = 40$ ms. Figure 4.4(a) shows the influence of these geometrical parameters in CaBER experiments on the formation of long living filaments for a 10 mM CTAB/NaSal, $R = 0.5$ dilute surfactant solution. We plot the filament lifetime as a function of initial volume V_i divided by the final height h_f , with $V_i = \pi D_0^2 h_i / 4$. The filament lifetime is nearly independent of V_i/h_f at $t_{\text{fil}} \approx 120$ s. If the sample is stretched from a very small initial volume, e.g. with $D_0 = 4$ mm and $h_i = 0.5$ mm, to a large final height, e.g. $h_f = 6$ mm, the filament lifetimes decrease to $t_{\text{fil}} \approx 70$ s. The decrease of V_i/h_f results in a smaller diameter D_1 after the step stretch (see Fig. 4.2), thus leading to smaller t_{fil} . However, this filament lifetime is still orders of magnitude larger than expected. In contrast to our observations, Kim *et al.* [97] found a strong dependence of stretching conditions on the filament thinning behavior of surfactant solutions. They investigated a 100 mM CTAB/NaSal, $R = 0.5$ solution in 100 mM NaCl brine, using CaBER and varying the final height and the plate diameter while keeping the initial

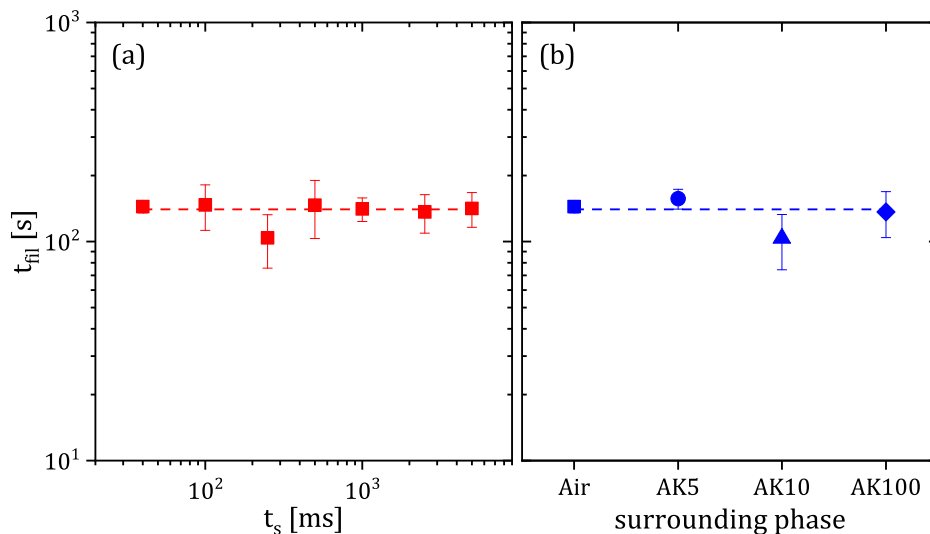


Figure 4.5: Influence of (a) strike time t_s and (b) surrounding phase on the filament lifetime t_{fil} of a 10 mM CTAB/NaSal, $R = 0.5$ surfactant solution in CaBER experiments. *Reproduced with permission from Springer Nature [1].*

height constant. The authors reported an increase of filament lifetime with increasing final aspect ratio $\Lambda_f = h_f/D_0$ for this higher concentrated sample.

In Fig. 4.4(b) we summarize the occurrence of long-lasting filaments during CaBER experiments, in the parameter space spanned by final height h_f and initial sample volume V_i for the same sample shown in Fig. 4.4(a). If the initial volume is small, e.g. $V_i \approx 6 \text{ mm}^3$, and the sample is stretched to a large final height, e.g. $h_f = 14 \text{ mm}$, the fluid thread ruptures during the initial step stretch and no filament is formed (hatched red area). On the other hand, when the initial volume is large, e.g. $V_i \approx 100 \text{ mm}^3$, and the sample is stretched to a small final height, e.g. $h_f = 4 \text{ mm}$, a stable liquid bridge forms (hatched green area). This bridge generally does not form a cylindrical filament. In between these two regimes, we find long-lasting filaments with $t_{\text{fil}} \approx 120 \text{ s}$ (hatched blue area), independent of stretching ratio (i.e. D_0 , h_i and h_f) as long as conditions are such that cylindrical filaments can be formed. The blue symbols in Fig. 4.4(b) correspond to the data shown in Fig. 4.4(a). Our results are in agreement with Sachsenheimer *et al.* [5], who introduced a similar map. They further found that a critical diameter D_1 after the step stretch is required for the formation of long-lasting filaments. Similarly, we observe that a critical diameter of $D_1 \approx 0.3 \text{ mm}$ is required, as discussed earlier. D_1 decreases with decreasing V_i/h_f , thus smaller filament lifetimes are observed for small V_i/h_f , as shown in Fig. 4.4(a).

Furthermore, stretching conditions during the initial step stretch in CaBER experiments can influence filament thinning and thus t_{fil} [179]. Therefore, we probe the uniaxial flow behavior covering a broad range of strike time $40 \leq t_s \leq 5000 \text{ ms}$. Using long strike times minimizes the disturbance of the capillary thinning process, similar to the slow retraction method (SRM) introduced by Campo-Deaño and Clasen [180]. Here, we find that the filament lifetime in CaBER experiments does not depend on the

strike time t_s , as shown in Fig. 4.5(a).

The surface or interfacial tension between the fluid sample and the surrounding phase acts as a dominant mechanism for thinning of the liquid thread in capillary-driven breakup experiments [38]. Here, we perform CaBER experiments in different oils as surrounding phases, using a customized transparent cell that encloses the CaBER plates and the fluid sample. The cell is filled with Newtonian polydimethylsiloxane (PDMS) oils with different viscosities (AK5 $\eta_0 \approx 5$ mPa s, AK10 $\eta_0 \approx 10$ mPa s and AK100 $\eta_0 \approx 100$ mPa s, Wacker Chemie AK), resulting in a range of viscosity ratio between the surfactant solution and the PDMS oil ($0.03 \leq \eta_0^{\text{surf}}/\eta_0^{\text{oil}} \leq 0.6$). The interfacial tension between the dilute surfactant solution and the air is $\Gamma = 32.90 \pm 0.12$ mN/m and between the dilute surfactant solution and PDMS $\Gamma = 4.08 \pm 0.14$ mN/m. Interfacial tensions are measured using a drop shape analyzer (DSA100, Krüss) and are independent of surfactant and PDMS oil type, as well as surfactant and salt concentration. Surfactant solution properties are summarized in Table 4.1 for one representative low and one representative high concentrated surfactant solution.

Table 4.1: Material parameters for a representative low concentrated surfactant solution (10 mM CTAB/NaSal, $R = 0.5$) and for one representative high concentrated surfactant solution (30 mM CTAB/NaSal, $R = 7.67$).

c_{surf} [mM]	R	ρ [g/cm ³]	Γ_{air} [mN/m]	Γ_{AK5} [mN/m]	Γ_{AK10} [mN/m]	Γ_{AK100} [mN/m]
10	0.5	0.995 ± 0.002	32.90 ± 0.12	4.15 ± 0.07	3.93 ± 0.02	4.18 ± 0.49
30	7.67	1.011 ± 0.001	32.79 ± 1.57	3.05 ± 0.34	3.44 ± 0.16	4.31 ± 0.42

For solutions at low concentrations, the filament lifetime is independent of the interfacial tension Γ between the surfactant filament and the surrounding phase. In Fig. 4.5(b), we plot the filament lifetime t_{fil} for different surrounding phases as blue symbols. Long lasting filaments can be created in all investigated surrounding phases and t_{fil} neither depends on Γ nor on $\eta_0^{\text{surf}}/\eta_0^{\text{oil}}$ between the two fluids, within experimental error.

4.2.3 Formation of long surfactant filaments

The experiments illustrated in Fig. 4.6 demonstrate the unique flow behavior of low concentrated surfactant solutions in uniaxial extension. In Fig. 4.6(a), a small droplet of a 10 mM CTAB/NaSal, $R = 0.5$ solution detaches from a syringe and creates a long filament while falling down, which starts to thin. However, the fluid thread does not rupture quickly but forms a long filament longer than 10 cm (black bar on the left of Fig. 4.6).

A similar phenomenon is shown in Fig. 4.6(b). Here, a cylindrical piston is withdrawn with a constant velocity $v_p \approx 3$ mm/s from a larger reservoir of dilute 10 mM CTAB/NaSal, $R = 0.5$ solution. Again, the formation of a slender, long filament is observed, until the fluid thread breaks at a remarkable length (e.g. $\gg 10$ cm, as indicated by the black bar on the right in Fig. 4.6(b)).

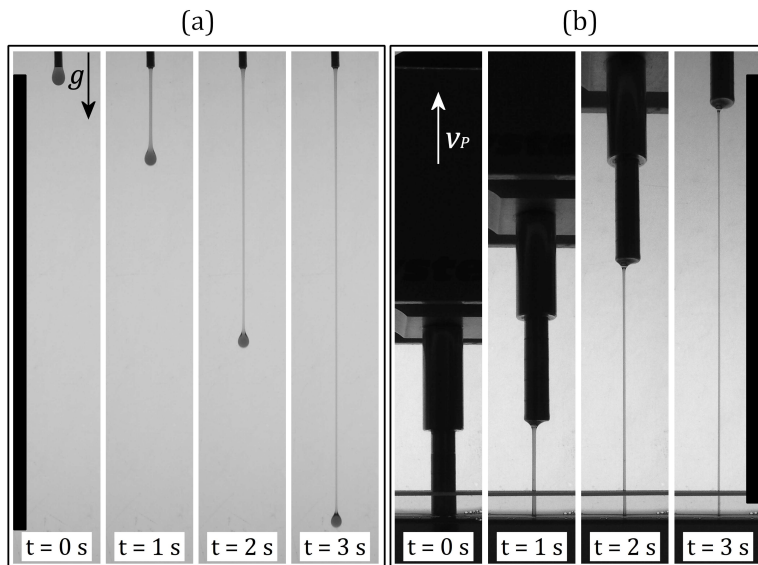


Figure 4.6: Series of snapshots showing the formation of long filaments using a 10 mM CTAB/NaSal, $R = 0.5$ dilute surfactant solution. (a) A drop detaches due to gravity from a blunt needle with diameter $D_n = 1.65$ mm, forming a long lasting filament. (b) Cylindrical piston with diameter $D_p = 6$ mm moves upwards with a constant velocity $v_p \approx 3$ mm/s and creates a fluid thread. The black area at the bottom indicates the fluid reservoir. Bars on the left and right of both panels represent a length of 10 cm. *Reproduced with permission from Springer Nature [1].*

We probe the influence of geometrical (i.e. D_p and H) as well as stretching conditions (i.e. v_p) on the formation of such long filaments, as shown in Fig. 4.6. In Fig. 4.7, the filament lifetime is plotted as a function of initial filament diameter D_1 that forms as soon as the piston exits the reservoir. For the sake of clarity, we only show results for one piston ($D_p = 6$ mm) and two piston velocities ($v_p = 1$ mm/s and $v_p = 10$ mm/s). For the smaller piston velocity $v_p = 1$ mm/s, the filament lifetime increases strongly with increasing initial diameter, similar to the results obtained in CaBER experiments. If the immersion depth of the piston in the filament stretching experiments is too small, e.g. $H = 0$ mm, the initial diameter is small and the filament quickly ruptures. Increasing the immersion depth above $H \geq 5$ mm results in larger D_1 and thus t_{fil} increases. On the other hand, the dependency of the filament lifetime on the initial diameter for the higher piston velocity $v_p = 10$ mm/s is much weaker. Although, filaments with a large D_1 form as soon as the piston emerges from the reservoir, the filament quickly breaks while the piston moves upwards with a fast velocity and thus t_{fil} is much smaller than for $v_p = 1$ mm/s. In these experiments, the filament breakup depends on the stretching conditions (i.e. v_p), in contrast to Fig. 4.5(a). In the CaBER experiments shown in Fig. 4.5(a), the fluid is stretched within different strike times t_s during the initial step stretch, while the filament subsequently thins, driven by surface tension and not by other external forces. On the other hand, in the filament stretching experiments shown in Fig. 4.7, the fluid is constantly stretched by moving the piston upwards. This effect increases with increasing piston velocity. In this case, the superposition of filament stretching and surface tension driven thinning leads to a faster filament breakup, hence

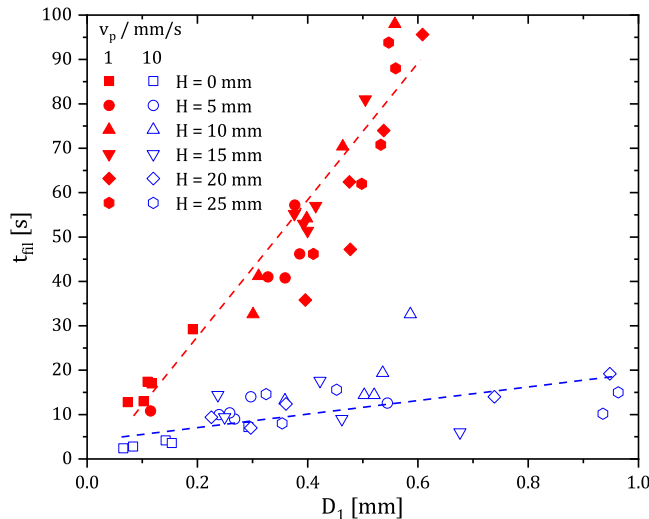


Figure 4.7: Filament lifetime t_{fil} of a 10 mM CTAB/NaSal, $R = 0.5$ solution as a function of initial filament diameter D_1 , derived from filament stretching experiments (shown in Fig. 4.6(b)) for different piston velocities v_p and immersion depths H . Here, a cylindrical piston with diameter $D_p = 6$ mm is used. Dashed lines are to guide the eye.

to smaller t_{fil} . Similar results are found for the other investigated piston diameters and velocities.

Furthermore, we use the method displayed in Fig. 4.6(a) to perform dripping-onto-substrate (DoS) experiments, similar to Dinic *et al.* [181], by introducing a glass slide below the tip of the blunt needle at a certain displacement $1 \leq h_f \leq 10$ cm and determine the filament lifetime t_{fil} . Figure 4.8 shows t_{fil} as a function of final displacement h_f between needle and glass plate. The thinning process and thus t_{fil} is independent of final displacement h_f (i.e. filament length) within experimental error. Further, the filament lifetime in DoS experiments matches t_{fil} obtained in CaBER measurements, as indicated by the hatched red area in Fig. 4.8. In contrast, Omidvar *et al.* [98] found that extensional relaxation times, hence t_{fil} measured in CaBER experiments were smaller than obtained by the DoS technique for WLM solutions. However, they used a higher concentrated 100 mM CPyCl/NaSal solution with $0.52 \leq R \leq 0.9$ as well as a 3 wt% OTAB/NaOA solution (corresponding to approximately 120 mM). These strongly viscoelastic solutions showed transitions from linear to shorter linear micelles and from linear to branched micelles with increasing R , respectively. The authors argued that in CaBER experiments, WLM are subjected to significant step-strain perturbations at the onset of the experiment, thus inducing flow-induced micellar chain scission and resulting in shorter filament lifetimes in CaBER experiments, compared to DoS measurements.

Here, the dilute surfactant solution shown in Fig. 4.8 consists of small, rodlike micelles and does not show a shear-thinning or viscoelastic behavior, in contrast to the systems investigated by Omidvar *et al.* [98]. We find no influence of filament creation method (CaBER and DoS) on filament lifetime t_{fil} within experimental error. As the filament lengths increases, e.g. $h_f > 5$ cm, the filaments start to vibrate due to a draft

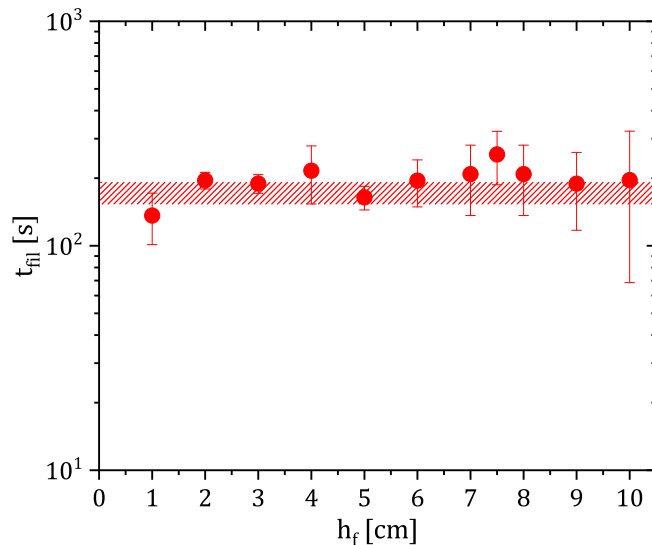


Figure 4.8: Filament lifetime t_{fil} of a 10 mM CTAB/NaSal, $R = 0.5$ solution as a function of final displacement h_f between needle and glass plate in dripping-onto-substrate experiments. The hatched red area represents the filament lifetime obtained from classic CaBER experiments.

of air and t_{fil} varies stronger from measurement to measurement, yet we find stable and long-living filaments as long as conditions are such that cylindrical filaments can be formed.

4.3 Conclusions

Dilute surfactant solutions show a unique filament thinning behavior in uniaxial extension. Although these low viscous solutions have a zero shear viscosity close to water (i.e. $\eta_0 \approx 3$ mPa s for 10 mM CTAB/NaSal, $R = 0.5$) and do not show any elastic response in SAOS measurements, they exhibit filament lifetimes on the order of several minutes, as probed by CaBER. This breakup process is neither influenced by variation of the viscosity of the surrounding phase nor by varying the interfacial tension between the surfactant solution and surrounding phase by one order of magnitude. This is an unusual result since surface tension is the dominating driving mechanism in capillary breakup processes and should therefore strongly influence the filament lifetime. Furthermore, surprisingly long filaments with a length greater than 10 cm can be created with these dilute surfactant solutions.

Similar long filament lifetimes in CaBER experiments were previously reported for surfactant solutions at low concentrations. To explain the long t_{fil} , a structure formation in elongational flow fields, termed elongation-induced structures (EIS), was proposed analogous to SIS buildup in shear. Sachsenheimer *et al.* [5] investigated the uniaxial thinning behavior of CTAB/NaSal and CPyCl/NaSal solutions and suggested that the formation of EIS stabilizes the liquid thread during capillary thinning, thus increasing t_{fil} . Additionally, Omidvar *et al.* [6] found a similar phenomenon for very

low concentrated CTAT solutions, also exhibiting long-lasting filaments. The authors calculated extensibility parameters based on bulk rheological data from elongation and shear measurements and argued that cylindrical micelles aggregated into bigger worm-like micelles during uniaxial deformation. These long micelles could entangle, forming a viscoelastic network, resulting in a growth of extensional stresses inside the filament and hence delaying the capillary breakup. However, direct evidence of elongation-induced structure buildup in low concentrated surfactant solutions is still missing.

The generic observations reported above, motivate us to have a closer look at the unique extensional properties of this type of low viscosity fluids, exhibiting unusual filament lengths and lifetimes. In an effort to reveal the origin of the long filament lifetime and the proposed EIS formation, we visualize the flow inside horizontal surfactant threads in the following chapter.

5 Flow Inside Thinning Surfactant Filaments

In this chapter, we introduce a novel method to investigate the flow field inside horizontally stretched fluid filaments during capillary thinning, using particle image velocimetry (PIV). The stretching setup and the PIV analysis routine is tested by examining the flow inside filaments of a viscoelastic polymer solution. Subsequently, we investigate the flow inside dilute surfactant solution threads that exhibit long filament lifetimes in detail and compare the results to the flow behavior of highly concentrated surfactant solutions. Finally, we establish instability maps for four widely studied surfactant systems by carefully exploring a broad range of surfactant and salt concentration.

5.1 Experimental

5.1.1 Flow field measurements during horizontal filament thinning

In order to create horizontal filaments, a stretching device is designed similar to CaBER, as schematically shown in Fig. 5.1(a). The device consists of two circular plates that can be separated with two micrometers (M-622, Physik Instrumente (PI) GmbH & Co. KG). This design allows to adjust an initial displacement h_i as well as a final displacement h_f in the range of $0 \leq h \leq 15$ mm between the plates, accurately to $10 \mu\text{m}$. However, if h_i or h_f are chosen too large, bending and sagging of the fluid bridge between the plates can arise and can influence capillary thinning. Therefore, we limit the final displacement to $h_f \leq 4$ mm and confirm that filament thinning is not influenced by stretching the fluid horizontally, by determining the diameter decay over time from classic vertical CaBER measurements as well as from horizontal tilted CaBER experiments [182]. Stretching surfactant filaments with both methods results in the same thinning process and similar filament lifetimes t_{fil} are obtained. The stretching device shown in Fig. 5.1(b) can be equipped with plates of diameter $1 \leq D_0 \leq 8$ mm. One plate is fixed, while the other plate is separated from an initial length h_i to a final length h_f within a time t_s . If not mentioned otherwise, we use $D_0 = 4$ mm, $h_i = 1$ mm, $h_f = 4$ mm and $t_s = 0.5$ s as stretching parameters. The customized stretching device is used to create horizontal filaments between the circular plates, as indicated by the red thread in Fig. 5.1(b).

We perform quantitative measurements of the flow field inside thinning fluid filaments by employing particle image velocimetry. In PIV experiments, the displacement

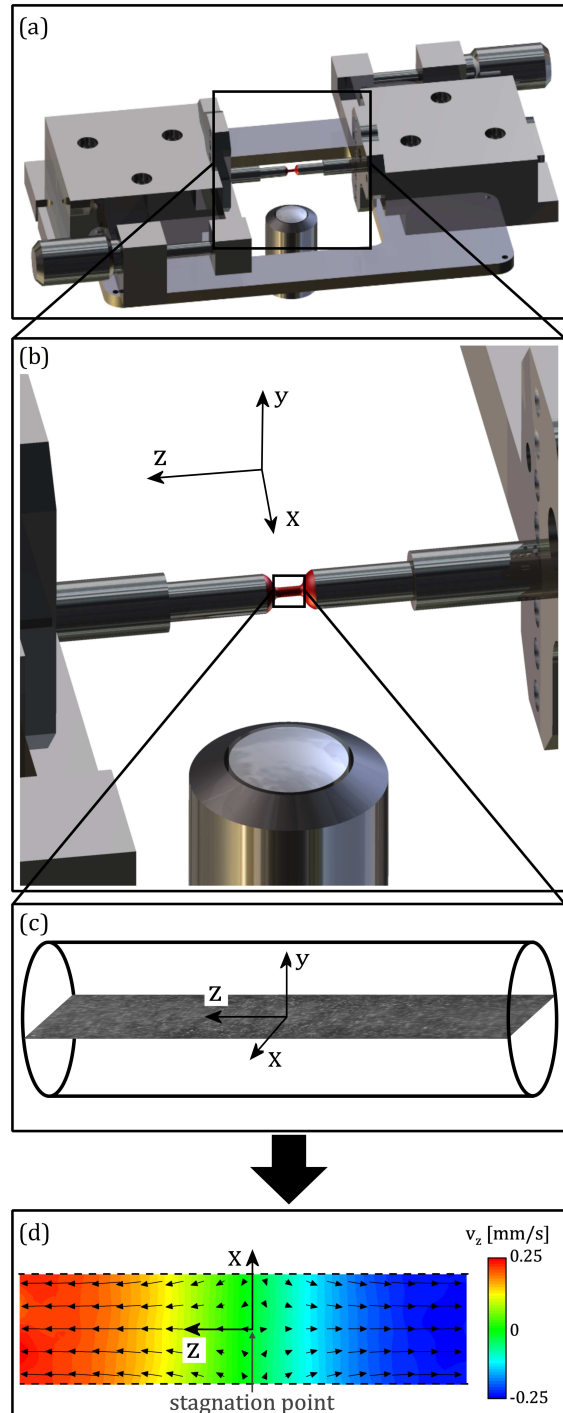


Figure 5.1: Schematic illustration of (a) the complete and (b) of the middle part of the stretching device. The sample (red) is placed between two circular plates that reached their final position h_f and the lens is focused in the center between both plates. (c) Image of a thinning PEO filament seeded with fluorescent particles in the midplane of the filament. Note that the field of view is much smaller than h_f . (d) Color plot of the axial velocity component v_z with superimposed velocity vectors in the $x - z$ plane. The dashed black lines indicate the filament borders. *Reproduced with permission from Springer Nature [1].*

of added particles in the sample is determined. Generally, the two-dimensional velocity field is calculated by analyzing the cross-correlation of two consecutive frames, subdividing the PIV recording into certain interrogation areas. For a thorough description of PIV techniques see Raffel *et al.* [183].

In our setup, samples are seeded with 0.01 wt% of mono-disperse fluorescent polystyrene microspheres (Banglabs Inc.) of diameter $d_p = 0.96 \mu\text{m}$ with excitation and emission wavelengths of 480 nm and 520 nm, respectively. The horizontal stretching device is mounted on an inverted fluorescence microscope (AxioObserver D, Carl Zeiss AG) equipped with a sCMOS Zyla X camera (Andor Technology, 2048×2048 pixel, up to 50 fps) and a long working distance lens (Nikon LU-Plan, $20\times$, $NA = 0.4$). A constant LED light source (Colibri, $\lambda_{\text{LED}} = 470 \text{ nm}$, Carl Zeiss AG) is used for volume illumination of the cylindrical filament. The measurement depth of two-dimensional PIV measurements δz_m can be defined as the distance over which particles are located with sufficient intensity and thus contribute to the correlation function [183]. It is calculated according to Meinhart *et al.* [184]:

$$\delta z_m = \frac{3n\lambda_0}{NA^2} + \frac{2.16d_p}{\tan \theta} + d_p, \quad (5.1)$$

where n is the refractive index of the fluid between the device and the objective lens (i.e. air), λ_0 is the wavelength of light in vacuum imaged by the optical system, and NA is the numerical aperture of the objective lens. In the second and third term, d_p is the particle diameter and $\tan \theta \simeq \sin \theta = NA/n$, valid for small light collection angles. With the configuration used here, the PIV measurement depth over which particles contribute to the determination of the flow field is $\delta z_m \approx 15 \mu\text{m}$.

After the plate reaches h_f , images are recorded throughout the whole thinning process, making a longitudinal cut through the midplane of the center part of the slender filament, as shown in Fig. 5.1(c). During the early thinning process, the filament diameter is $100 \leq D \leq 300 \mu\text{m}$, depending on the surfactant sample. This accounts for $0.05 \leq \delta z_m/D \leq 0.15$. During the late thinning stages, the amount of tracer particles in the filament is not sufficient for feasible PIV analysis. Hence, we limit our measurements to times when $D > 50 \mu\text{m}$ ($\delta z_m/D \approx 0.3$). Particle images are captured and analyzed in pairs, where the time delay between two images in each pair is chosen such that particle displacement is around 4 pixels. Note that the field of view ($\approx 350 \times 350 \mu\text{m}$) is much smaller than the filament length, i.e. $h_f - h_i = 3 \text{ mm}$. Thus, only flow in the center of the fluid thread is examined. We use an open source PIV software [185, 186] for quantitative analysis of the flow field. Velocity vectors are obtained in interrogation areas of 32×32 pixels in x and z direction. Here, the velocity field inside the horizontal filaments is shown as a spatial color plot representation of the axial velocity component v_z with superimposed velocity vectors in the $x - z$ plane, as schematically shown in Fig. 5.1(d).

5.1.2 Homogeneous uniaxial elongation of viscoelastic fluids

We test the PIV setup for horizontal filament stretching by investigating the flow inside a thinning viscoelastic poly(ethylene oxide) (PEO) filament (2 wt%, $M_w = 10^6 \text{ g/mol}$, Sigma Aldrich). Figure 5.2(a) displays the diameter over time during the thinning of

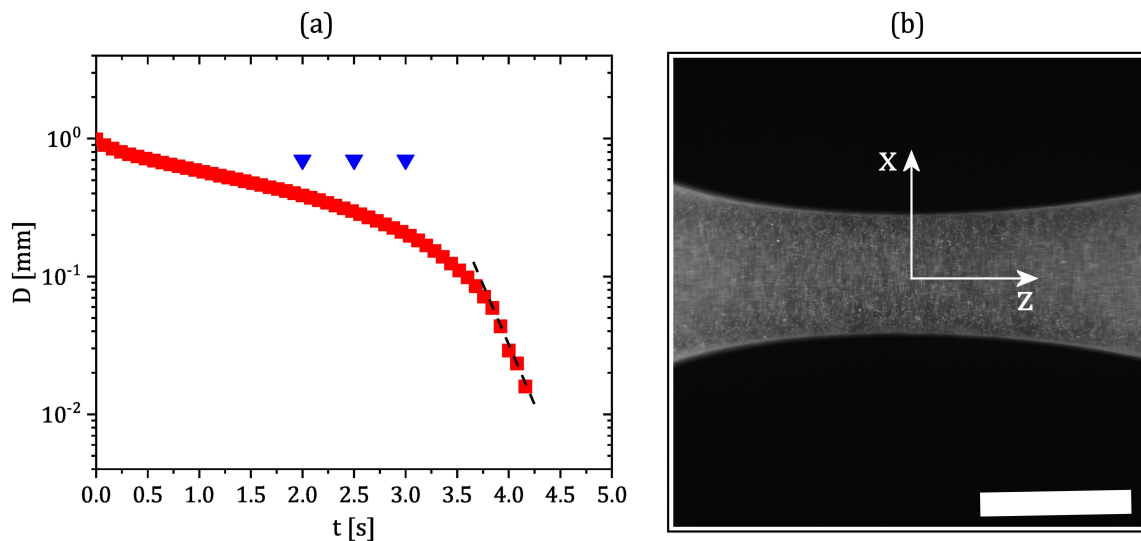


Figure 5.2: (a) Diameter as a function of time for a PEO filament (2 wt%, $M_w = 10^6$ g/mol). Dashed line represents an exponential fit of the diameter over time curve in the last part on the thinning process. Blue arrow heads indicate the times at which PIV analysis is performed in Fig. 5.3. (b) Raw PIV image of the PEO filament in the $x - z$ plane at $t = 2$ s, seeded with 0.01 wt% of mono-disperse fluorescent polystyrene microspheres ($d_p = 0.96 \mu\text{m}$). The white scale bar represents a length of 0.5 mm.

the horizontally stretched PEO filament. Here, the filament lifetime is slightly longer compared to CaBER experiments on similar PEO solutions [187], since a smaller final displacement h_f is used in our study. PIV analysis of the flow field is performed at three times during thinning, as indicated by the blue arrowheads, and is discussed in detail in the following paragraphs. In the late thinning regime, the filament thins with an exponentially decreasing diameter, indicated by the dashed black line. A representative raw image of the seeded filament at $t = 2$ s is shown in Fig. 5.2(b). Such images are analyzed in pairs at the indicated times in Fig. 5.2(a) to obtain the velocity components v_x and v_z in x and z direction, respectively.

Figure 5.3 shows the velocity field at three times during the thinning of the PEO filament, indicated in Fig. 5.2(a). We analyze the flow inside the longitudinal $x - z$ midplane of the filament and in the center between the plates (schematically shown in Fig. 5.1). In Fig. 5.3, we present the velocity component v_z in axial direction z as spatial color plot representation with superimposed velocity vectors to guide the eye. The flow field during uniaxial elongation is homogeneous, with flow in both negative and positive axial direction z , axisymmetric to the centrally located stagnation point, as shown in Fig. 5.3. This homogeneous flow persists throughout the whole thinning process and is expected for thinning viscoelastic filaments in uniaxial extension in accordance with earlier work on similar viscoelastic fluids [188].

We extract the axial velocity component v_z and the velocity component v_x in the x direction from Fig. 5.3 at $z \approx -0.3$ mm and plot both quantities over the normalized filament diameter $x/D(t)$ in Fig. 5.4(a). First, we again see that the velocity profiles of

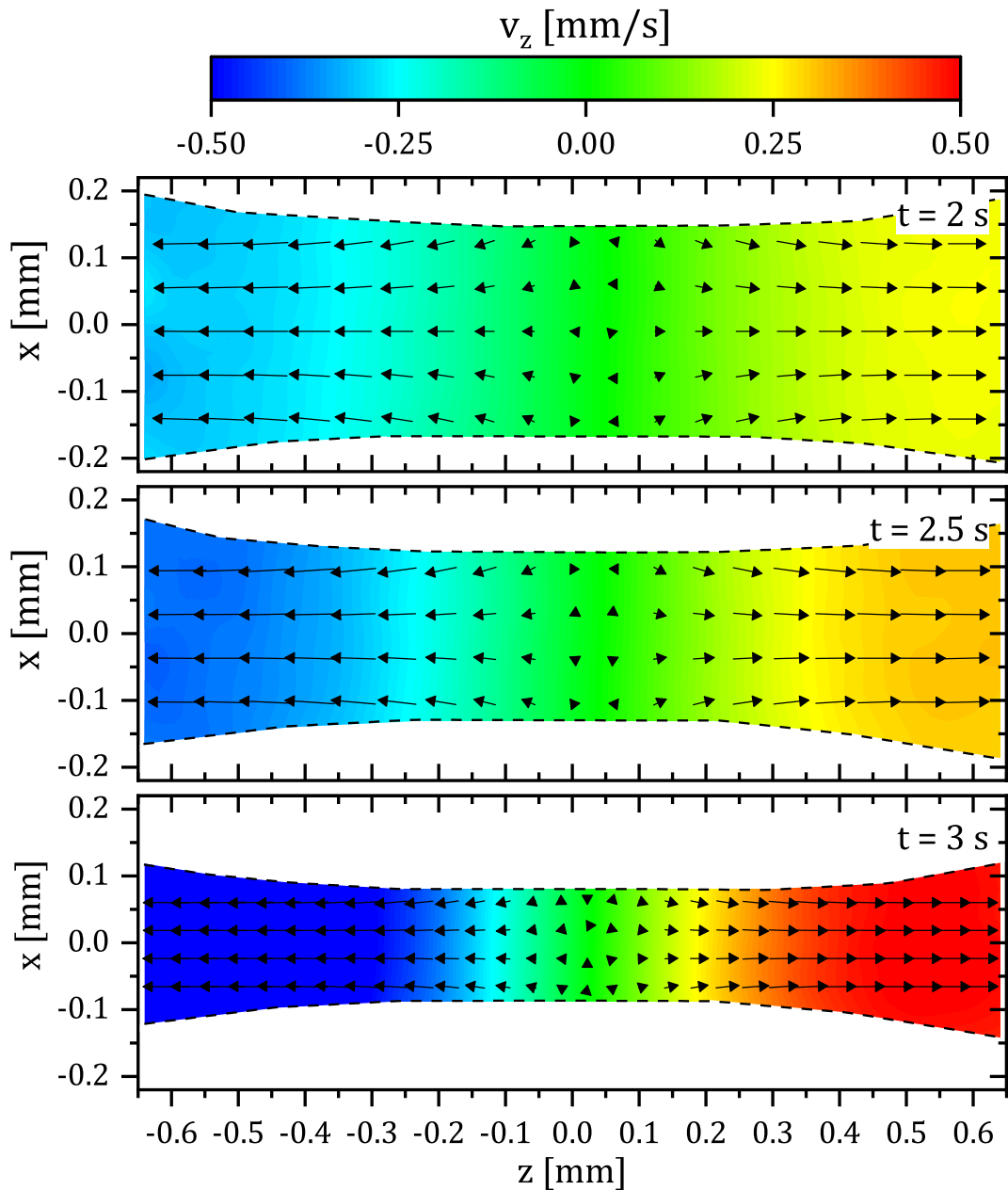


Figure 5.3: Velocity component v_z in axial direction inside a PEO filament (2 wt%, $M_w = 10^6$ g/mol) filament during thinning, as indicated by the time stamps in the corresponding panels. The initial displacement, final displacement, and strike time are $h_i = 1$ mm, $h_f = 4$ mm, and $t_s = 0.5$ s, respectively. Dashed black lines represent the filament boundaries in the measured plane.

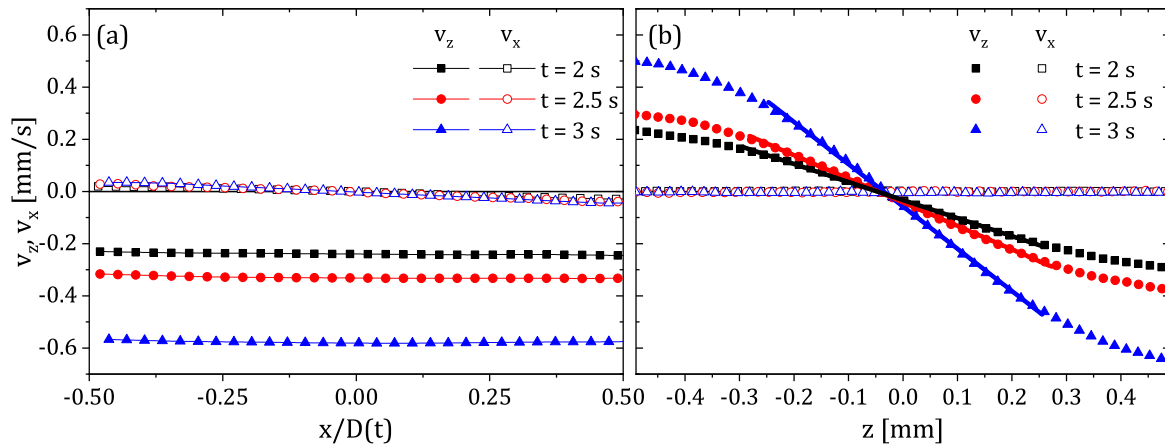


Figure 5.4: (a) Flow profiles of the axial velocity component v_z (closed symbols) and velocity component v_x in x direction (open symbols) over the normalized filament diameter $x/D(t)$ for the PEO solution, shown in Fig. 5.3. Data is extracted from Fig. 5.3 at $z \approx -0.3$ mm. (b) v_z and v_x over the axial coordinate z , extracted from Fig. 5.3 at $x = 0$ mm.

v_z show a homogeneous, plug-like flow that is sustained throughout the whole thinning process until the filament breaks. Second, we find that v_x (open symbols) is always more than one order of magnitude smaller than v_z (closed symbols), in agreement with Gier and Wagner [188]. Hence, v_x will not be considered in the result section regarding the flow behavior inside surfactant filaments. Gier and Wagner [188] investigated the flow profile in a thinning capillary bridge of a 0.2 wt% PEO solution ($M_w = 4 \times 10^6$ g/mol), dissolved in a 60/40 wt% glycerol-water solution. They used particles with a diameter of $d_p = 3 \mu\text{m}$ and employed a PIV technique to visualize the flow in filaments ranging from $150 \geq D(t) \geq 30 \mu\text{m}$. During the initial formation of the cylindrical filament (i.e. $t/t_{\text{fil}} \lesssim 0.24$), they found flow only in the outer parts of the filament. We do not observe this non-uniform flow profile for the investigated PEO solution here. Gier and Wagner [188] further reported that when the cylindrical filament is formed and throughout the subsequent thinning, the flow field is homogeneous and purely extensional, similar to our results. However, in contrast to the PEO solution investigated by Gier and Wagner [188], the PEO filament shown in Fig. 5.3 does not form a perfect cylindrical shape between the plates (see Fig. 5.2(b)) and the temporal evolution of the thinning diameter in Fig. 5.2(a) can be fitted with an exponential model merely in the last thinning regime [103].

Furthermore, we show the velocity components v_z and v_x , extracted at the filament centerline $x = 0$ mm from Fig. 5.3, and plot both quantities over z in Fig. 5.4(b). Again, we find that v_x (open symbols) is more than one order of magnitude smaller than v_z (closed symbols), i.e. $v_x \approx 0$. Furthermore, the velocity gradient that defines the elongation rate in the filament $\dot{\epsilon} = dv_z(z)/dz|_{x=0}$ can be fitted with a linear model in the cylindrical center part of the filament, indicated by the full lines in Fig. 5.4(b) for $-0.25 \leq z \leq 0.25$ mm. Thus the fluid deforms with a constant elongation rate $\dot{\epsilon}$ in the cylindrical filament middle. However, the elongation rate is not constant over time and increases as the filament thins, since the diameter does not decrease exponentially in the regime investigated with PIV (see Fig. 5.2(a)). Hence, $v_z(x)$ as well as the slope

$dv_z(z)/dz|_{x=0}$ increase over time, as shown in Fig. 5.4(a) and (b), respectively.

5.2 Results and discussion

After we confirm our novel method by examining the flow inside thinning threads of a well-characterized viscoelastic polymer solution, we now apply our stretching and PIV technique to surfactant filaments. First, dilute solutions are probed that exhibit unusually long filament lifetimes. Second, higher concentrated surfactant solutions are probed in a broad range of surfactant concentration c_{surf} as well as salt/surfactant ratio R , in an effort to map the flow behavior inside surfactant filaments.

5.2.1 Heterogeneous flow of dilute solutions

Figure 5.5 shows the velocity component v_z in axial filament direction z for a dilute, shear-thickening 10 mM CTAB/NaSal, $R = 0.5$ solution. We focus on this solution as a representative example of the flow behavior of dilute surfactant solutions. The flow inside the longitudinal $x - z$ midplane of the circular filament and in the center between the plates is analyzed and v_z is presented as spatial color plot representation with superimposed velocity vectors to guide the eye. Note, that the color bar in Fig. 5.5 ranges from negative to positive values of v_z , i.e. flow in negative and positive axial direction.

For the dilute 10 mM CTAB/NaSal, $R = 0.5$ solution shown in Fig. 5.5, an unexpected flow behavior emerges. We find flow in positive and negative axial direction z across the filament diameter, indicated by the red/yellow and blue colors, respectively. During filament thinning, two bands form inside the filament midplane, transporting fluid in opposing axial directions. This non-homogeneous pattern is visible during the whole thinning process.

To show the development of the flow pattern over time, the velocity component v_z is extracted from Fig. 5.5 at $z = 0$ mm and plotted over the normalized diameter $x/D(t)$ in Fig. 5.6, where different curves correspond to the three times during the thinning process shown in Fig. 5.5. For the 10 mM CTAB/NaSal, $R = 0.5$ solution, we again see that two bands with flow in both axial directions are present at $t/t_{\text{fil}} = 1/4$. This heterogeneous flow pattern persists throughout the whole thinning process, but the shape of the flow profile and the magnitude of v_z change over time. The band with flow in positive axial direction broadens, while the width of the other band seems to decrease until only flow in one direction leads to filament breakup. The non-uniform velocity pattern of $v_z(x)$ results in a velocity gradient, hence a shear rate distribution $\dot{\gamma}(x) = dv_z(x)/dx$ across the filament diameter. For the 10 mM CTAB/NaSal, $R = 0.5$ solution shown in Fig. 5.6, we find regions of localized high shear rate $2 \leq \dot{\gamma}(x) \leq 5 \text{ s}^{-1}$ between different bands. These shear rates are in the hysteretic region of the flow curve (see Fig. 3.3).

Performing multiple experiments with the dilute surfactant and salt solution always yields heterogeneous flow patterns, yet the number of bands and the magnitude of v_z in the bands seem to change arbitrarily from measurement to measurement. Furthermore, this heterogeneous flow occurs irrespective of stretching ratio (i.e. D_0 , h_i and h_f) and

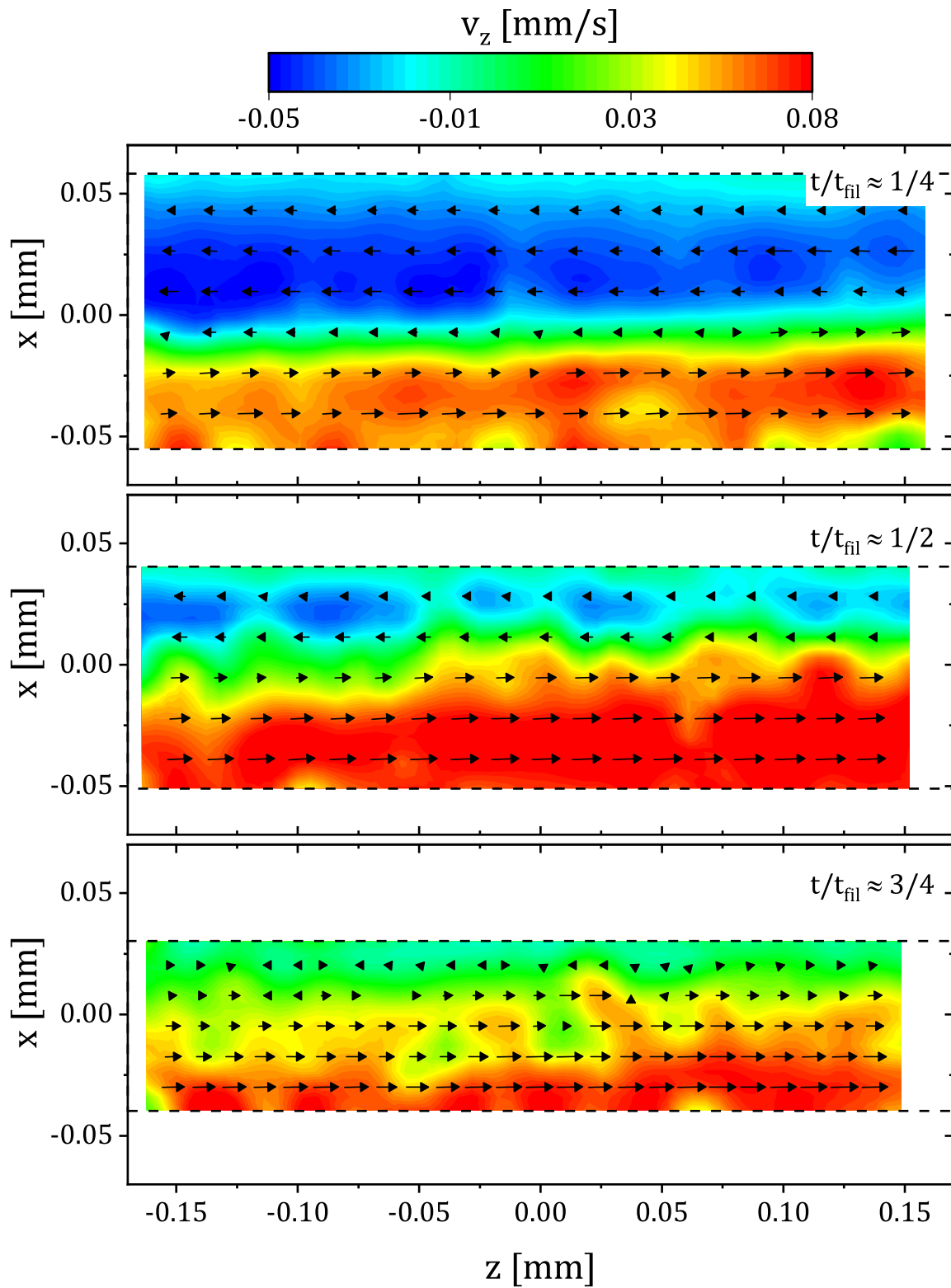


Figure 5.5: Velocity component v_z in axial direction inside a 10 mM CTAB/NaSal, $R = 0.5$ filament for three times during thinning, as indicated by the time stamps in the corresponding panels. The initial displacement, final displacement, and the strike time are $h_i = 1$ mm, $h_f = 4$ mm, and $t_s = 0.5$ s, respectively. Dashed black lines represent the filament boundaries in the measured plane. *Top panel reproduced with permission from Springer Nature [1].*

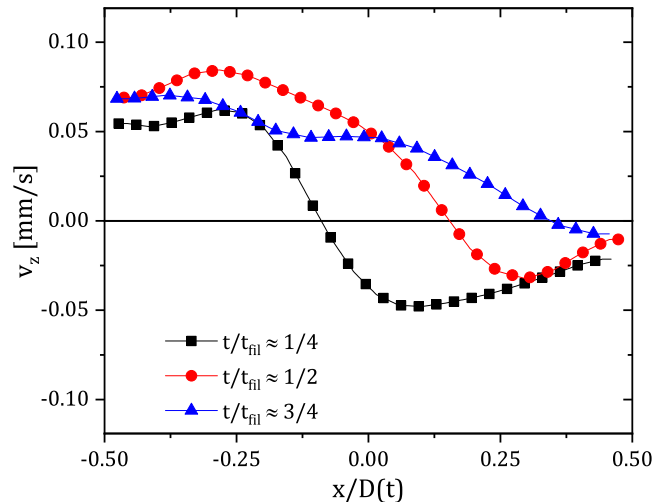


Figure 5.6: Flow profiles of the axial velocity component v_z over the normalized filament diameter $x/D(t)$ for a 10 mM CTAB/NaSal, $R = 0.5$ solution. Data is extracted from Fig. 5.5 at $z = 0$ mm for three different times. During this time, the filament diameter decreases from $D \approx 115 \mu\text{m}$ to $70 \mu\text{m}$. Dashed black lines represent the filament boundaries. *Reproduced with permission from Springer Nature [1].*

strike time (t_s), as long as conditions are such that cylindrical filaments form. This is the first observation of such a heterogeneous banding phenomenon during the thinning of a fluid in uniaxial elongational deformation.

Furthermore, we find that for low concentrated samples, the flow in the whole filament cross-section is heterogeneous, and not only in the middle of the cylindrical filament as shown in Fig. 5.5. We use a long travel range objective scanner (P-a 725.4CD, Physik Instrumente (PI) GmbH & Co. KG) to capture the three-dimensional (3D) flow inside the lower half of the circular filament. Image pairs in the $x - z$ plane are recorded in ten slices, with spacing δ_s in depth y of the filament matching the measurement depth of the PIV setup $\delta_s \approx \delta z_m$. The total number of image pairs is recorded over a time of roughly 1 s that is much smaller than the filament lifetime $t_{\text{fil}} \approx 100$ s, hence thinning in radial direction and spatial shifting of the velocity bands can be neglected. PIV analysis is performed in each slice and v_z is extracted at the same axial position. Figure 5.7 shows v_z in the lower half of a 10 mM CTAB/NaSal, $R = 0.5$ filament. From this 3D representation, it is clear that the heterogeneous flow exists in the whole cross-section without any rotational symmetry. At one fixed x position, e.g. $x = -0.05$ mm, flow direction changes along the y -axis, as seen in the projection at the bottom of Fig. 5.7.

In our experiments shown in Fig. 5.5 and Fig. 5.7, the field of view is much smaller than the filament length (i.e. $h_f - h_i = 3$ mm), thus the heterogeneous flow is only visible in the central part of the filament. In Fig. 5.8, we decrease the final height to $h_f \approx 1.5$ mm and use a $10\times$ lens to elucidate the flow field in the whole filament. Here, we track individual tracer particles that are in the right reservoir at $t = 0$ s over a 20 s time interval. We use a custom particle tracking routine, incorporated into the software Image Processing System (Visiometrics iPS) and a self-written MATLAB pro-

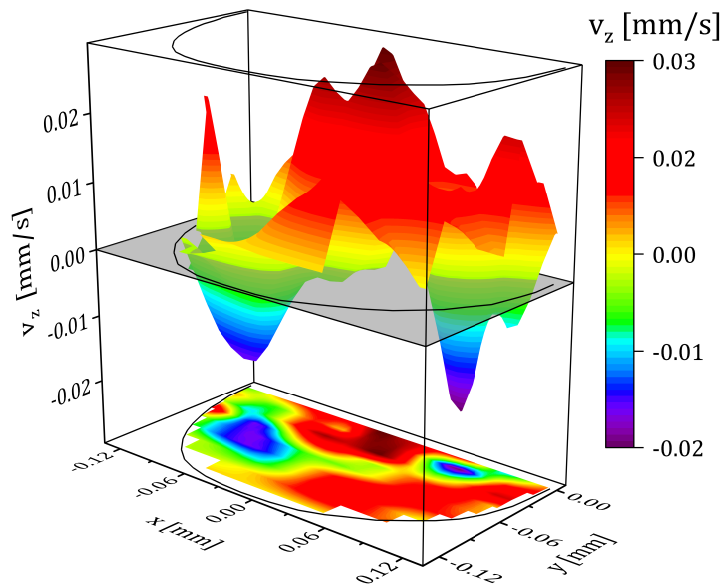


Figure 5.7: Three-dimensional (3D) representation of the axial velocity component v_z in the lower half of a circular 10 mM CTAB/NaSal, $R = 0.5$ filament cross-section. The graph is rotated vertically by 90° and a projection of v_z in the $x - y$ plane is inserted at the bottom of the graph. The grey, semitransparent area indicates the $v_z = 0$ surface. *Reproduced with permission from Springer Nature [1].*

gram [189] based on the widely used Crocker and Grier tracking algorithm [190]. Our results in Fig. 5.8 show that particles travel from one reservoir across the filament into the opposite reservoir. This means that the heterogeneous flow exists across the whole filament length and leads to an additional flow from the reservoirs into the filament besides the expected surface tension driven flow from the filament into the reservoirs at both ends. A circulating flow merely inside the filament is not observed. Trajectories that seem to start inside the filament arise from tracers entering the focal plane during data acquisition. We find this heterogeneous flow behavior for the CTAB/NaSal and CPyCl/NaSal solutions investigated by Sachsenheimer *et al.* [5] and the CTAT samples probed by Omidvart *et al.* [6]. Both originally attributed the observation of long filament lifetimes to the formation of elongation-induced structures. Here we find that the immediate reason for the long filament lifetime is the additional flow from the reservoir into the filament of dilute surfactant solutions. The origin for this non-homogeneous flow with the reported flow bands is a flow instability triggered by the extensional deformation of the filament and we hypothesize that the extreme stretchability of the fluid filaments in the other experiments reported above (see Fig. 4.6) is also due to such an elongation-induced banding phenomenon.

5.2.2 Uniform extension of high concentrated solutions

Next, we employ the stretching and PIV method to viscoelastic, higher concentrated surfactant solutions and focus on a 30 mM CTAB/NaSal, $R = 7.67$ solution, as a

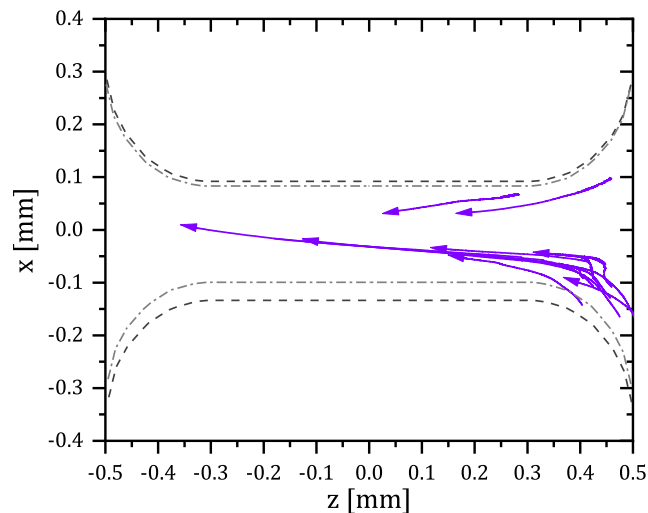


Figure 5.8: Trajectories of individual tracer particles during thinning over 20 s of a 10 mM CTAB/NaSal, $R = 0.5$ filament. Arrowheads indicate movement directions of the tracers. Dark grey dashed line and light grey dashed-dotted line represent the filament boundaries at $t = 0$ s and $t = 20$ s, respectively. A $10\times$ lens and a final displacement of $h_f \approx 1.5$ mm is used for this experiment. *Reproduced with permission from Springer Nature [1].*

representative sample. In contrast to the flow behavior inside the dilute surfactant solution reported above, the 30 mM CTAB/NaSal, $R = 7.67$ solution shows uniform flow inside the filament, as seen in Fig. 5.9. Thus, increasing the amount of salt and surfactant in the system results in a homogeneous flow across the filament cross-section, as expected for viscoelastic thinning filaments and similar to the results reported by Gier and Wagner [188] for polymer solutions. However, the stagnation point is not in the center between the reservoirs but shifted towards negative z direction. In contrast to the low concentrated, shear-thickening solutions (with $\eta_0 = 3$ mPa s), the 30 mM CTAB/NaSal, $R = 7.67$ solution exhibits a Newtonian plateau with a low-shear viscosity of $\eta_0 \approx 18$ Pa s, followed by a shear-thinning regime for $\dot{\gamma} \gtrsim 0.1$ s $^{-1}$ (see Fig. 3.2(a)).

The velocity component v_z is extracted from Fig. 5.9 at $z = 0$ mm and plotted over the normalized diameter $x/D(t)$ in Fig. 5.10(a). For the higher concentrated surfactant/salt sample, velocity profiles show a homogeneous, plug-like flow that remains present throughout the whole thinning process until the filament breaks. Here, the velocity gradient $dv_z(x)/dx$ across the filament diameter is neglectable within experimental error, in accordance with earlier work regarding the flow inside viscoelastic polymer solutions [188].

Besides the heterogeneous and homogeneous flow regimes, we find a transition behavior, where sample composition leads to flow in only one axial direction, yet the velocity profile v_z is non-uniform, as shown in Fig. 5.10(b). This flow profile changes arbitrarily from measurement to measurement, while performing multiple experiments.

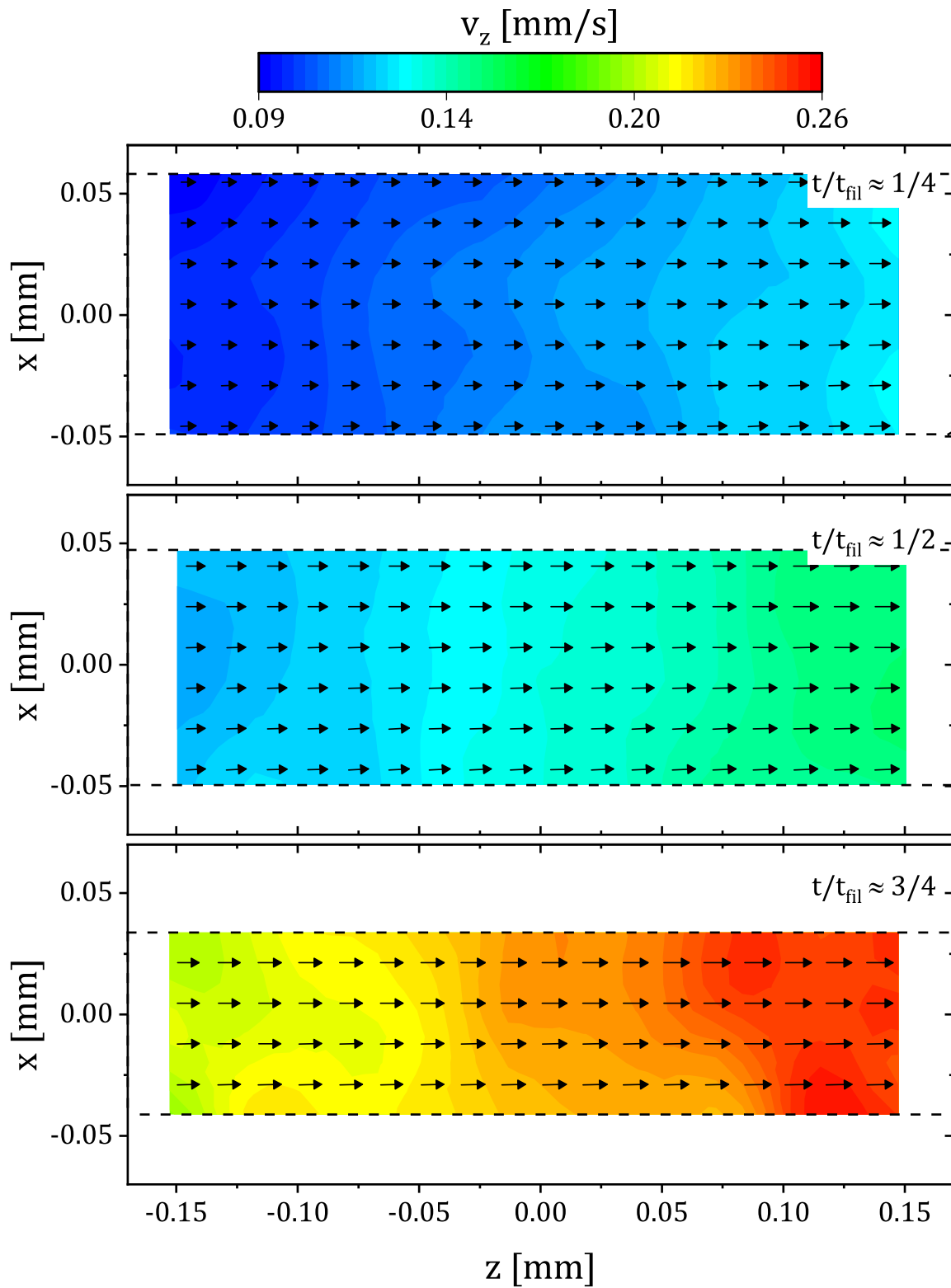


Figure 5.9: Velocity component v_z in axial direction inside a 30 mM CTAB/NaSal, $R = 7.67$ surfactant filament for three times during thinning, as indicated by the time stamps in the corresponding panels. The initial displacement, final displacement, and the strike time are $h_i = 1$ mm, $h_f = 4$ mm, and $t_s = 0.5$ s, respectively. Dashed black lines represent the filament boundaries in the measured plane.

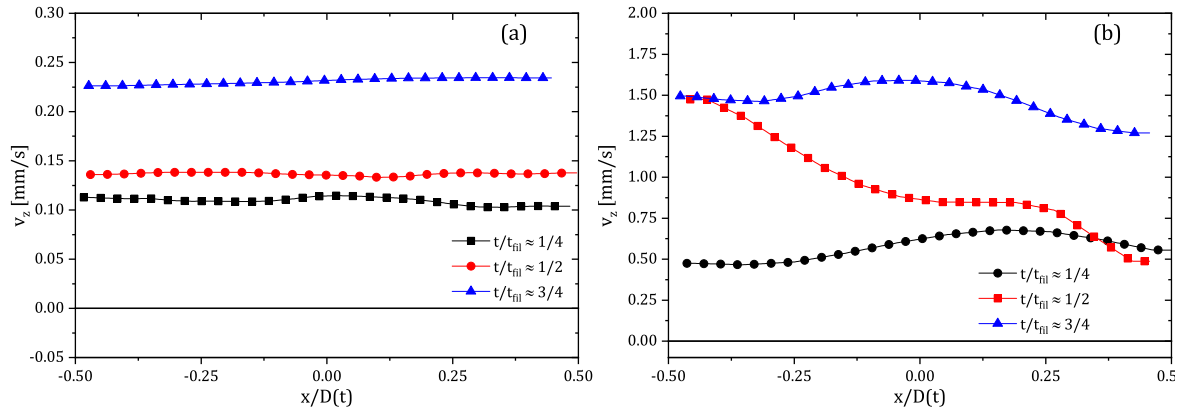


Figure 5.10: Flow profiles of the axial velocity component v_z over the normalized filament diameter for (a) a 30 mM CTAB/NaSal $R = 7.67$ solution and (b) a 20 mM CTAB/NaSal, $R = 3$ for three different times during filament thinning. For (a) data is extracted from Fig. 5.9 at $z = 0$ mm for three different times. During this time, the filament diameter decreases from $D \approx 110 \mu\text{m}$ to $75 \mu\text{m}$ in (a) and from $D \approx 100 \mu\text{m}$ to $60 \mu\text{m}$ in (b). Dashed black lines represent the filament boundaries. (a) *Reproduced with permission from Springer Nature* [1].

5.2.3 Flow behavior phase diagrams

We summarize our results regarding the flow behavior inside thinning surfactant filament in Fig. 5.11, by covering a broad range of surfactant concentrations c_{surf} as well as the salt/surfactant ratio R for the four investigated surfactant/salt systems (a) CTAB/NaSal, (b) CPyCl/NaSal, (c) CTAC/NaSal and (d) CTAT/NaTos. All systems show similar features in the investigated concentration regimes. If the surfactant concentration or the amount of salt is too low, no filaments form during uniaxial deformation. When filaments can be created, we find three types of different flow behavior. For low surfactant concentrations, the flow is heterogeneous with flow in both axial directions. This heterogeneous flow leads to the additional flow from the reservoirs into the filament, thus increasing the filament lifetime. For high surfactant and salt concentrations, a homogeneous flow in one axial direction away from the stagnation point in the filament center emerges. Between the heterogeneous and homogeneous areas, a transition regime appears. Here, we find either homogeneous or heterogeneous flow while performing multiple experiments. Also in this transition regime, some samples show flow in only one axial direction, however the velocity profile of v_z is non-uniform (see Fig. 5.10(b)) similar to the results reported by Gier and Wagner [188] during the early thinning stages of PEO threads. The extent of the heterogeneous flow regimes varies between the different surfactant systems, and is greatest for CTAB/NaSal (red area in Fig. 5.11(a)). For CTAT/NaTos, filaments can be created even without the addition of salt at $R = 0$ and we therefore plot the x axis linearly. This can be explained as follows. For the samples in Fig. 5.11(a-c), the halogen counterions Br^- and Cl^- dissociate in water and the added salt NaSal promotes anisotropic micellar growth, by penetrating the polar micellar shell that is mostly composed by surfactant headgroups [191]. In the case of CTAT, the surfactant molecule consists of the cationic surfactant

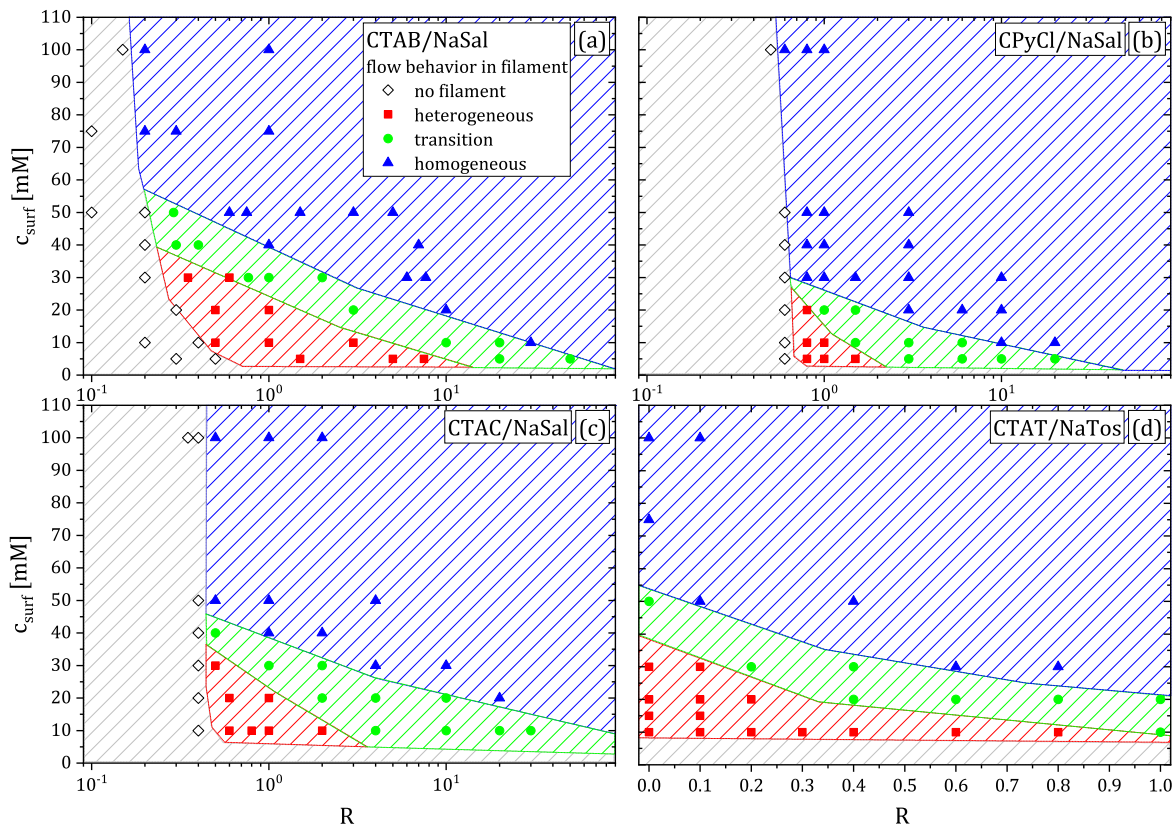


Figure 5.11: Flow behavior phase diagrams of all investigated surfactant/salt systems; (a) CTAB/NaSal, (b) CPyCl/NaSal, (c) CTAC/NaSal, (d) CTAT/NaTos. Hatched areas are to guide the eye. *Reproduced with permission from Springer Nature [1].*

chain and the anionic molecule p-toluenesulfonate. If the pure surfactant is dissolved in water, the dissociation of p-toluenesulfonate is sufficient to promote the formation of elongated micelles without the addition of further salt. In this case, the instability occurs even without additional salt for $c_{surf} < 40$ mM.

Such long filament lifetimes for low concentrated surfactant solutions were reported previously and were attributed to the formation of elongation-induced structures [5, 6]. However, here we find that the immediate reason for the long filament lifetime is the additional flow from the reservoir into the filament of dilute surfactant solutions. Sachsenheimer *et al.* [5] proposed a map for the occurrence of elongation-induced structure formation in CTAB/NaSal solutions with surfactant concentrations $0 \leq c_{surf} \leq 30$ mM and $0.2 \leq R \leq 1.6$. The regime for which they proposed the formation of EIS, based on huge filament lifetime ratios, matches the heterogeneous flow regime shown in Fig. 5.11(a) based on our PIV data. Furthermore, the CTAT solutions with $15 \leq c_{surf} \leq 25$ mM investigated by Omidvar *et al.* [6], also show heterogeneous flow (Fig. 5.11(d)) that was attributed to EIS formation without further evidence. For the particular sample 30 mM CTAB/NaSal, $R = 7.67$, EIS formation was confirmed by flow-induced onset of turbidity in planar squeeze flow and planar elongation [106, 107, 111]. However, this highly viscoelastic sample shows homogeneous flow behavior in our PIV experiments in uniaxial extension. Obviously, the emergence of a flow instability during extensional

deformation and the flow-induced formation of structures such as micellar growth and aggregation are not necessarily related.

5.3 Conclusions

We have established an experimental method and protocol to examine the flow field inside horizontally stretched thinning liquid filaments, employing particle image velocimetry. The setup is tested by investigation of the flow inside thinning polymer threads. Here, we find a homogeneous, purely extensional deformation with a centrally located stagnation point, as expected for viscoelastic solutions. A similar flow field is found for highly concentrated surfactant solutions, yet the position of the stagnation point might not be in the filament center between the plates but shifted towards one side of the filament.

In contrast, we discover an unexpected flow inside thinning threads of dilute surfactant solutions. Here, we find a heterogeneously banded flow, including regions with opposite flow directions inside the liquid thread. Tracing the motion of individual tracer particles, we show that this phenomenon leads to an additional flow from the reservoirs at the filaments ends back into the filament, besides the expected surface tension driven flow from the filament into the reservoirs. This intriguing effect also results in the formation of remarkably long filaments (> 10 cm), as shown in Fig. 4.6, and to filament lifetimes of several minutes, discussed in chapter 4.2.

Sachsenheimer *et al.* [5] investigated the uniaxial thinning behavior of surfactant solutions and reported long-lasting filaments for systems with low surfactant and low salt concentration. They attributed the long filament lifetime to the formation of EIS that stabilize the liquid thread during capillary thinning. Additionally, Omidvar *et al.* [6] found a similar phenomenon for another very low concentrated surfactant system, also exhibiting long-lasting filaments. The authors calculated extensibility parameters based on bulk rheological data from elongation and shear measurements and argued that cylindrical micelles aggregated into bigger wormlike micelles during uniaxial deformation. However, direct evidence of elongation-induced structure buildup in low concentrated surfactant solutions is still missing. Here, we find that the reason for the long filament lifetime is the additional flow from the reservoir into the filament of dilute surfactant solutions, caused by a heterogeneous banded flow inside the filament.

Banding inside the filament is induced by extensional deformation and we have proven the existence of multiple flow bands with different velocities and even reversed flow direction. However, the corresponding microstructure still remains unclear. In shear flow, microstructural transitions and corresponding flow banding instabilities in semi-dilute surfactant solutions can arise due to flow-induced concentration fluctuations [145]. One simple tool to probe the local micelle concentration is the use of the dye Nile Red as a marker to study changes in fluorescence intensity for identifying microstructural transitions [76, 192, 193, 194]. In aqueous surfactant solutions, the hydrophobic dye Nile red preferably binds into the micellar core and surface. While in pure water, Nile Red does not fluoresce in the visible spectrum, the fluorescence intensity in micellar solutions was shown to increase linearly with surfactant concentration [76]. Nile Red was recently used to study micelle-to-vesicle [192] and sphere-to-

rod-to-wormlike micelle transition [193] in aqueous surfactant solutions. Furthermore, the dye was used to study flow-induced structure formation in flows of CTAB/NaSal solutions through a microfluidic array of microposts [76] as well as to probe the formation of micellar membranes in a T-shaped microchannel [194]. Here, we try to reveal possible concentration fluctuations inside the thinning surfactant filament, by using a 10 mM CTAB/NaSal, $R = 0.5$ surfactant solution containing $1 \mu\text{M}$ fluorescent Nile Red. The addition of dye does not influence the filament lifetime. However, the fluorescence signal of the dyed filament is uniform in the whole filament and across the filament cross-section. Thus, it is not possible to detect any spacial concentration fluctuation, similar to the heterogeneously banded flow, by using Nile Red as a marker. One explanation might be that the surfactant concentration of $c_{\text{surf}} = 10 \text{ mM}$ is not sufficient in contrast to the higher concentrations used in previous studies ($c_{\text{surf}} = 50 \text{ mM}$) [76, 194].

Although we are not able to verify a microstructural transition with the above-mentioned method, we hypothesize that the observed phenomenon is caused by a flow instability in extension. If the heterogeneous flow, characterized by multiple bands at one macroscopic elongation rate, arises from a flow instability, we may find critical conditions in terms of strain rate and total strain for this transition. Sachsenheimer *et al.* [5] found that a critical total strain $\varepsilon_c \approx 1$ is required to form long-lasting filaments in filament stretching experiments, independent of elongation rate in the range of $0.1 \leq \dot{\varepsilon} \leq 1 \text{ s}^{-1}$, as probed by FiSER experiments. In our CaBER experiments, long-lasting filaments form as soon as the fluid thins after the initial step stretch. This suggests that the banding instability arises before the fluid thread reaches its slow thinning period at D_1 (see Fig. 4.2). Assuming homogeneous deformation during uniaxial thinning, the macroscopic elongation rate $\dot{\varepsilon}$ and the total Hencky strain ε can be derived from the diameter change, as

$$\dot{\varepsilon}(t) = -\frac{2}{D(t)} \frac{dD(t)}{dt} \quad (5.2)$$

and

$$\varepsilon(t) = 2 \ln \left(\frac{D_0}{D(t)} \right), \quad (5.3)$$

respectively [169, 174]. For the standard configuration used here, the diameter thins from $D_0 = 6 \text{ mm}$ to $D_1 \approx 0.3 \text{ mm}$ during the initial step stretch of the 10 mM CTAB/NaSal, $R = 0.5$ solution. During this step stretch and the subsequent filament thinning, the elongation rate $\dot{\varepsilon}$ is generally not a constant. It sets according to stretching parameters, e.g. strike time t_s , initial h_i and final h_f displacement, plate diameter D_0 , as well as viscous and elastic forces inside the fluid. Also, inertia can play an important role during the initial thinning period. Figure 5.12 shows the filament diameter as a function of time (red circles) during stretching and subsequent capillary driven thinning of a 10 mM CTAB/NaSal, $R = 0.5$ solution. At time t_s , the top plate reaches its final position h_f and the actual CaBER experiment starts. Furthermore, we calculate the local elongation rate $\dot{\varepsilon}(t)$, according to Eq. 5.2 and plot $\dot{\varepsilon}(t)$ as blue squares in Fig. 5.12.

During the initial step stretch ($t < t_s$), the filament first thins slowly before the diameter decreases rapidly when h_f is approached. During this fast thinning regime,

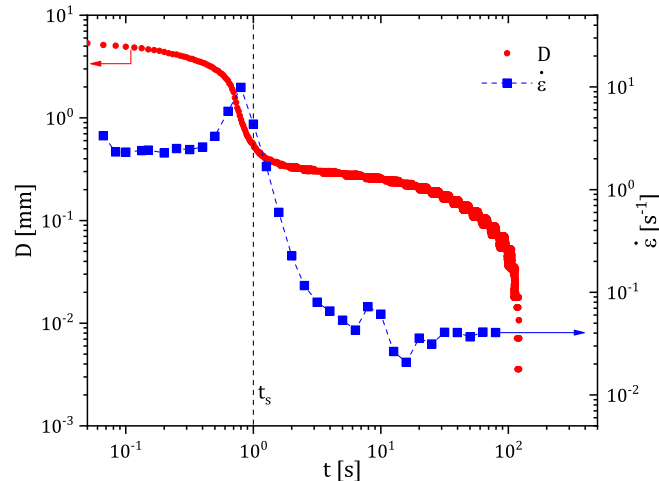


Figure 5.12: Diameter as a function of time (red circles) for a 10 mM CTAB/NaSal, $R = 0.5$ filament during step stretch and subsequent thinning, using CaBER. Stretching parameters are $D_0 = 6$ mm, $h_i = 1.5$ mm, $h_f = 6$ mm and $t_s = 1$ s. Blue squares display the local derivative of $D(t)$, hence the local elongation rate $\dot{\varepsilon}$. *Reproduced with permission from Springer Nature [1].*

the elongation rate passes through a range of $1 \leq \dot{\varepsilon} \leq 10 \text{ s}^{-1}$. Long lasting cylindrical filaments are formed as soon as the top plate reaches h_f . The instability that results in a heterogeneous flow during uniaxial extension is triggered in the initial step stretch and we take the elongation rate range $1 \leq \dot{\varepsilon}_c \leq 10 \text{ s}^{-1}$ as a critical condition for the phenomenon to arise. Furthermore, the total accumulated strain during the initial step stretch is $\varepsilon_c \approx 6$ according to Eq. 5.3, with $D_0 = 6$ mm and $D_1 = 0.3$ mm. The first thinning process is followed by a second slow capillary driven thinning period, starting at t_s and lasting until $t_{\text{fil}} \approx 150$ s. Here, the elongation rate is calculated based on the assumption of homogeneous deformation inside the filament. However, this sample shows a heterogeneous flow inside the filament, thus $\dot{\varepsilon}$ represents merely an apparent value in this regime.

The apparent $\dot{\varepsilon}$ and ε values during the initial step stretch period may give an idea for the critical parameters, necessary to induce the heterogeneous flow phenomenon. However as already noted, the elongation rate during the step stretch in CaBER experiments is not constant but sets according to stretching parameters, viscous and elastic stresses inside the tested fluid. Furthermore, the cylindrical filament shape does not allow us to employ spatially resolved optical techniques, such as birefringence imaging, to probe structural changes and orientation of micelles during elongation on a microscopic length scale. Therefore, we use a microfluidic cross-slot to generate a planar extensional flow field with a controlled elongation rate, as discussed in the following chapter. The planar flow in the deep channel enables us to make meaningful measurements of the flow-induced birefringence, which allows tracking flow-induced micellar orientation at negligible inertia and without an influence of potential solvent evaporation as well as surface tension.

6 Planar Elongational Deformation of Surfactant Solutions

In this chapter, the optimized-shape cross-slot extensional rheometer (OSCER) is briefly introduced and the characteristic flow behavior of a Newtonian fluid in this cross-slot is discussed. Further, we investigate the flow field and the flow-induced birefringence of two representative dilute surfactant solutions that show heterogeneous banding in filament thinning experiments (10 mM CTAB/NaSal, $R = 0.5$ and 30 mM CTAB/NaSal, $R = 0.35$). The results are then compared with the extensional flow behavior of two representative high concentrated samples that exhibit uniform flow during filament thinning (10 mM CTAB/NaSal, $R = 30$ and 30 mM CTAB/NaSal, $R = 7.67$).

6.1 Experimental

6.1.1 The OSCER - flow in planar elongation

Cross-slot channels play a pivotal role in the investigation and understanding of the flow behavior of complex fluids in strong extensional flow fields [195] and were used to study unraveling of fluorescently labeled DNA [196], flow-induced chain fracture of macromolecules [197] as well as instabilities in polymer solutions [198]. Devices consist of bisecting channels with opposed inlets and outlets, generating a symmetric stagnation point flow with strong elongational deformation of the fluid in the center. However, a well-defined elongational flow field is only achieved near the stagnation point in standard cross-slots. Therefore, Alves [199] proposed a numerical optimization method to design a cross-slot geometry that results in a more homogeneous extension along the outflow symmetry line. This optimized-shape cross-slot extensional rheometer (OSCER) generates an almost ideal planar elongational flow field and was used to study the flow behavior and instabilities of polymer and WLM solutions in planar elongation [160, 199, 200, 201, 202, 203, 204, 205]. A schematic representation of the geometry is shown in Fig. 6.1(a). Additionally, Fig. 6.1(b) shows the symmetric flow inside the OSCER in the $x - y$ plane ($z = 0$) with a centrally located stagnation point about which hyperbolic streamlines (superimposed dashed lines) divide symmetrically.

Here, we perform flow velocimetry experiments and measurements of flow-induced birefringence (FIB) of surfactant solutions in planar extension, using a microfluidic OSCER device. The channel is fabricated via selective laser-induced etching [206, 207] in bulk fused silica, utilizing a LightFab 3D printer (LightFab GmbH). The cross-slot

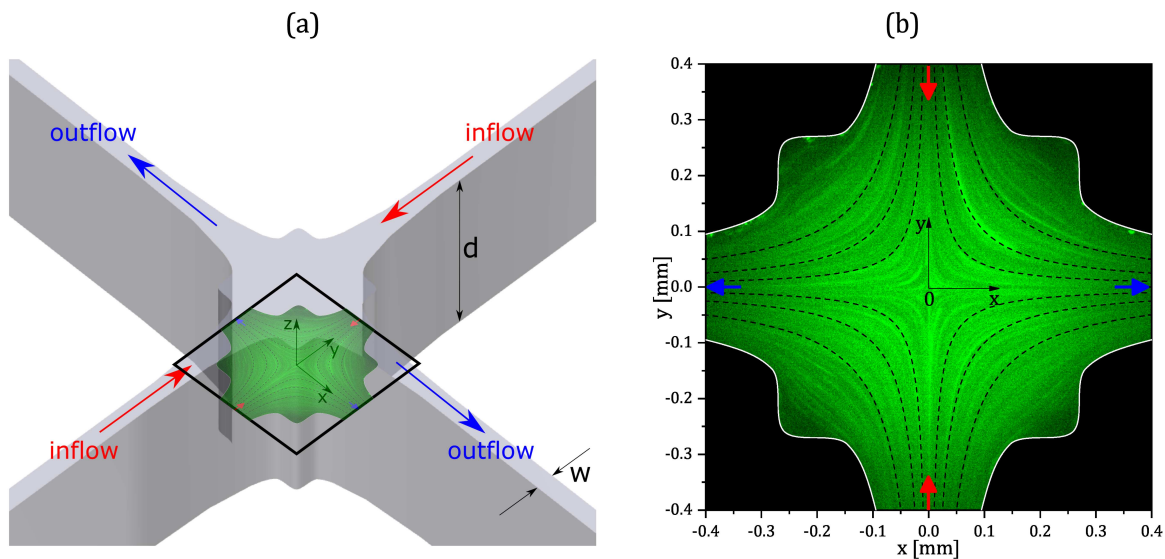


Figure 6.1: (a) Schematic representation of the OSCER geometry with height d and width w . Red and blue arrows indicate inflow and outflow directions, respectively. (b) Illustration of symmetric Newtonian flow inside the OSCER device in the middle of the cross-slot height from (a), showing a streak image from fluorescent tracer particles in water at $Re = 1.6$. Black dashed lines represent hyperbolic streamlines.

is fitted between two glass windows to enclose the channels with optical access. Four holes are ultrasonically drilled in one window to connect the channel with in- and outlet tubing. We use four servo-driven syringe pumps (neMESYS, Cetoni GmbH), fitted with Hamilton Gastight syringes, to inject fluid in two opposed inlet channels and simultaneously withdraw fluid from the other two opposed outlet channels at equal rates. The depth of the OSCER device is $d = 2$ mm and the width of the in- and outlet channels are $w = 100$ μm , resulting in a high aspect ratio $d/w = 20$. The Reynolds number Re in the OSCER is defined as

$$Re = \frac{\rho U D_h}{\eta_0}, \quad (6.1)$$

where ρ and η_0 are the fluid density and zero shear viscosity, respectively. $U = Q/(wd)$ is the average flow velocity, with volumetric flow rate Q , and $D_h = 2wd/(w+d) \approx 2w$ is the hydraulic diameter. For the shear-thickening sample 10 mM CTAB/NaSal, $R = 0.5$ discussed below, we use $\rho = 0.996$ g/cm^3 and $\eta_0 = 3$ mPa s to calculate Re .

The flow field inside the OSCER in the $x - y$ plane ($z = 0$) is characterized using a μPIV system (TSI Inc.). Samples are seeded with 0.02 wt% carboxylate-modified microspheres (FluoSpheres) of diameter $d_p = 1$ μm with excitation and emission wavelengths of 535 nm and 575 nm, respectively. The OSCER device is mounted on an inverted microscope (Nikon Eclipse Ti), equipped with a CMOS camera (1280×800 pixel, Phantom Miro M310, Vision Research Inc.) and a $10\times$ lens (Nikon Plan Fluor, NA = 0.3). The measurement depth with this setup is $\delta z_m \approx 30$ μm ($\delta z_m/d \approx 0.015$). The camera is synchronized with a dual-pulsed Nd:YLF laser (Terra PIV, Continuum

Inc.), which illuminates the sample with short laser pulses ($\lambda_l = 527$ nm, $\delta t_l < 10$ ns). A standard cross-correlation PIV algorithm (TSI Insight 4G software), with interrogation areas of 32×32 pixels and Nyquist criterion is used to perform quantitative analysis of the flow field inside the microfluidic device.

Furthermore, we measure the flow-induced birefringence during planar extension employing two different techniques. Quantitative experiments are performed with an Excimer MicroImagerTM (Hinds Instruments Inc.). The device is equipped with a $10\times$ lens and a CCD camera (2048×2048 pixel). A dual photoelastic modulator system and a stroboscopic illumination technique are used to record seven images at a frame rate of 1 fps and to determine the pixelwise sample retardance δ and angle of high refractive index Θ [208, 209]. Additionally, we visualize time-resolved qualitative FIB inside the OSCER using an optical train that consists of a white light source, a polarizer (45°), the flow cell with outlets oriented at 0° , a second polarizer (-45°) and a CCD camera (1024×1024 pixel) with a $10\times$ lens. With such a configuration, the measured intensity depends upon the micellar orientation angle as well as the degree of micellar alignment. However, because the orientation in the OSCER device is known to be along the stretching direction (i.e. 0°), the signal intensity can be related to the optical anisotropy, with bright regions indicating more significant alignment of micelles. Based on the stress-optical rule, the signal intensity is also related to the principal stress difference in the flowing fluid [87]. Images are recorded with an exposure time of 20 ms at 10 Hz.

6.1.2 Stagnation point flow of Newtonian fluids

We test our microfluidic setup, by characterizing the flow of water, covering a broad range of elongation rates $\dot{\epsilon}$. A brief summary of the most important results, as derived from PIV analysis, is shown in Fig. 6.2.

The normalized velocity field $\sqrt{v_x^2 + v_y^2}/U$ of water in the OSCER at $Re = 1.6$ is plotted in Fig. 6.2(a). For a Newtonian fluid, steady flow behavior in the OSCER device is characterized by a flow field with a centrally located stagnation point about which hyperbolic streamlines divide symmetrically, in accordance with PIV experiments on other Newtonian fluids [204]. In microfluidics, the onset of inertially-driven secondary flow begins for $Re \gtrsim 10$ [73] and we therefore limit our experiments to $Re < 10$. In the OSCER, the velocity component v_x in x direction along $y = 0$ is proportional to x , as shown in Fig. 6.2(b) for $0.016 \leq Re \leq 1.6$. Hence the velocity gradient $\partial v_x / \partial x|_{y=0}$ is constant and defines the elongation rate $\dot{\epsilon}$ imposed on the fluid in the OSCER [199, 203]. For our channel geometry, we find the proportionality

$$\dot{\epsilon} = \frac{0.197 U}{w}, \quad (6.2)$$

between elongation rate $\dot{\epsilon}$ and average flow velocity U (see Fig. 6.2(c)) in close agreement with the expectation for a two-dimensional flow, which is as expected for a channel with such high aspect ratio, and indicates that the flow profile is almost uniform through most of the depth.

Since we examine the time-dependent behavior of surfactant solutions in the OSCER, we probe the transient flow of water at the marked position in Fig. 6.2(a). The velocity

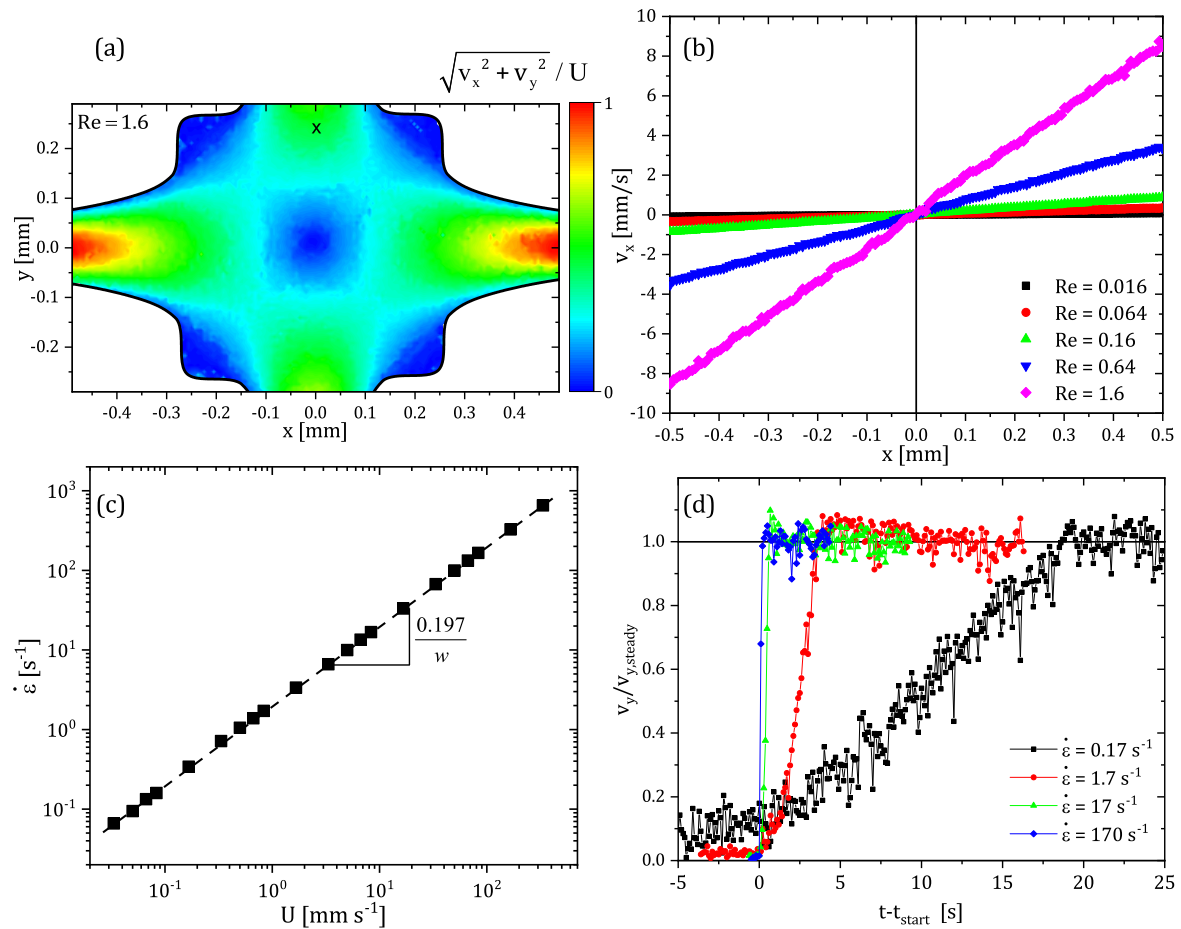


Figure 6.2: Planar elongational flow of water using a microfluidic OSCER. (a) Normalized velocity field $\sqrt{v_x^2 + v_y^2}/U$ at $Re = 1.6$. (b) Velocity component v_x in x direction along $y = 0$ for $0.016 \leq Re \leq 1.6$. (c) Elongation rate $\dot{\epsilon}$ as function of the average flow velocity U , showing the proportionality $0.197/w$. (d) Transient behavior, depicted by normalized velocity $v_y/v_{y,\text{steady}}$ for $0.17 \leq \dot{\epsilon} \leq 170$ s $^{-1}$ at the position that is marked by an x in Fig. 6.2(a).

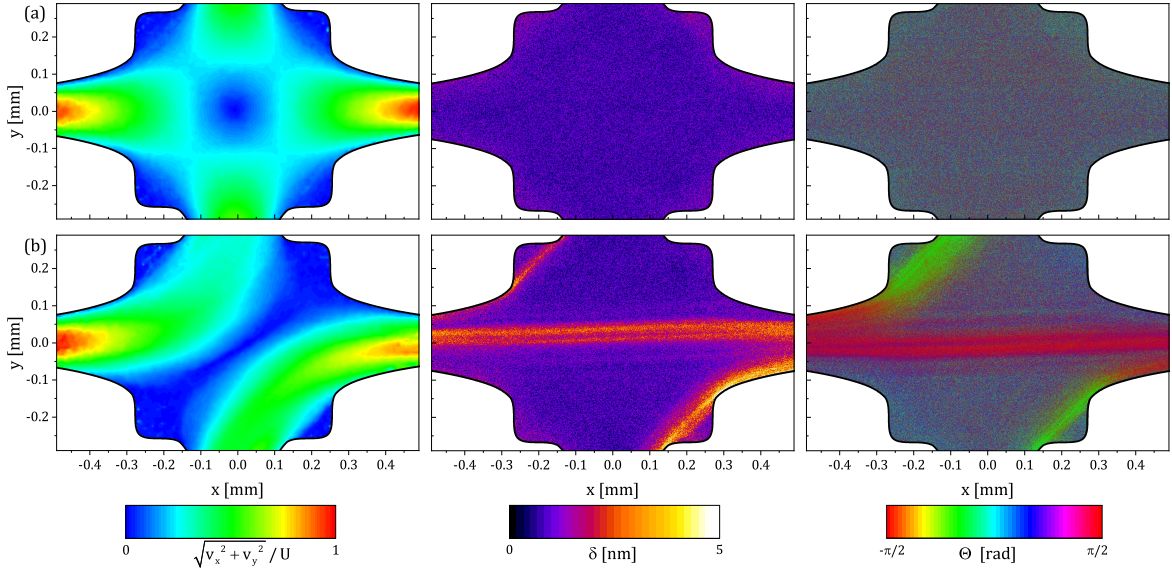


Figure 6.3: Time evolution of the velocity field and the flow-induced birefringence for 10 mM CTAB/NaSal, $R = 0.5$ solution in the OSCER. (a) At the start of the experiment and (b) after 60 s. At both times $\dot{\epsilon} = 3 \text{ s}^{-1}$ and $Re = 0.19$. Left column: normalized velocity fields; middle column: retardance; right column: angle of slow optical axis.

component v_y is normalized by the steady velocity in y direction $v_{y,\text{steady}}$ when the flow field is fully developed and plotted over the normalized time $t - t_{\text{start}}$ in Fig. 6.2(d) for $0.17 \leq \dot{\epsilon} \leq 170 \text{ s}^{-1}$. Here, t_{start} denotes the time when the four syringe pumps are switched on. For $\dot{\epsilon} = 0.17 \text{ s}^{-1}$, steady flow is achieved after a time interval of $t_{\text{ind}} \approx 20 \text{ s}$. This induction time t_{ind} decreases with increasing elongation rate $\dot{\epsilon}$. This observation is relevant for the following experiments, since transients in the flow field can superimpose time-dependent structural changes in surfactant solutions, depending on the magnitude of each effect.

In summary, Newtonian fluids like water show a symmetric flow field, resulting in a homogeneous extensional deformation of the fluid along the outflow centerline, where the elongation rate $\dot{\epsilon}$ can be controlled by applying a certain volumetric flow rate. We use the dependency shown in Fig. 6.2(c) and Eq. 6.2 for further measurements.

6.2 Results and discussion

6.2.1 Time-dependent flow instability of dilute solutions

Here, we examine the flow of low concentrated surfactant solutions through a microfluidic OSCER device. We focus on a representative 10 mM CTAB/NaSal, $R = 0.5$ solutions, which shows a heterogeneous flow inside filaments during uniaxial extension. The flow field, as well as flow-induced structural changes, are probed, using μPIV and flow-induced birefringence measurements in a broad range of elongation rates $\dot{\epsilon}$.

Figure 6.3 shows the evolution of the flow field, the retardance δ and the angle of

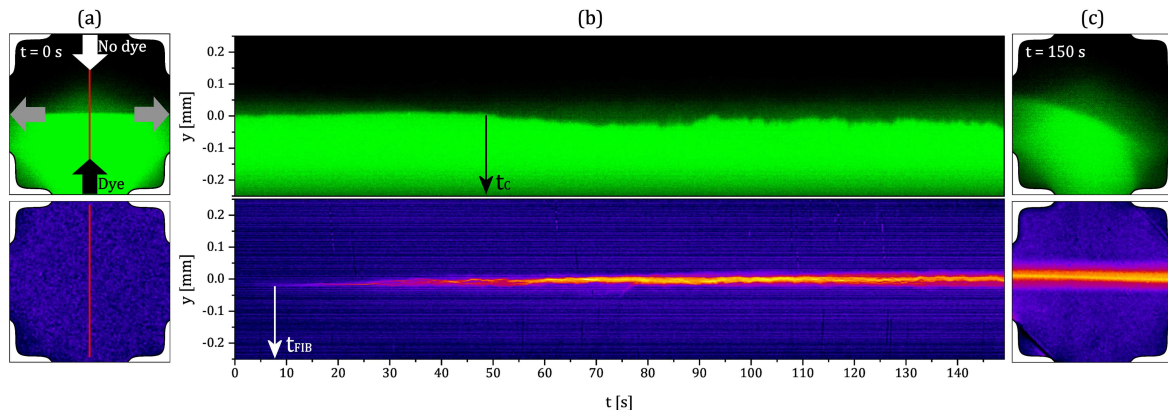


Figure 6.4: Evolution of the flow field probed by dye imaging (top) and birefringence imaging (bottom) of a 10 mM CTAB/NaSal, $R = 0.5$ solution in the OSCER. (a) Images at start of experiment $t = 0$ s, (b) evolution across red lines in (a), and (c) after $t = 150$ s. Colors represent normalized intensities of the dye and qualitative birefringence. *Reproduced with permission from Springer Nature [1].*

high refractive index Θ at an elongation rate of $\dot{\epsilon} = 3 \text{ s}^{-1}$, corresponding to $Re = 0.19$. The top row displays the initial situation at the start of the experiment, the bottom row corresponds to $t = 60$ s in the same measurement. Since no fluid relaxation time λ can be derived from SAOS measurements, we are not able to calculate a Weissenberg number Wi that characterizes the ratio between the deformation rate and the relaxation rate, $Wi = \dot{\epsilon}\lambda$.

At the beginning of the experiment, the flow field is steady Newtonian-like and symmetric with a centrally located stagnation point, similar to Fig. 6.2(a). The retardance is at the lower detection limit of the device and no orientation is observed. However, the flow field and the FIB change dramatically over time, as shown in the lower row in Fig. 6.3, referring to $t = 60$ s after the experiment started. A large scale symmetry breaking results in a globally asymmetric flow field. Fluid entering the top inlet exits through the left outlet, while fluid coming from the bottom inlet flows through the right outlet channel. This flow bifurcation is observed in both directions at random in the symmetric cross-slot device. Additionally, a birefringent strand develops along the outflow axis and along the channel walls. Here, surfactant micellar structures are oriented by the extensional flow field and the birefringent strand in the center is slightly bended according to the asymmetric flow field.

Next, we focus on the time-dependency, using dye imaging as another method to quantify the time t_c at which the flow undergoes transition. We employ a differential spinning disk (DSD2) confocal microscope (Andor Technology Ltd) and use a surfactant solution containing $10 \mu\text{M}$ fluorescent rhodamine B flowing through one inlet, while an undyed solution is introduced in the second inlet channel.

In Fig. 6.4(a) and (c), we show confocal microscope images of the dye imaging and the normalized intensity for the qualitative FIB measurement at $t = 0$ s and $t = 150$ s, respectively. The elongation rate is $\dot{\epsilon} = 3 \text{ s}^{-1}$ and the Reynolds number is $Re = 0.19$. Space-time diagrams in (b) show the evolution of the signals across $x = 0$, indicated

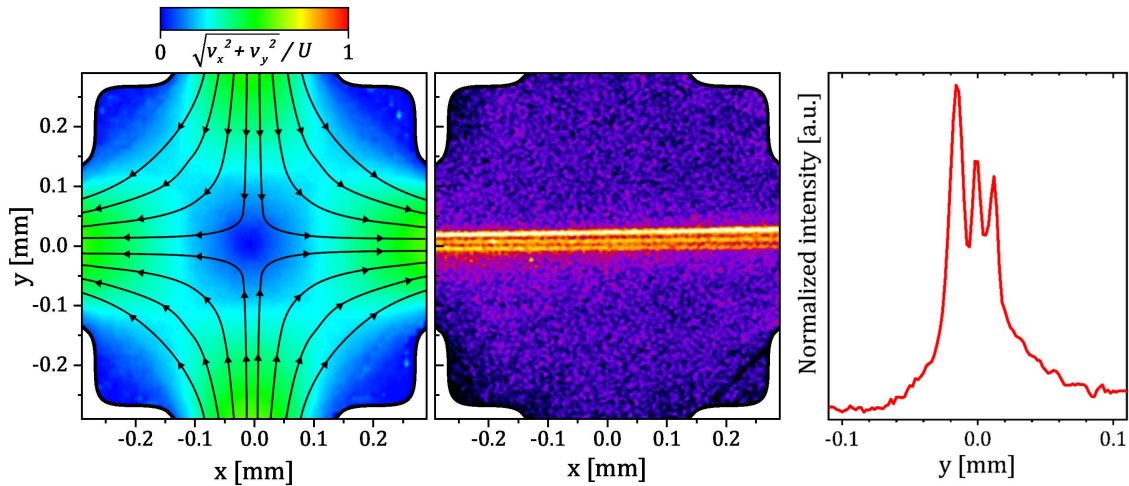


Figure 6.5: Normalized velocity (left) with superimposed hyperbolic streamlines from PIV measurements and normalized intensity of FIB in the whole OSCER device (middle) and across $x = 0$ (right) for a 10 mM CTAB/NaSal, $R = 0.5$ solution at $t = 32$ s after the experiment started. The elongation rate is $\dot{\epsilon} = 3 \text{ s}^{-1}$ and the Reynolds number is $Re = 0.19$. *Reproduced with permission from Springer Nature [1].*

by the red lines at $t = 0$ s. In the beginning, the flow field stays symmetric until the flow bifurcates at t_c , indicated by the fluctuations in the interface between the dyed and undyed solutions in the top of Fig. 6.4(b). These results are in quantitative agreement with time-resolved PIV measurements. Prior to the symmetry breaking, a single birefringent strand emerges at $t_{\text{FIB}} \approx 8$ s when the flow is still symmetric. This strand splits up into several bands that start to oscillate laterally, similarly to the spatiotemporal fluctuations of the asymmetric flow field. However, the number of bands seems to change over time as the strands collapse and split continuously. We note that the exposure time in qualitative FIB measurements is much smaller than the temporal fluctuations of the FIB signal reported in Fig. 6.4.

To emphasize the occurrence of multiple birefringent strands, we show the velocity field and the birefringence signal in the OSCER device at $t = 32$ s in Fig. 6.5. Here, the flow field is still symmetric, with a centrally located stagnation point about which incoming hyperbolic streamlines divide symmetrically. A constant elongation rate ($\dot{\epsilon} = 3 \text{ s}^{-1}$) is imposed on the fluid along the outflow direction, i.e. $y = 0$. While the flow field is still uniform and well-defined, flow-induced birefringence emerges and three individual birefringent bands are clearly distinguishable in the middle of Fig. 6.5. Consequently, we find bands of different stresses coexisting at the same deformation rate, based on a qualitative interpretation of the stress-optical rule [87]. The right panel of Fig. 6.5 shows the normalized birefringence intensity across the y -direction at $x = 0$. We estimate the spatial scale of the mesoscopic bands to be approximately $15 \mu\text{m}$, much larger than the length scale of WLM bundles (roughly 350 nm , as deduced from scanning electron microscopy (SEM)) that formed flow-induced structured phases in similar dilute surfactant solutions [77]. At higher surfactant and salt concentrations, WLM can grow up to roughly $3 \mu\text{m}$, as derived from light scattering experiments under rest [210], as well as estimated from their zero shear viscosity [211]. Even these length

scales are much smaller than the spatial dimensions we observe in Fig. 6.5. This is the first direct observation of such a multivalued relation between stress and elongation rate in a planar elongation flow, as recently reported by Dutta and Graham [161]. The authors presented a mechanistic constitutive model for surfactant solutions with flow-induced structure formation that predicts a multivalued stress at one global deformation rate in both shear and extension. Here, we present the first evidence of such behavior for dilute surfactant solution during elongational deformation.

Before the fluid enters the actual cross-slot and is deformed in a planar extensional manner, it is transported through the rectangular inlet channels. Here, the sample experiences shear forces, which can induce structural changes, e.g. SIS. Therefore, we examine the velocity profile and the FIB in the inlet channels, before the sample enters the cross-slot. In Fig. 6.6, the normalized velocity v_y/U in direction y towards the cross-slot across the channel width as well as the retardance δ are shown at a distance of $y = 1.5$ mm upstream of the central stagnation point. Measurements are performed at a time when the flow inside the cross-slot is still symmetric and when multiple birefringence bands emerge along the outflow direction in the OSCER, similar to Fig. 6.7. The elongation rate in the OSCER is $\dot{\epsilon} = 3 \text{ s}^{-1}$ and the nominal wall shear rate in the inlet channel can be estimated as $\dot{\gamma}_{\text{wall}} \approx 6U/w = 6 \text{ s}^{-1}$, due to the large aspect ratio of the device. At this point, the velocity profile upstream shows a Poiseuille flow with a parabolic shape, as indicated by the red line in Fig. 6.6, while the birefringence is in the lower detection limit of the device. We do not observe any banding due to structural changes of the surfactant solutions caused by shear in the straight channel before the fluid enters into the cross-slot, as reported for higher concentrated surfactant solutions [72]. Also, we do not observe spatiotemporally dependent jets of high velocity in the rectangular channels that were recently reported during the flow of viscoelastic wormlike micellar solutions flowing through rectangular microchannels [212]. Hence, the observations shown in Figs. 6.3, 6.4 and 6.5 arise solely by the strong elongation of the flow field inside the central part of the OSCER device.

Employing time-resolved μ PIV measurements and dye imaging on low concentrated samples, we determine the time t_c for the onset of the symmetry breaking instability shown in Fig. 6.5. This time decreases with increasing applied elongation rate, as shown in Fig. 6.7. Note that t_c is at almost two orders of magnitude larger than corresponding transients at the same elongation rate, as shown in Fig. 6.2(d). Hence, the observed time-dependent phenomenon is not caused by any softness of the tubing or by start-up effects. Scaling t_c with the corresponding elongation rate $\dot{\epsilon}$ yields a constant critical Hencky strain $\varepsilon_c = \ln(\dot{\epsilon} t_c) \approx 5.5$. We note that for elongation rates smaller than the critical rate $\dot{\epsilon}_c = 1.5 \text{ s}^{-1}$, the flow stays Newtonian-like with no detectable FIB signal. In chapter 3, we estimate the relaxation time for this dilute surfactant solution to be smaller than $\lambda \ll 0.02$ s. Hence, the critical Weissenberg number $Wi_c = \dot{\epsilon}_c \lambda$ in planar elongation for the instability to arise is smaller than $Wi_c \ll 0.03$. Similar behavior is found for the second investigated dilute surfactant solution 30 mM CTAB/NaSal, $R = 0.35$. Here, we also find a time-dependent transition from a steady symmetric to asymmetric flow with the emergence of multiple birefringent bands. The critical elongation rate $\dot{\epsilon}_c = 8 \text{ s}^{-1}$ and total strain $\varepsilon_c \approx 6.4$ are slightly higher than for 10 mM CTAB/NaSal, $R = 0.5$.

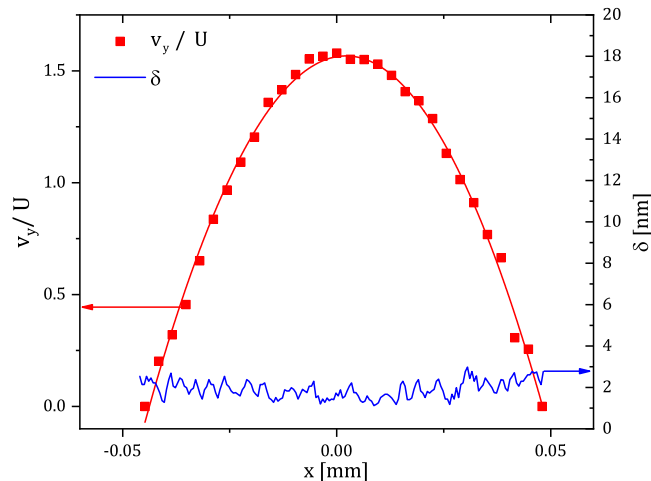


Figure 6.6: Normalized velocity component in y direction v_y/U (red squares) and retardance δ (blue line) across x coordinate along the inlet channel with width w . Data is acquired at a distance of $y = 1.5$ mm upstream of the stagnation point. The red line represents a parabolic fit of the velocity data and the elongation rate is $\dot{\epsilon} = 3 \text{ s}^{-1}$.

Dubash *et al.* [157] examined the flow behavior and birefringence of two weakly viscoelastic, shear-thickening wormlike micellar solutions. A flow instability resulted in an immediate transition from a stable symmetric flow to an unsteady flow. They observed a very faint birefringent band along the centerline. However, the authors did not report any time-dependency at a critical elongation rate. In contrast to our experiments, the fluctuations in FIB and the flow transition, indicating an unsteady state, appeared at very high elongation rates ($\dot{\epsilon} > 200 \text{ s}^{-1}$). Our results extend these observations since we find a regime where the flow is steady and asymmetric. But upon increasing the flow rate further, we eventually find the unstable flow state.

6.2.2 Elastic flow instability of high concentrated solutions

Furthermore, we examine two viscoelastic, shear thinning samples in planar elongation that show a uniform flow inside the filament during uniaxial thinning (10 mM CTAB/NaSal, $R = 30$ and 30 mM CTAB/NaSal, $R = 7.67$). Figure 6.8 shows the evolution of the flow field, the retardance δ and the angle of high refractive index Θ with increasing elongation rate $\dot{\epsilon}$ for a 30 mM CTAB/NaSal, $R = 7.67$ solution. The top row (a) displays the flow behavior at $\dot{\epsilon} = 0.17 \text{ s}^{-1}$, the middle row (b) at $\dot{\epsilon} = 0.7 \text{ s}^{-1}$, and the bottom row (c) at $\dot{\epsilon} = 1.4 \text{ s}^{-1}$. Further, we calculate the Weissenberg number Wi and the Reynolds number Re in the OSCER. For the 30 mM CTAB/NaSal, $R = 7.67$ surfactant solution, the shear relaxation time $\lambda = 4 \text{ s}$ is determined from SAOS measurements (see Fig. 2.4). In the experiments shown here, the Reynolds number is very small $Re \ll 1$ and the Weissenberg number varies between $0.68 \leq Wi \leq 4.1$ with increasing elongation rate. Hence, the elasticity number $El = Wi/Re$ is always greater than unity in the results shown, indicating that the elastic forces dominate inertia effects for all investigated elongation rates.

At very small elongation rates, the flow is Newtonian-like and no birefringence signal

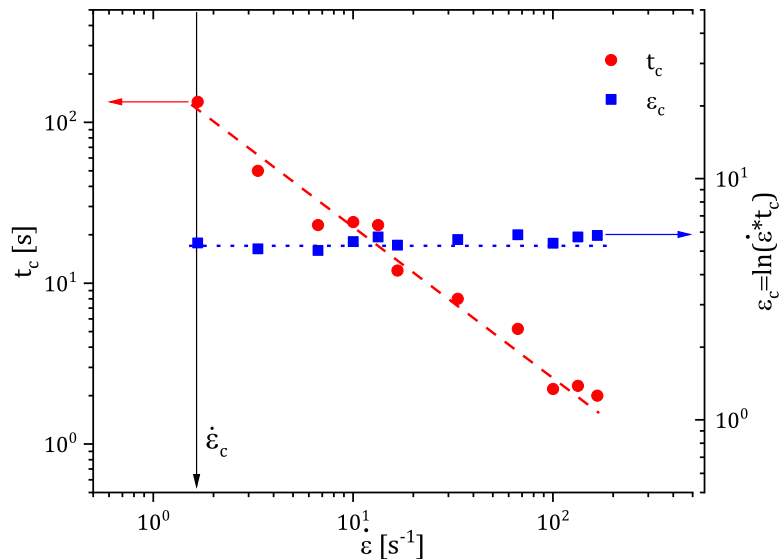


Figure 6.7: Time required for onset of asymmetry breaking t_c and critical total strain ε_c as a function of applied strain rate $\dot{\varepsilon}$ in the OSCER for 10 mM CTAB/NaSal, $R = 0.5$. Reproduced with permission from Springer Nature [1].

can be detected (Fig. 6.8(a)). Upon increasing the flow rate, a single stable birefringent strand appears along the outflow direction, while the flow field still remains symmetric at $Wi = 2.8$. At this point, birefringence also arises along the inlet channel walls, indicating the orientation of surfactant micelles. When increasing the elongation rate further ($\dot{\varepsilon} = 1.4 \text{ s}^{-1}$ and $Wi = 5.6$), the flow field changes from steady symmetric to steady asymmetric. Here, the birefringent strand bends according to the asymmetry of the flow field. Increasing the elongation rate to very high values results in an unsteady flow field (not shown). Similar results are found for the second higher concentrated sample (10 mM CTAB/NaSal, $R = 30$).

Our results are in qualitative accordance with stagnation point flow experiments on entangled wormlike micellar surfactant solutions in standard shaped cross-slots that were reported before [156, 157, 158, 159]. Pathak and Hudson [156] used μ PIV and birefringence microscopy to study the flow of a 30 mM CTAB/NaSal, $R = 8$ solution and a 100 mM CPyCl/NaSal $R = 0.6$ solution. Above a critical Weissenberg number $Wi_c > 0.5$, the flow field was found to be steady symmetric and both solutions show sharply peaked birefringent and transmittance bands along the outflow direction. The same CPyCl/NaSal system was studied by Haward *et al.* [159] using a standard cross-slot flow channel. The authors performed a detailed quantitative study of the flow field, the flow-induced birefringence and the macroscopic bulk pressure drop over a wide range of deformation rates. At low Wi , the flow field was steady symmetric, accompanied by a slender birefringent strand. Upon increasing Wi above unity, the flow field bifurcated and became asymmetric, with a rotated birefringent strand. The origin for this bifurcation was found to be purely elastic since the Reynolds numbers were vanishingly small. At very high rates, the flow became time-dependent with rapid fluctuations in the birefringent signal.

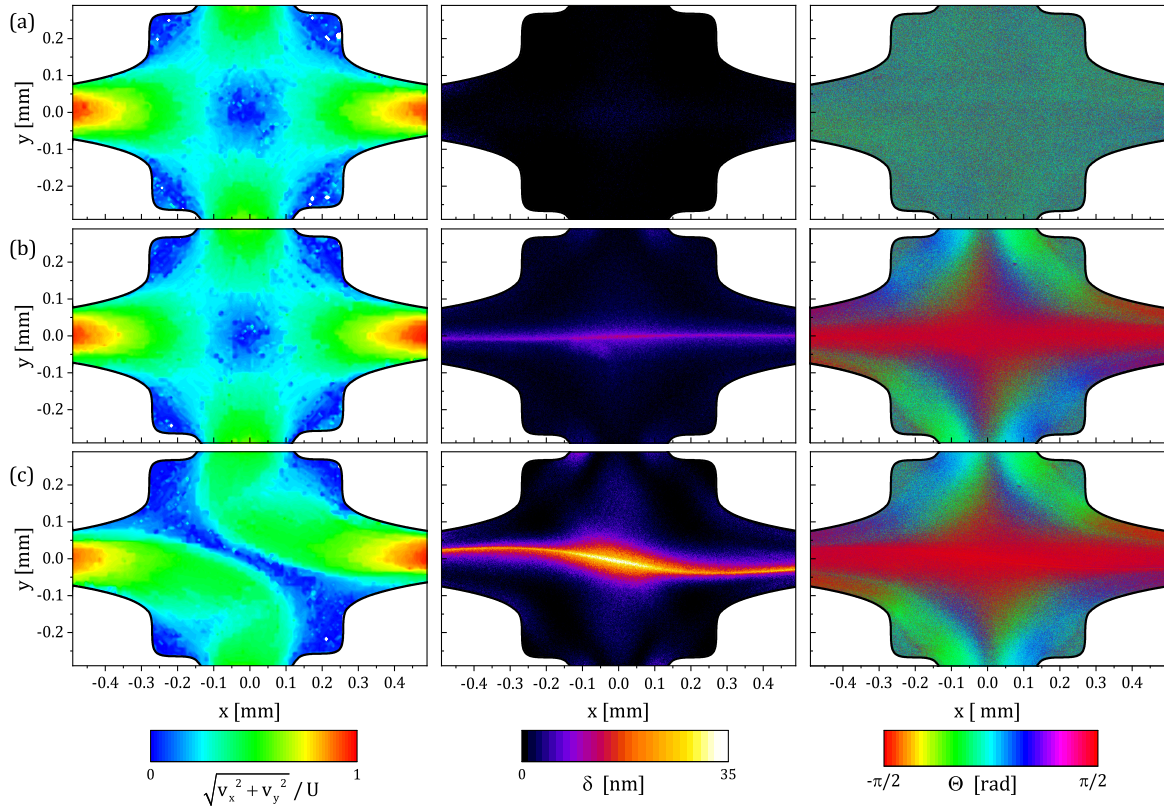


Figure 6.8: Evolution of the velocity field and the flow-induced birefringence for 30 mM CTAB/NaSal, $R = 7.67$ solution in the OSCER. Left column: normalized velocity fields; middle column: retardance; right column: angle of slow optical axis. (a) $\dot{\epsilon} = 0.17 \text{ s}^{-1}$, $Re = 1.4 \times 10^{-6}$, $Wi = 0.68$, $El = 4.9 \times 10^5$. (b) $\dot{\epsilon} = 0.7 \text{ s}^{-1}$, $Re = 1.4 \times 10^{-5}$, $Wi = 2.8$, $El = 2 \times 10^5$. (c) $\dot{\epsilon} = 1.4 \text{ s}^{-1}$, $Re = 3.4 \times 10^{-5}$, $Wi = 5.6$, $El = 1.7 \times 10^5$.

Haward and McKinley [158] constructed a stability diagram for viscoelastic flows of polymeric fluids in cross-slot geometries. They used a series of shear-thinning CPyCl/NaSal/NaCl solutions that showed a pronounced stress-plateau in the flow curve at higher concentrations, indicative of shear banding. The authors also reported the evolution from a steady symmetric flow with a slender birefringent strand, to a steady bifurcated flow at $Wi > 2$, until an unsteady time-dependent state is reached with increasing Wi . Similar instabilities with the formation of lip vortices were found for viscoelastic CTAB/NaSal solutions by Dubash *et al.* [157], using standard cross-slots. Our results confirm the previously reported flow transitions in wormlike micellar solutions in an optimized-shaped cross-slot instead of a standard cross-slot for the first time. However, the critical Weissenberg number $Wi_c \approx 2$ at which a birefringent strand appears is slightly higher compared to the results of Pathak and Hudson [156] ($Wi_c \approx 0.5$).

6.3 Conclusions

We probe the flow behavior of surfactant solutions in a microfluidic optimized-shape cross-slot extensional rheometer that generates a planar elongational flow field. A combination of PIV and FIB imaging techniques is employed to study flow and microstructural transitions, covering a broad range of elongation rate. Highly concentrated surfactant solutions exhibit a transition from a steady symmetric to a steady asymmetric flow field with the emergence of a localized birefringent band above a critical Weissenberg number, in accordance with similar experiments on wormlike micellar and polymer solutions. We find this elasticity induced flow instability in planar elongation for solutions that show the expected homogeneous flow during filament thinning in uniaxial extension. However, for dilute solutions that exhibit heterogeneous flow inside the filaments, with unusual filament lifetimes and filament length, we discover a unique flow instability during planar extension in the OSCER. At a critical elongation rate, flow transitions from a steady symmetric towards a steady asymmetric flow over time. A critical total strain is required for this transition, irrespective of the elongation rate. Prior to the symmetry breaking, multiple birefringent strands emerge, indicating multiple stresses at one global elongation rate. This is the first experimental observation of such a multivalued relation between stress and strain rate in an extensional flow field, which was theoretically predicted recently. The critical conditions (in terms of elongation rate and total strain) for this phenomenon help us to understand the heterogeneous flow during uniaxial elongation and we combine and discuss the observations obtained in different flow kinematics in the next chapter.

7 Discussion - Flow Instabilities of Dilute Surfactant Solutions in Different Flow Kinematics

In this chapter, we relate the results from uniaxial and planar elongations to the non-monotonic flow curve from steady shear experiments in an effort to provide a unifying view on the unique flow instabilities of dilute surfactant solutions. Therefore, we calculate nominal shear rates for the flow in the OSCER cross-slot and during filament thinning in CaBER measurements, defined as $\dot{\gamma}_{\text{nom,O}} = \sqrt{4} \dot{\epsilon}_{\text{nom,O}}$ and $\dot{\gamma}_{\text{nom,C}} = \sqrt{3} \dot{\epsilon}_{\text{nom,C}}$, respectively. Here, the nominal elongation rates represent the critical elongation rates $\dot{\epsilon}_c$ for the onset of a flow instability in extension that we identified in the previous chapters. We combine the critical nominal shear rates for the onset of flow instabilities of dilute surfactant solutions in different flow kinematics in Fig. 7.1. The figure shows steady shear data of a 10 mM CTAB/NaSal, $R = 0.5$ dilute surfactant solution (controlled-stress upwards ramp from Fig. 3.3 in chapter 3.2). The hatched areas represent the calculated nominal shear rate regimes for the emergence of a flow instability in the OSCER $\dot{\gamma}_{\text{nom,O}}$ and the values experienced by the fluid during the initial step stretch in CaBER experiments $\dot{\gamma}_{\text{nom,C}}$. Furthermore, the heterogeneous flow inside the filaments results in regions of localized high shear rate of $\dot{\gamma}(x)$.

For the 10 mM CTAB/NaSal $R = 0.5$ solution, we find that the flow instability in the OSCER emerges for elongation rates larger than $\dot{\epsilon}_c \approx 1.5 \text{ s}^{-1}$, hence for nominal shear rates $\dot{\gamma}_{\text{nom,O}} \approx 3 \text{ s}^{-1}$. Relating this nominal value to the non-monotonic flow curve obtained from steady shear rheometry in Fig. 7.1 shows that $\dot{\gamma}_c^* < \dot{\gamma}_{\text{nom,O}} < \dot{\gamma}_c$, hence $\dot{\gamma}_{\text{nom,O}}$ is in the hysteretic regime of the flow curve. In shear, the flow separates into vorticity bands with a multivalued stress with the emergence of flow-induced structures if the imposed shear rate is between $\dot{\gamma}_c^* \approx 1.4 \text{ s}^{-1}$ and $\dot{\gamma}_c \approx 4 \text{ s}^{-1}$. Similarly, we find bands of different stresses coexisting at the same deformation rate in OSCER experiments, indicated by multiple birefringent bands at $\dot{\epsilon} \geq \dot{\epsilon}_c$ (see Fig. 6.5).

In CaBER measurements, the elongation rate and hence the nominal shear rate passes through a broad range (i.e. $1 \leq \dot{\epsilon} \leq 10 \text{ s}^{-1}$) during the initial step stretch as discussed in chapter 4.2 (see Fig. 5.12). In this case, we find that the nominal shear rate regimes partially overlaps the hysteresis area of the flow curve $1.7 \leq \dot{\gamma}_{\text{nom,C}} \leq 17 \text{ s}^{-1}$. However, the total strain required for this transition is much larger in shear flow ($\gamma_c \approx 5 \times 10^3$, as discussed in chapter 3.2) than during extension in the OSCER ($\epsilon_c \approx 5.5$, see chapter 5.2) and during the initial step stretch in CaBER experiments ($\epsilon_c \approx 6$, as discussed in chapter 5.3).

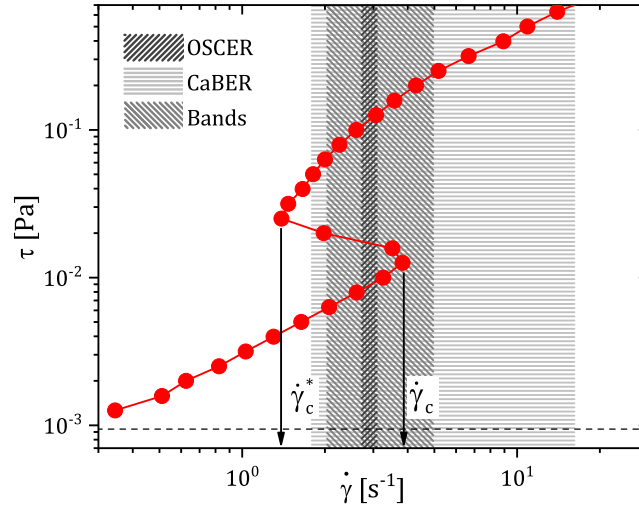


Figure 7.1: Non-monotonic flow curve of 10 mM CTAB/NaSal, $R = 0.5$ (CS up ramp from Fig. 3.3 in chapter 3.2). Hatched areas represent ranges of nominal shear rate $\dot{\gamma}_{\text{nom}}$ for OSCER and CaBER measurements, as well as between macroscopic bands during heterogeneous flow inside the filament. *Reproduced with permission from Springer Nature [1].*

Furthermore, we find that the heterogeneous velocity distribution across the filament diameter results in regions of localized high shear rate $2 \leq \dot{\gamma}(x) \leq 5 \text{ s}^{-1}$ between the different bands, as discussed in chapter 5.2. Similarly to the OSCER and CaBER measurements, the shear rate is in the hysteretic regime of the flow curve.

Table 7.1: Critical conditions in terms of rate for the onset of banding instabilities in different flow fields for two different dilute CTAB/NaSal solutions. *Bands refers to the shear rate between different bands during heterogeneous flow inside the filaments.

Flow field	crit. rates [s^{-1}]	10 mM, $R = 0.5$	30 mM, $R = 0.35$
Shear	$\dot{\gamma}_c^* - \dot{\gamma}_c$	1.4 – 4	10 – 16
OSCER	$\dot{\gamma}_{\text{nom},O}$	3	14
CaBER	$\dot{\gamma}_{\text{nom},C}$	1.7 – 17	2 – 35
Bands*	$\dot{\gamma}(x)$	2 – 5	3 – 13

In summary, we show that banding instabilities in uniaxial as well as in planar elongation emerge at nominal rates corresponding to the hysteresis regime in the shear curve, hence similar strain rates are necessary to induce such banding phenomena, irrespective of flow kinematics. Table 7.1 summarizes the critical conditions in terms of shear rate for the onset of banding instabilities in different flow fields for the 10 mM CTAB/NaSal, $R = 0.5$ solution as well as for a second dilute 30 mM CTAB/NaSal, $R = 0.35$ solution, showing similar phenomena in shear and elongation. For the 30 mM CTAB/NaSal, $R = 0.35$ solution, the critical shear rates are higher in all flow fields, yet they still are on the same order of magnitude. The non-monotonic flow curves of dilute surfactant solutions, as shown in Fig. 7.1, are a necessary condition for the existence of

a stationary vorticity banded state. We therefore state that the reported phenomena occurring in elongational flows are due to an *extensional vorticity banding* phenomenon. Such a multivalued relation between stress and elongation rate in extension was recently reported by Dutta and Graham [161], using a mechanistic constitutive model. Here, we present the first experimental evidence of such behavior for dilute surfactant solution during elongational deformation.

The origin for the multivalued relation between stress and shear rate and the vorticity banding in the hysteresis of the shear flow curve is the formation of a new and more viscous phase - a shear-induced structure buildup - and different mechanisms were reported to explain the SIS phenomenon. Berret *et al.* [55] investigated very dilute CTAT solutions using shear rheometry as well as small-angle neutron scattering and proposed the coexistence of a purely viscous state with short micelles and a strongly viscoelastic network of entangled micellar aggregates. Hu *et al.* [42] observed high flow-induced birefringence and strongly nonlinear viscoelasticity accompanying the shear-induced transition. They suggested that surfactant molecules self-assemble to form new structures resulting in shear-induced coagulation. In uniaxial extension, Sachsenheimer *et al.* [5] and Omidvar *et al.* [6] attributed long filament lifetimes of low concentrated surfactant solutions in CaBER experiments to the formation of elongation-induced structures. Omidvar *et al.* [6] suggested that cylindrical micelles aggregate into big wormlike micelles under extensional flow, based on the assumption of homogeneous uniaxial deformation.

However, our PIV results show that an extensional banding, characterized by a heterogeneous distribution of axial velocities across the whole filament cross-section with flow in both axial directions, leads to surprisingly long filament lifetimes. The non-homogeneous banding instability in these low concentrated surfactant solutions shows that structure formation during extension does not occur homogeneously on a mesoscopic length scale throughout the filament, e.g. no uniform flow-induced structured phase, with entangled, branched, and multiconnected micellar bundles is formed, as reported previously for semidilute wormlike micellar solutions flowing through micro-posts [77]. Instead, we propose that during the initial step stretch in CaBER experiments, strain rate and total strain experienced by the sample are sufficient to induce a banding instability, leading to the formation of heterogeneous structures. This heterogeneity occurs randomly in the filament. The strong coupling between internal structure and flow leads to regions of localized high shear rate between coexisting macroscopic bands, where new structures can form. Although we are not able to resolve the full mechanism of flow-induced structure formation in this complex scenario up to now, our experiments in elongation as well as in shear experiments enable us to reveal a new banding instability in elongational flows and demonstrate that the occurrence of a flow instability in such solutions is a generic phenomenon, independent of flow kinematics. However, further direct structural investigations will be required to confirm this non-uniform structure formation during extension.

8 Summary and Outlook

Surfactant solutions that can self-assemble into various structures are widely used in everyday life as well as in sophisticated technical processes. The flow behavior of aqueous surfactant solutions was thoroughly studied in the last decades, mainly focusing on the shear rheology of long, flexible wormlike micelles. However, little is known about the flow behavior of dilute surfactant solutions with short, rodlike micelles, particularly in extensional flow fields, despite the omnipresence of elongational deformations in nature and technology.

In this work, we examine the elongational flow behavior of a series of commonly studied surfactant systems covering a broad range of surfactant and salt concentrations, focusing on dilute solutions. We characterize the systems by means of steady shear rheometry and investigate their flow behavior in uniaxial as well as planar elongation.

In steady shear rheometry, the examined dilute solutions exhibit a Newtonian plateau with a zero shear viscosity of $\eta_0 \approx 3$ mPa s. At a critical shear rate and total deformation, the viscosity dramatically increases by more than one order of magnitude, due to the formation of shear-induced structures. In the hysteretic regime of the non-monotonic flow curve, a vorticity banding instability emerges in shear-thickening surfactant solutions and bands bearing different stresses are stacked along the vorticity direction, as reported recently [54, 56]. Furthermore, these solutions do not show any elastic response in the linear viscoelastic regime, employing small-amplitude oscillatory shear measurements.

In order to probe the macroscopic filament formation and the breakup of these low viscosity solutions in uniaxial extension, we employ capillary breakup elongational rheometry (CaBER) as well as filament stretching and dripping-onto-substrate experiments. In CaBER experiments, unusually long filament lifetimes of several minutes are observed, as reported previously [5, 6]. At low salt/surfactant ratios, we find huge filament lifetime ratios $t_{\text{fil}}/t_{\text{fil,N}} \approx 10^5$, demonstrating that the filament lifetime during uniaxial filament thinning is orders of magnitude larger than expected, based on their shear viscosity. Additionally, we find that the filament lifetime of dilute surfactant solutions does not depend on geometrical parameters (D_0 , h_i , h_f) and stretching conditions (t_s) in CaBER experiments, as long as conditions are such that cylindrical filaments can be formed. Equipping the CaBER device with a transparent cell, filled with Newtonian PDMS oils, we find that the filament lifetime does also not depend on the interfacial tension Γ as well as on the viscosity ratio $\eta_0^{\text{surf}}/\eta_0^{\text{oil}}$ between surfactant solution and surrounding phase. Further, we demonstrate that these solutions can form filaments with a length greater than 10 cm when dripping from a nozzle or when an immersed cylinder is withdrawn from a large solutions reservoir.

These unusual observations motivate us to examine the flow kinematics inside thinning surfactant filaments. Therefore, we use a customized stretching device in combination with a particle image velocimetry (PIV) setup and determine the velocity components in x and z direction during filament thinning. For viscoelastic polymer solutions, we find a homogeneous flow field with a centrally located stagnation point, resulting in a uniform extensional flow field. However, for dilute surfactant solutions that show long filament lifetimes and long filament length in macroscopic breakup experiments, we discover an anomalous flow inside the filament. Here, we find a heterogeneous distribution of the axial velocity component v_z in the whole filament cross-section, with multiple bands of flow in opposite filament direction. These bands occur randomly in the whole filament cross-section and lead to an additional flow from the reservoir at the filament ends back into the filament, which results in global filament lifetimes t_{fil} of several minutes. Upon an increase of surfactant concentration and/or salt/surfactant ratios, the flow profile in the filament cross-section transitions towards a homogeneous flow as expected for viscoelastic fluids. By carefully investigating the flow behavior inside surfactant filaments covering a surfactant concentration regime of $5 \leq c_{\text{surf}} \leq 100$ mM as well as salt/surfactant ratio of $0 \leq R = c_{\text{salt}}/c_{\text{surf}} \leq 50$, we are able to construct uniaxial extensional flow stability maps for some of the most commonly studied surfactant systems CTAB, CPyCl, CTAC and CTAT. We find this heterogeneous flow behavior in the surfactant solutions investigated by Sachsenheimer *et al.* [5] and Omidvar *et al.* [6], who attributed the observation of such long filament lifetimes to the formation of elongation-induced structures (EIS) without further experimental evidence. Here, we demonstrate with our PIV experiments that any structure formation during extension does not occur homogeneously on a mesoscopic length scale throughout the filament. Instead, we propose that during the initial step stretch in CaBER experiments, a banding instability is induced that leads to the formation of heterogeneous structures, randomly occurring in the filament.

In order to explore the critical conditions in terms of elongation rate $\dot{\epsilon}$ and strain ϵ required for the onset of such a banding instability during elongation, we use a microfluidic optimized-shape cross-slot extensional rheometer (OSCER), combined with flow velocimetry and birefringence imaging techniques. Here, dilute surfactant systems also exhibit a flow instability in planar extension. We find a time-dependent transition from a symmetric flow towards a large-scale symmetry-breaking of the flow field at a critical elongation rate. Prior to this transition, a single localized birefringent strand emerges along the outflow direction. However, this strand splits into several individual strands, indicating multiple stresses at one global rate. This is the first experimental observation of such a multivalued relation between stress and deformation rate in extension that was recently predicted using a mechanistic constitutive model [161]. A minimum elongation rate $\dot{\epsilon}_c$, depending on sample composition, and a critical total strain ϵ_c , independent of strain rate, are required for this phenomenon to arise. Similar strain rates and total strains are also experienced by the fluids during the initial step stretch in CaBER experiments.

Finally, we relate the results in elongation to the hysteretic flow curve of the dilute surfactant systems. The critical strain rate to trigger the flow instability during CaBER and OSCER measurements is in the same range as the critical shear rate required to induce banding in vorticity direction and flow-induced structure buildup in shear.

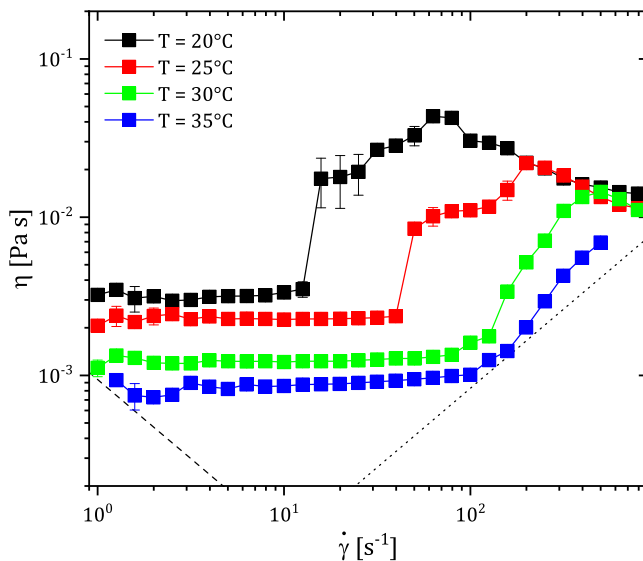


Figure 8.1: Influence of temperature on the steady shear viscosity of a dilute 30 mM CTAB/NaSal, $R = 0.35$ surfactant solution. The dashed and the dashed-dotted black lines represent the minimum torque limit of the rheometer and the critical shear rate for the onset of secondary flows.

However, the total strain required to trigger this phenomenon is larger in shear than in elongation. Although we are not able to resolve the full mechanism of flow-induced structure formation in this complex scenario up to now, our experiments in different flow fields enable us to reveal a new banding instability, independent of flow kinematics.

Our results help to understand and predict the flow behavior of fluids with low viscosity in extension and offer a more general, unifying framework regarding flow instabilities in complex fluids. Furthermore, the observed flow instability sets new limits for evaluation of extensional viscosity or relaxation times from filament stretching experiments, employed to study technical processes such as drag reduction or fiber spinning, but also biophysical phenomena such as stretching and unraveling of DNA. Future theoretical work and new numerical simulation approaches will be stimulated by our results in the interdisciplinary field between fluid mechanics, physical chemistry and process engineering.

8.1 Future prospects

This study provides various new insights into the elongational flow behavior of dilute surfactant solutions. However, there remain some aspects of further research, which are briefly discussed in the following.

All experiments presented here are performed at $T = 20^\circ\text{C}$. Nevertheless, the formation of flow-induced structures in shear experiments depends on temperature, as shown for a 30 mM CTAB/NaSal, $R = 0.35$ solution in Fig. 8.1. With increasing temperature, the zero-shear viscosity at small shear rates decreases. Further, the critical shear rate for the onset of shear-thickening $\dot{\gamma}_c$ is shifted towards higher values with increasing

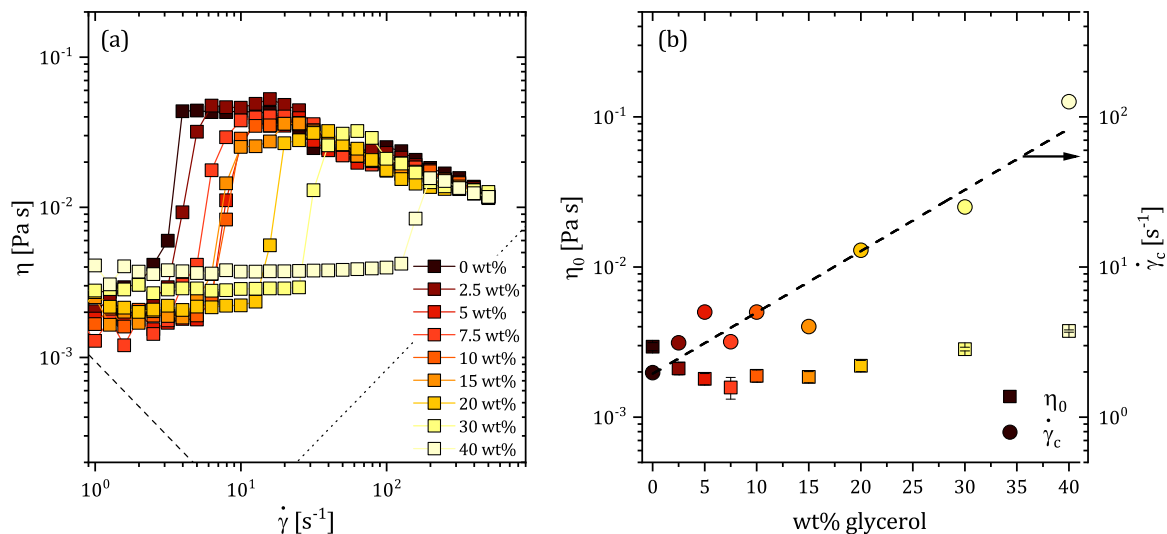


Figure 8.2: Influence of the addition of glycerol on the shear-thickening of a 10 mM CTAB/NaSal, $R = 0.5$ dilute surfactant solution. (a) Shear viscosity as a function of shear rate. (b) Zero shear viscosity and critical shear rate for the onset of shear-thickening, derived from (a). Dashed line in (b) represents a linear fit of $\dot{\gamma}_c$.

temperature. However, at higher temperatures, e.g. $T = 35^\circ\text{C}$, the shear viscosity does not increase as a consequence of SIS, but due to the onset of secondary flows at a critical shear [39], represented by the dotted line in Fig. 8.1. Varying the temperature in future CaBER as well as PIV experiments on horizontal filaments will show if a heterogeneous flow emerges inside dilute surfactant solutions at elevated temperatures or if the heterogeneous structure formation in extension diminishes at a certain temperature, similar to Fig. 8.1. Such temperature effects, and the influence on the flow-induced birefringence should also be studied in planar extension, by placing the OSCER device in a small, temperature controlled chamber. Knowledge about the temperature dependency of flow-induced structures in elongational flows is highly relevant for many technical applications that take place in a broad temperature regime, e.g. enhanced oil recovery applications.

In this study, we use water as a solvent. However, co-solvents can influence the micellar formation and thus can change the rheological behavior of water/surfactant solutions significantly [213, 214, 215]. For viscoelastic WLM solutions, the addition of glycerol as co-solvent leads to a decrease of viscosity and structural relaxation times at the viscosity maxima [216]. However, knowledge about the effect of glycerol on the rheology of dilute surfactant solutions and the shear-induced structure formation is still missing. Figure 8.2(a) shows the influence of the addition of glycerol as co-solvent on the shear-thickening behavior of a dilute 10 mM CTAB/NaSal, $R = 0.5$ solution. With an increasing amount of co-solvent, the critical shear rate for the onset of shear-thickening $\dot{\gamma}_c$ is shifted towards higher values, as shown by the circles in Fig. 8.2(b). Furthermore, the zero-shear viscosity first decreases until 10 wt% glycerol and subsequently increases (see square symbols in Fig. 8.2(b)). These preliminary experiments clearly show that the addition of a co-solvent has an effect on the SIS

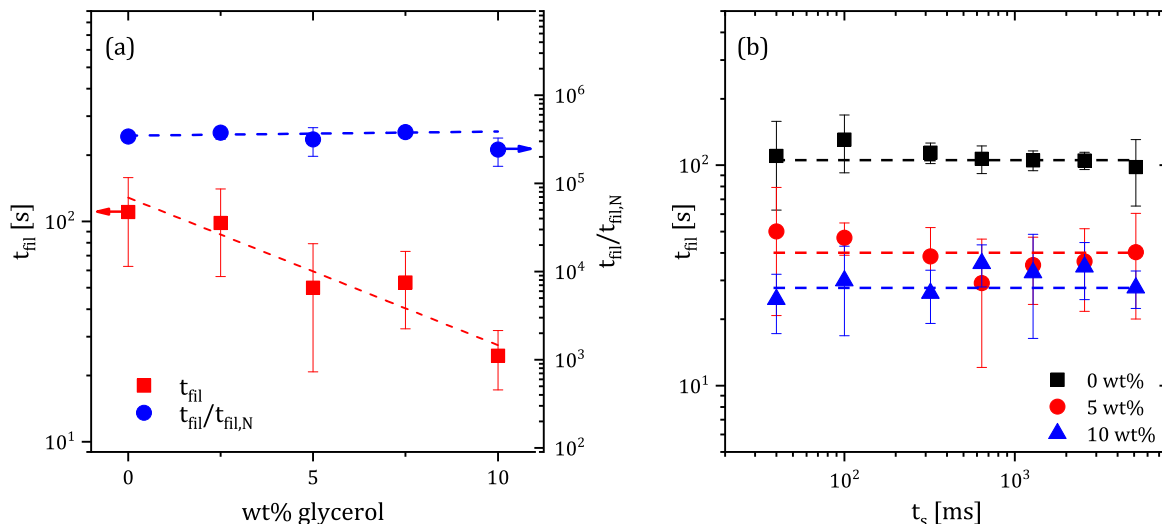


Figure 8.3: Influence of the addition of glycerol on the filament lifetime in CaBER experiments of a 10 mM CTAB/NaSal, $R = 0.5$ dilute solution. (a) Filament lifetime and filament lifetime ratio as a function of glycerol amount. (b) Filament lifetime as a function of strike time for different amounts of added glycerol.

formation in shear flow of dilute surfactant solutions.

In CaBER experiments, these mixtures show long filament lifetimes and filament lifetime ratios $t_{\text{fil}}/t_{\text{fil,N}}$, as shown in 8.3(a). The filament lifetime decreases with increasing amount of glycerol in the investigated regime, while $t_{\text{fil}}/t_{\text{fil,N}}$ remains a constant, since η_0 decreases as well (see Fig. 8.2(b)). For these solutions, the filament lifetime does not depend on the strike time t_s during the initial step stretch, as shown in Fig. 8.3(b). These preliminary results indicate, that the flow inside these filaments is heterogeneous, similar to solutions without glycerol. The addition of a co-solvent might provide an optional route to tune the shear rheology of dilute surfactant solutions at constant surfactant and salt concentrations and examine its effect on the extensional flow behavior and flow instabilities in future work.

Beyond the detailed investigations on surfactant solution behavior, our experimental method can be readily extended to study the flow inside other low viscosity fluid filaments in extensional flow fields, ubiquitous in nature or technology. In the following, preliminary results show that biopolymeric fluids such as saliva and hagfish mucus also exhibit banded flow during filament thinning.

8.2 Flow inside biopolymeric fluid filaments

Although we focus on the elongational flow behavior of dilute surfactant solutions as a model system in this study, we further employ our method to examine the flow inside thinning biological fluid filaments, such as whole human saliva and hagfish slime. Whole human saliva is collected from a healthy volunteer, who did not eat or drink for one hour before donation. Further, an aqueous 0.14 wt% hagfish slime solution, provided by IFNH Food Process Engineering Group of ETH Zurich, is prepared according to

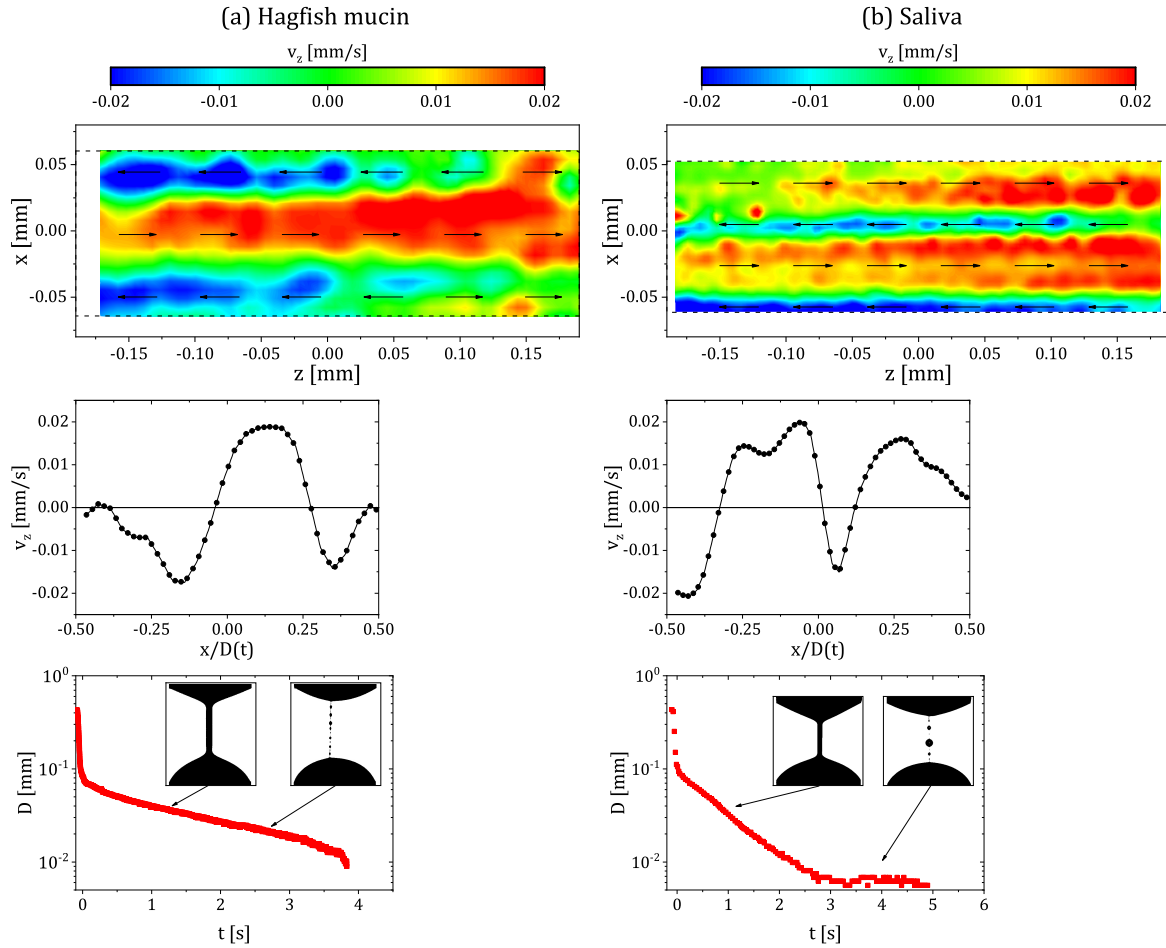


Figure 8.4: Filament thinning results of (a) a 0.14 wt% hagfish mucin solution and (b) whole human saliva. Top row shows the velocity component v_z in axial direction inside the filament during thinning, derived from PIV measurements. Results show the flow field in the $x-z$ plane in the center between the plates ($D_0 = 4$ mm). The initial displacement, final displacement, and the strike time are $h_i = 1$ mm, $h_f = 4$ mm, and $t_s = 0.5$ s, respectively. Dashed black lines represent the filament boundaries in the measured plane and arrows are to guide the eye. Second row shows the flow profiles of the axial velocity component v_z over the normalized filament, extracted from top row at $z = 0$ mm. Bottom row shows diameter as a function of time as probed by CaBER, with $D_0 = 6$ mm, $h_i = 1.5$ mm, $h_f = 7$ mm and $t_s = 40$ ms for the hagfish sample and $D_0 = 6$ mm, $h_i = 1.5$ mm, $h_f = 6$ mm and $t_s = 50$ ms for saliva. The inset pictures show snapshots of the cylindrical filament during thinning, the later ones displaying a beads-on-a-string structure. *Top and bottom panels reproduced with permission from Springer Nature [1].*

the work of Böni *et al.* [217, 218, 219]. The samples are seeded with mono-disperse fluorescent polystyrene microspheres of diameter $d_p = 0.96 \mu\text{m}$ and experiments are performed as discussed in chapter 5. Preliminary results demonstrate that biopolymeric fluids such as hagfish slime and whole human saliva also show banded flow during filament thinning, as shown in Fig. 8.4.

Figure 8.4(a) shows the PIV results during filament thinning as well as the macroscopic thinning of the 0.14 wt% hagfish slime solution behavior in CaBER. A heterogeneous velocity distribution of v_z with flow in both positive and negative axial filament direction emerges inside the cylindrical thread, similar to the flow inside thinning filaments of dilute surfactant solutions. This non-uniform flow consists of multiple bands, bearing different velocities v_z and different flow directions, shown in the second row of Fig. 8.4(a), where v_z is extracted at $z = 0 \text{ mm}$ and plotted over the normalized diameter. The global filament lifetime of this samples is $t_{\text{fil}} \approx 4 \text{ s}$ (last row in Fig. 8.4(a)). Note that PIV measurements are performed during the early thinning process, prior to the formation of beads-on-a-string structures. Furthermore, similar results are obtained during the early thinning process of whole human saliva [220] (see Fig. 8.4(b)), exhibiting a filament lifetime of $t_{\text{fil}} \approx 5 \text{ s}$, in accordance with Turcanu *et al.* [221], who found similar filament lifetimes. Both fluids were studied under uniaxial deformation before, using CaBER [217, 221, 222, 223]. Whole saliva is a mixture of different glandular secretions [224] and hagfish slime contains mucin vesicles and thread skeins [217]. Both naturally heterogeneous fluids show filament lifetimes of several seconds and exhibit a heterogeneous velocity distribution inside the cylindrical thread, similar to the results shown in chapter 5.

Although further investigations will be required to elucidate the origin for the heterogeneous flow in these fluids, the preliminary results presented in Fig. 8.4 indicate that the heterogeneous flow phenomenon is not limited to aqueous surfactant solutions. The generic phenomenon might be an important mechanism during extensional deformation of different types of low viscosity, complex fluids occurring in nature and technology, and highly relevant for many scientists from different topical areas of physics, chemistry, and biology.

9 Bibliography

- [1] S. M. Recktenwald, S. J. Haward, A. Q. Shen, and N. Willenbacher. Heterogeneous flow inside threads of low viscosity fluids leads to anomalous long filament lifetimes. *Sci. Rep.*, 9(1):7110, 2019.
- [2] B. Keshavarz, V. Sharma, E. C. Houze, M. R. Koerner, J. R. Moore, P. M. Cotts, P. Threlfall-Holmes, and G. H. McKinley. Studying the Effects of Elongational Properties on Atomization of Weakly Viscoelastic Solutions using Rayleigh Ohnesorge Jetting Extensional Rheometry (ROJER). *J. Non-Newton. Fluid Mech.*, 222:171–189, 2015.
- [3] D.H. Reneker, A.L. Yarin, E. Zussman, and H. Xu. Electrospinning of Nanofibers from Polymer Solutions and Melts. In *Adv. Appl. Mech.*, volume 41, pages 43–346. Elsevier, 2007.
- [4] S. K. Han, D. M. Shin, H. Y. Park, H. W. Jung, and J. C. Hyun. Effect of Viscoelasticity on Dynamics and Stability in Roll Coatings. *Eur. Phys. J. Spec. Top.*, 166(1):107–110, 2009.
- [5] D. Sachsenheimer, C. Oelschlaeger, S. Müller, J. Küstner, S. Bindgen, and N. Willenbacher. Elongational Deformation of Wormlike Micellar Solutions. *J. Rheol.*, 58(6):2017–2042, 2014.
- [6] R. Omidvar, A. Dalili, A. Mir, and H. Mohammadigoushki. Exploring Sensitivity of the Extensional Flow to Wormlike Micellar Structure. *J. Non-Newton. Fluid Mech.*, 252(August 2017):48–56, 2018.
- [7] P. D. Olmsted. Perspectives on Shear Banding in Complex Fluids. *Rheol. Acta*, 47(3):283–300, 2008.
- [8] S. Manneville. Recent Experimental Probes of Shear Banding. *Rheol. Acta*, 47(3):301–318, 2008.
- [9] P. Schall and M. van Hecke. Shear Bands in Matter with Granularity. *Annu. Rev. Fluid Mech.*, 42(1):67–88, 2010.
- [10] T. Divoux, M. A. Fardin, S. Manneville, and S. Lerouge. Shear Banding of Complex Fluids. *Annu. Rev. Fluid Mech.*, 48(1):81–103, 2016.
- [11] B. Saint-Michel, T. Gibaud, and S. Manneville. Uncovering Instabilities in the Spatiotemporal Dynamics of a Shear-Thickening Cornstarch Suspension. *Phys. Rev. X*, 8(3):031006, 2018.

- [12] J.-F. Berret. Rheology of Wormlike Micelles: Equilibrium Properties and Shear Banding Transitions. In *Mol. Gels*, pages 667–720. Springer-Verlag, 2006.
- [13] S. Lerouge and J.-F. Berret. *Polymer Characterization*, volume 230. Springer Berlin Heidelberg, 2010.
- [14] J. Yang. Viscoelastic Wormlike Micelles and Their Applications. *Curr. Opin. Colloid Interface Sci.*, 7(5-6):276–281, 2002.
- [15] D. Ohlendorf, W. Interthal, and H. Hoffmann. Surfactant Systems for Drag Reduction: Physico-Chemical Properties and Rheological Behaviour. *Rheol. Acta*, 25(5):468–486, 1986.
- [16] K. Arora, R. Sureshkumar, M. P. Scheiner, and J. L. Piper. Surfactant-Induced Effects on Turbulent Swirling Flows. *Rheol. Acta*, 41(1-2):25–34, 2002.
- [17] F.-C. Li, Y. Kawaguchi, B. Yu, J.-J. Wei, and K. Hishida. Experimental study of Drag-Reduction Mechanism for a Dilute Surfactant Solution Flow. *Int. J. Heat Mass Transf.*, 51(3-4):835–843, 2008.
- [18] F. Hadri and S. Guillou. Drag Reduction by Surfactant in Closed Turbulent Flow. *Int. J. Eng. Sci. Technol.*, 2(12):6876–6879, 2010.
- [19] S. Ezrahi, E. Tuval, and A. Aserin. Properties, Main Applications and Perspectives of Worm Micelles. *Adv. Colloid Interface Sci.*, 128-130(2006):77–102, 2006.
- [20] G. C. Maitland. Oil and Gas Production. *Curr. Opin. Colloid Interface Sci.*, 5(5-6):301–311, 2000.
- [21] H. Rehage and H. Hoffmann. Rheological Properties of Viscoelastic Surfactant Systems. *J. Phys. Chem.*, 92(16):4712–4719, 1988.
- [22] V. Lutz-Bueno. *Effects of Formulation and Flow on the Structure of Micellar Aggregates*. Phd thesis, ETH Zürich, 2016.
- [23] B. Kronberg, K. Holmberg, and B. Lindman. *Surface Chemistry of Surfactants and Polymers*. John Wiley & Sons, Ltd, 2014.
- [24] R. Zana and E. W. Kaler. *Giant Micelles: Properties and Applications*. CRC Press, 2007.
- [25] J. W. McBain. Mobility of Highly-Charged Micelles. *Trans. Faraday Soc.*, 9:99–101, 1913.
- [26] P. Debye. Light Scattering in Soap Solutions. *J. Colloid Interface Sci.*, 3:407–409, 1948.
- [27] J. N. Israelachvili, D. J. Mitchell, and B. W. Ninham. Theory of Self-Assembly of Lipid Bilayers and Vesicles. *Biochim. Biophys. Acta - Biomembr.*, 470(2):185–201, 1977.

-
- [28] C. A. Dreiss. Wormlike Micelles: Where do We Stand? Recent Developments, Linear Rheology and Scattering Techniques. *Soft Matter*, 3(8):956–970, 2007.
- [29] M. Rubinstein and R. H Colby. *Polymer Physics*, volume 23. Oxford University Press New York, 2003.
- [30] H. Rehage and H. Hoffmann. Shear Induced Phase Transition in Highly Dilute Aqueous Detergent Solutions. *Rheol. Acta*, 21(4-5):561–563, 1982.
- [31] J.-F. Berret, R. Gamez-Corrales, S. Lerouge, and J. P. Decruppe. Shear-Thickening Transition in Surfactant Solutions: New Experimental Features from Rheology and Flow Birefringence. *Eur. Phys. J. E*, 2:343–350, 2000.
- [32] J.-F. Berret, R. Gamez-Corrales, Y. S  r  ro, F. Molino, and P. Lindner. Shear-Induced Micellar Growth in Dilute Surfactant Solutions. *Europhys. Lett.*, 54(5):605–611, 2001.
- [33] M. E. Cates. Reptation of Living Polymers: Dynamics of Entangled Polymers in the Presence of Reversible Chain-Scission Reactions. *Macromolecules*, 20(9):2289–96, 1987.
- [34] M. E. Cates and S. J. Candau. Statics and Dynamics of Worm-Like Surfactant Micelles. *J. Phys. Condens. Matter*, 2(33):6869–6892, 1990.
- [35] R. Nagarajan. Molecular Packing Parameter and Surfactant Self-Assembly: The Neglected Role of the Surfactant Tail. *Langmuir*, 18(1):31–38, 2002.
- [36] C. W. Macosko. *Rheology: Principles, Measurements, and Applications*. Wiley-VCH, 1994.
- [37] Ronald G. Larson. *The Structure and Rheology of Complex Fluids*. OUP USA, 1999.
- [38] G. H. McKinley and T. Sridhar. Filament-Stretching Rheometry of Complex Fluids. *Annu. Rev. Fluid Mech.*, 34(1):375–415, 2002.
- [39] R. H. Ewoldt, M. T. Johnston, and L. M. Caretta. Experimental Challenges of Shear Rheology: How to Avoid Bad Data. In *Complex Fluids Biol. Syst.*, chapter 6, pages 207–241. Springer, 2015.
- [40] H. Azzouzi, J. P. Decruppe, S. Lerouge, and O. Greffier. Temporal Oscillations of the Shear Stress and Scattered Light in a Shear-Banding-Shear-Thickening Micellar Solution. *Eur. Phys. J. E*, 17(4):507–514, 2005.
- [41] V. Lutz-Bueno, J. Kohlbrecher, and P. Fischer. Shear Thickening, Temporal Shear Oscillations, and Degradation of Dilute Equimolar CTAB/NaSal Wormlike Solutions. *Rheol. Acta*, 52(4):297–312, 2013.
- [42] Y. Hu, S. Q. Wang, and A. M. Jamieson. Rheological and Flow Birefringence Studies of a Shear-Thickening Complex Fluid—A Surfactant Model System. *J. Rheol.*, 37(3):531–546, 1993.

- [43] P. Boltenhagen, Y. Hu, E.F. Matthys, and D.J. Pine. Observation of Bulk Phase Separation and Coexistence in a Sheared Micellar Solution. *Phys. Rev. Lett.*, 79(12):2359–2362, 1997.
- [44] Y. T. Hu, P. Boltenhagen, and D. J. Pine. Shear Thickening in Low-Concentration Solutions of Wormlike Micelles. I. Direct Visualization of Transient Behavior and Phase Transitions. *J. Rheol.*, 42(5):1185–1208, 1998.
- [45] C.-H. Liu and D. J. Pine. Shear-Induced Gelation and Fracture in Micellar Solutions. *Phys. Rev. Lett.*, 77(10):2121–2124, 1996.
- [46] Y. Hu and E. F. Matthys. Characterization of Micellar Structure Dynamics for a Drag-Reducing Surfactant Solution Under Shear: Normal Stress Studies and Flow Geometry Effects. *Rheol. Acta*, 34(5):450–460, 1995.
- [47] Y. T. Hu, P. Boltenhagen, E. Matthys, and D. J. Pine. Shear Thickening in Low-Concentration Solutions of Wormlike Micelles. II. Slip, Fracture, and Stability of the Shear-Induced Phase. *J. Rheol.*, 42(5):1209–1226, 1998.
- [48] I. Wunderlich, H. Hoffmann, and H. Rehage. Flow Birefringence and Rheological Measurements on Shear Induced Micellar Structures. *Rheol. Acta*, 26(6):532–542, 1987.
- [49] Y. Hu, C. V. Rajaram, S. Q. Wang, and A. M. Jamieson. Shear Thickening Behavior of a Rheopectic Micellar Solution: Salt Effects. *Langmuir*, 10(1):80–85, 1994.
- [50] R. Cressely and V. Hartmann. Rheological Behaviour and Shear Thickening Exhibited by Aqueous CTAB Micellar Solutions. *Eur. Phys. J. B*, 6(1):57–62, 1998.
- [51] J.-F. Berret, S. Lerouge, and J. P. Decruppe. Kinetics of the Shear-Thickening Transition Observed in Dilute Surfactant Solutions and Investigated by Flow Birefringence. *Langmuir*, 18(20):7279–7286, 2002.
- [52] M. Ito, Y. Yoshitake, and T. Takahashi. Shear-Induced Structure Change in Shear-Banding of a Wormlike Micellar Solution in Concentric Cylinder Flow. *J. Rheol.*, 60(5):1019–1029, 2016.
- [53] E. K. Wheeler, P. Fischer, and G. G. Fuller. Time-Periodic Flow Induced Structures and Instabilities in a Viscoelastic Surfactant Solution. *J. Non-Newton. Fluid Mech.*, 75(2-3):193–208, 1998.
- [54] V. Herle, P. Fischer, and E. J. Windhab. Stress Driven Shear Bands and the Effect of Confinement on their Structures - A Rheological, Flow Visualization, and Rheo-SALS Study. *Langmuir*, 21(20):9051–9057, 2005.
- [55] J.-F. Berret, R. Gamez-Corrales, J. Oberdisse, L. M. Walker, and P. Lindner. Flow-Structure Relationship of Shear-Thickening Surfactant Solutions. *Europhys. Lett.*, 41(6):677–682, 1998.

-
- [56] V. Herle, J. Kohlbrecher, B. Pfister, P. Fischer, and E. J. Windhab. Alternating Vorticity Bands in a Solution of Wormlike Micelles. *Phys. Rev. Lett.*, 99(15):158302, 2007.
- [57] V. Schmitt, F. Schosseler, and F. Lequeux. Structure of Salt-Free Wormlike Micelles: Signature by SANS at Rest and under Shear. *Europhys. Lett.*, 30(1):31–36, 1995.
- [58] J. Dehmoune, J. P. Decruppe, O. Greffier, H. Xu, and P. Lindner. Shear Thickening in Three Surfactants of the Alkyl Family CnTAB: Small Angle Neutron Scattering and Rheological Study. *Langmuir*, 25(13):7271–7278, 2009.
- [59] V. Lutz-Bueno, J. Kohlbrecher, and P. Fischer. Micellar Solutions in Contraction Slit-Flow: Alignment Mapped by SANS. *J. Non-Newton. Fluid Mech.*, 215:8–18, 2015.
- [60] S. Koch, T. Schneider, and W. Küter. The Velocity Field of Dilute Cationic Surfactant Solutions in a Couette-Viscometer. *J. Non-Newton. Fluid Mech.*, 78(1):47–59, 1998.
- [61] M. E. Cates and S. J. Candau. Ring-Driven Shear Thickening in Wormlike Micelles? *Europhys. Lett.*, 55(6):887–983, 2001.
- [62] M. E. Cates and S. M. Fielding. Rheology of Giant Micelles. *Adv. Phys.*, 55(7-8):799–879, 2006.
- [63] H. A. Stone, A. D. Stroock, and A. Ajdari. Engineering Flows in Small Devices. *Annu. Rev. Fluid Mech.*, 36(1):381–411, 2004.
- [64] T. M. Squires and S. R. Quake. Microfluidics: Fluid Physics at the Nanoliter Scale. *Rev. Mod. Phys.*, 77(3):977–1026, 2005.
- [65] R. Attia, D. C. Pregibon, P. S. Doyle, J. L. Viovy, and D. Bartolo. Soft Microflow Sensors. *Lab Chip*, 9(9):1213–1218, 2009.
- [66] C. Clasen and G. H. McKinley. Gap-Dependent Microrheometry of Complex Liquids. *J. Non-Newton. Fluid Mech.*, 124(1-3):1–10, 2004.
- [67] P. Nghe, G. Degré, P. Tabeling, and A. Ajdari. High Shear Rheology of Shear Banding Fluids in Microchannels. *Appl. Phys. Lett.*, 93(20):1–4, 2008.
- [68] C. Masselon, J. B. Salmon, and A. Colin. Nonlocal Effects in Flows of Wormlike Micellar Solutions. *Phys. Rev. Lett.*, 100(3):1–4, 2008.
- [69] E. Miller and J. Cooper-White. The Effects of Chain Conformation in the Microfluidic Entry Flow of Polymer-Surfactant Systems. *J. Non-Newton. Fluid Mech.*, 160(1):22–30, 2009.
- [70] C. Masselon, A. Colin, and P. D. Olmsted. Influence of Boundary Conditions and Confinement on Nonlocal Effects in Flows of Wormlike Micellar Systems. *Phys. Rev. E*, 81(2):021502, 2010.

- [71] P. Nghe, S. M. Fielding, P. Tabeling, and A. Ajdari. Interfacially Driven Instability in the Microchannel Flow of a Shear-Banding Fluid. *Phys. Rev. Lett.*, 104(24):248303, 2010.
- [72] T. J. Ober, J. Soulages, and G. H. McKinley. Spatially Resolved Quantitative Rheo-Optics of Complex Fluids in a Microfluidic Device. *J. Rheol.*, 55(5):1127–1159, 2011.
- [73] T. J. Ober, S. J. Haward, C. J. Pipe, J. Soulages, and G. H. McKinley. Microfluidic Extensional Rheometry Using a Hyperbolic Contraction Geometry. *Rheol. Acta*, 52(6):529–546, 2013.
- [74] Y. Zhao, P. Cheung, and A. Q. Shen. Microfluidic Flows of Wormlike Micellar Solutions. *Adv. Colloid Interface Sci.*, 211:34–46, 2014.
- [75] M. Vasudevan, E. Buse, D. Lu, H. Krishna, R. Kalyanaraman, A. Q. Shen, B. Khomami, and R. Sureshkumar. Irreversible Nanogel Formation in Surfactant Solutions by Microporous Flow. *Nat. Mater.*, 9(5):436–441, 2010.
- [76] P. Cheung, N. Dubash, and A. Q. Shen. Local Micelle Concentration Fluctuations in Microfluidic Flows and its Relation to a Flow-Induced Structured Phase (FISP). *Soft Matter*, 8(7):2304, 2012.
- [77] J. J. Cardiel, A. C. Dohnalkova, N. Dubash, Y. Zhao, P. Cheung, and A. Q. Shen. Microstructure and Rheology of a Flow-Induced Structured Phase in Wormlike Micellar Solutions. *Proc. Natl. Acad. Sci.*, 110(18):E1653–E1660, 2013.
- [78] R. K. Prudhomme and G. G. Warr. Elongational Flow of Solutions of Rodlike Micelles. *Langmuir*, 10(10):3419–3426, 1994.
- [79] L. M. Walker, P. Moldenaers, and J.-F. Berret. Macroscopic Response of Wormlike Micelles to Elongational Flow. *Langmuir*, 12(26):6309–6314, 1996.
- [80] C.-M. Chen and G. G. Warr. Light Scattering from Wormlike Micelles in an Elongational Field. *Langmuir*, 13(8):1374–1376, 1997.
- [81] P. Fischer, G. G. Fuller, and Z. Lin. Branched Viscoelastic Surfactant Solutions and their Response to Elongational Flow. *Rheol. Acta*, 36(6):632–638, 1997.
- [82] B. Lu, X. Li, L. E. Scriven, H. T. Davis, Y. Talmon, and J. L. Zakin. Effect of Chemical Structure on Viscoelasticity and Extensional Viscosity of Drag-Reducing Cationic Surfactant Solutions. *Langmuir*, 14(1):8–16, 1998.
- [83] A. J. Müller, M. F. Torres, and A. E. Sáez. Effect of the Flow Field on the Rheological Behavior of Aqueous Cetyltrimethylammonium p-Toluenesulfonate Solutions. *Langmuir*, 20(10):3838–3841, 2004.
- [84] M. Kato, T. Takahashi, and M. Shirakashi. Steady Planar Elongational Viscosity of CTAB/NaSal Aqueous Solutions Measured in a 4-Roll Mill Flow Cell. *Nihon Reoroji Gakkaishi*, 30(5):283–287, 2002.

-
- [85] M. Kato, T. Takahashi, and M. Shirakashi. Flow-Induced Structure Change and Flow Instability of CTAB/NaSal Aqueous Solution in 4-Roll Mill Flow Cell. *Int. Congr. on Rheol.*, 2004.
- [86] M. Kato, T. Takahashi, and M. Shirakashi. Influence of Planar Elongation Strain on Flow-Induced Structure and Flow Instability of CTAB/NaSal Aqueous Solution. *Trans. Japan Soc. Mech. Eng. Ser. B*, 72(720):1935–1942, 2006.
- [87] G. G. Fuller. *Optical Rheometry of Complex Fluids*. Oxford University Press on Demand, 1995.
- [88] S. L. Anna, G. H. McKinley, D. A. Nguyen, T. Sridhar, S. J. Muller, J. Huang, and D. F. James. An Interlaboratory Comparison of Measurements from Filament-Stretching Rheometers Using Common Test Fluids. *J. Rheol.*, 45(1):83–114, 2001.
- [89] J. P. Rothstein. Transient Extensional Rheology of Wormlike Micelle Solutions. *J. Rheol.*, 47(5):1227–1247, 2003.
- [90] L. E. Wedgewood, D. N. Ostrov, and R. B. Bird. A Finitely Extensible Bead-Spring Chain Model for Dilute Polymer Solutions. *J. Non-Newton. Fluid Mech.*, 40(1):119–139, 1991.
- [91] A. Bhardwaj, D. Richter, M. Chellamuthu, and J. P. Rothstein. The Effect of Pre-Shear on the Extensional Rheology of Wormlike Micelle Solutions. *Rheol. Acta*, 46(6):861–875, 2007.
- [92] A. Bhardwaj, E. Miller, and J. P. Rothstein. Filament Stretching and Capillary Breakup Extensional Rheometry Measurements of Viscoelastic Wormlike Micelle Solutions. *J. Rheol.*, 51(4):693, 2007.
- [93] M. Chellamuthu and J. P. Rothstein. Distinguishing Between Linear and Branched Wormlike Micelle Solutions using Extensional Rheology Measurements. *J. Rheol.*, 52(3):865, 2008.
- [94] F. Lequeux and S.J. Candau. Structural Properties of Wormlike Micelles. In T. McLeish, editor, *Theor. Challenges Dyn. complex fluids*. Kluwer Academic Publishers, Dordrecht, 1997.
- [95] D. Danino, Y. Talmon, and R. Zana. Cryo-TEM of Thread-Like Micelles: On-the-Grid Microstructural Transformations Induced during Specimen Preparation. *Colloids Surfaces A Physicochem. Eng. Asp.*, 169(1-3):67–73, 2000.
- [96] B. Yesilata, C. Clasen, and G. H. McKinley. Nonlinear Shear and Extensional Flow Dynamics of Wormlike Surfactant Solutions. *J. Non-Newton. Fluid Mech.*, 133(2-3):73–90, 2006.
- [97] N. J. Kim, C. J. Pipe, K. H. Ahn, S. J. Lee, and G. H. McKinley. Capillary Breakup Extensional Rheometry of a Wormlike Micellar Solution. *Korea Aust. Rheol. J.*, 22(1):31–41, 2010.

- [98] R. Omidvar, S. Wu, and H. Mohammadigoushki. Detecting Wormlike Micellar Microstructure using Extensional Rheology. *J. Rheol.*, 63(1):33–44, 2019.
- [99] P. A. Vasquez, G. H. McKinley, and L. Pamela Cook. A Network Scission Model for Wormlike Micellar Solutions. *J. Non-Newton. Fluid Mech.*, 144(2-3):122–139, 2007.
- [100] M. Cromer, L. P. Cook, and G. H. McKinley. Extensional Flow of Wormlike Micellar Solutions. *Chem. Eng. Sci.*, 64(22):4588–4596, 2009.
- [101] N. Germann, L.P. Cook, and A.N. Beris. Nonequilibrium Thermodynamic Modeling of the Structure and Rheology of Concentrated Wormlike Micellar Solutions. *J. Non-Newton. Fluid Mech.*, 196:51–57, 2013.
- [102] S. Dhakal and R. Sureshkumar. Uniaxial Extension of Surfactant Micelles: Counterion Mediated Chain Stiffening and a Mechanism of Rupture by Flow-Induced Energy Redistribution. *ACS Macro Lett.*, 5(1):108–111, 2016.
- [103] C. Clasen. Capillary Breakup Extensional Rheometry of Semi-Dilute Polymer Solutions. *Korea-Australia Rheol. J.*, 5:331–338, 2010.
- [104] D. T. Papageorgiou. On the Breakup of Viscous Liquid Threads. *Phys. Fluids*, 7(7):1529–1544, 1995.
- [105] G. H. McKinley and A. Tripathi. How to Extract the Newtonian Viscosity from Capillary Breakup Measurements in a Filament Rheometer. *J. Rheol.*, 44(3):653–670, 2000.
- [106] M. Okawara, T. Hasegawa, Y. Iino, and T. Narumi. Experimental Study on Pressure Loss of CTAB/NaSal Aqueous Solution through Slots and a Capillary. *Nihon Reoroji Gakkaishi*, 36(3):137–143, 2008.
- [107] M. Okawara, T. Hasegawa, N. Yamada, and T. Narumi. Experimental Study of Pressure Loss and Rheo-Optical Behavior of CTAB/NaSal Aqueous Solution under Elongational Flow. *Nihon Reoroji Gakkaishi*, 37(1):39–46, 2009.
- [108] D. M. Binding and D. M. Jones. On the Interpretation of Data from Converging Flow Rheometers. *Rheol. Acta*, 263(28):215–222, 1989.
- [109] M. S. N. Oliveira, M. A. Alves, F. T. Pinho, and G. H. McKinley. Viscous Flow Through Microfabricated Hyperbolic Contractions. *Exp. Fluids*, 43(2-3):437–451, 2007.
- [110] M. Chellamuthu, E. M. Arndt, and J. P. Rothstein. Extensional Rheology of Shear-Thickening Nanoparticle Suspensions. *Soft Matter*, 5(10):2117, 2009.
- [111] T. Takahashi and D. Sakata. Flow-Induced Structure Change of CTAB/NaSal Aqueous Solutions in Step Planar Elongation Flow. *J. Rheol.*, 55(2):225, 2011.
- [112] T. W. Wright. *The Physics and Mathematics of Adiabatic Shear Bands*. Cambridge University Press, 2002.

-
- [113] J. D. Goddard. Material Instability in Complex Fluids. *Annu. Rev. Fluid Mech.*, 35(1):113–133, 2003.
- [114] H. Rehage and H. Hoffmann. Viscoelastic Surfactant Solutions: Model Systems for Rheological Research. *Mol. Phys.*, 74(5):933–973, 1991.
- [115] S. Hooshyar and N. Germann. A Thermodynamic Study of Shear Banding in Polymer Solutions. *Phys. Fluids*, 28(6):063104, 2016.
- [116] J. K.G. Dhont and W. J. Briels. Gradient and Vorticity Banding. *Rheol. Acta*, 47(3):257–281, 2008.
- [117] S. M. Fielding. Complex Dynamics of Shear Banded Flows. *Soft Matter*, 3(10):1262, 2007.
- [118] J. P. Decruppe, R. Cressely, R. Makhloufi, and E. Cappelaere. Flow Firefringence Experiments Showing a Shear-Banding Structure in a CTAB Solution. *Colloid Polym. Sci.*, 273(4):346–351, 1995.
- [119] M. M. Britton and P. T. Callaghan. Shear Banding Instability in Wormlike Micellar Solutions. *Eur. Phys. J. B*, 7(2):237–49, 1999.
- [120] S. Manneville, J. B. Salmon, L. Bécu, A. Colin, and F. Molino. Inhomogeneous Flows in Sheared Complex Fluids. *Rheol. Acta*, 43:408–416, 2004.
- [121] S. Lerouge, M. A. Fardin, M. Argentina, G. Grégoire, and O. Cardoso. Interface Dynamics in Shear-Banding Flow of Giant Micelles. *Soft Matter*, 4(9):1808, 2008.
- [122] B. M. Marín-Santibáñez, J. Pérez-González, L. de Vargas, J. P. Decruppe, and G. Huelsz. Visualization of Shear Banding and Entry Poiseuille Flow Oscillations in a Micellar Aqueous Solution. *J. Non-Newton. Fluid Mech.*, 157(1-2):117–125, 2009.
- [123] M. A. Fardin, T. Divoux, M. A. Guedeau-Boudeville, I. Buchet-Maulien, J. Browaeys, G. H. McKinley, S. Manneville, and S. Lerouge. Shear-Banding in Surfactant Wormlike Micelles: Elastic Instabilities and Wall Slip. *Soft Matter*, 8(8):2535, 2012.
- [124] M. A. Fardin and S. Lerouge. Instabilities in Wormlike Micelle Systems: From Shear-Banding to Elastic Turbulence. *Eur. Phys. J. E*, 35(9), 2012.
- [125] M. A. Fardin, T. J. Ober, V. Grenard, T. Divoux, S. Manneville, G. H. McKinley, and S. Lerouge. Interplay Between Elastic Instabilities and Shear-Banding: Three Categories of Taylor–Couette Flows and Beyond. *Soft Matter*, 8(39):10072, 2012.
- [126] R. L. Moorcroft and S. M. Fielding. Shear Banding in Time-Dependent Flows of Polymers and Wormlike Micelles. *J. Rheol.*, 58(1):103–147, 2014.
- [127] A. K. Gurnon, C. López-Barrón, M. J. Wasbrough, L. Porcar, and N. J. Wagner. Spatially Resolved Concentration and Segmental Flow Alignment in a Shear-Banding Solution of Polymer-Like Micelles. *ACS Macro Lett.*, 3(3):276–280, 2014.

- [128] H. Mohammadigoushki and S. J. Muller. A Flow Visualization and Superposition Rheology Study of Shear-Banding Wormlike Micelle Solutions. *Soft Matter*, 12(4):1051–1061, 2015.
- [129] S. M. Fielding. Triggers and Signatures of Shear Banding in Steady and Time-Dependent Flows. *J. Rheol.*, 60(5):821–834, 2016.
- [130] S. Kuczera, C. Perge, M. A. Fardin, T. I. Brox, M. A.K. Williams, S. Manneville, and P. Galvosas. Anomalous Shear Banding Revisited with Rheo-NMR and Rheo-USV. *Rheol. Acta*, 54(7):619–636, 2015.
- [131] T. I Brox, B. Douglass, P. Galvosas, and J. R. Brown. Observations of the Influence of Taylor-Couette Geometry on the Onset of Shear-Banding in Surfactant Wormlike Micelles. *J. Rheol.*, 60(5):973–982, 2016.
- [132] M. A. Calabrese, S. A. Rogers, L. Porcar, and N. J. Wagner. Understanding Steady and Dynamic Shear Banding in a Model Wormlike Micellar Solution. *J. Rheol.*, 60(5):1001–1017, 2016.
- [133] P. F. Salipante, C. A. E. Little, and S. D. Hudson. Jetting of a Shear Banding Fluid in Rectangular Ducts. *Phys. Rev. Fluids*, 2(3):1–25, 2017.
- [134] V. Lutz-Bueno, R. Pasquino, S. J. Haward, A. Q. Shen, and P. Fischer. In-Situ Shear-Banding Quantification of Surfactant Solutions in Straight Microfluidic Channels. *J. Rheol.*, 61(4):769–783, 2017.
- [135] J. L. Goveas and P. D. Olmsted. A Minimal Model for Vorticity and Gradient Banding in Complex Fluids. *Eur. Phys. J. E*, 6(1):79–89, 2001.
- [136] P. D. Olmsted, O. Radulescu, and C.-Y. D. Lu. Johnson–Segalman Model with a Diffusion Term in Cylindrical Couette Flow. *J. Rheol.*, 44(2):257–275, 2000.
- [137] J. K. G. Dhont. A Constitutive Relation Describing the Shear-Banding Transition. *Phys. Rev. E*, 60(4):4534–4544, 1999.
- [138] O. Radulescu, P. D. Olmsted, and C.-Y. D. Lu. Shear Banding in Reaction-Diffusion Models. *Rheol. Acta*, 38(6):606–613, 1999.
- [139] M. A. Fardin, O. Radulescu, A. Morozov, O. Cardoso, J. Browaeys, and S. Lerouge. Stress Diffusion in Shear Banding Wormlike Micelles. *J. Rheol.*, 59(6):1335–1362, 2015.
- [140] N. Germann, A. Kate Gurnon, L. Zhou, L. Pamela Cook, A. N. Beris, and N. J. Wagner. Validation of Constitutive Modeling of Shear Banding, Threadlike Wormlike Micellar Fluids. *J. Rheol.*, 60(5):983–999, 2016.
- [141] M. A. Fardin, L. Casanellas, B. Saint-Michel, S. Manneville, and S. Lerouge. Shear-Banding in Wormlike Micelles: Beware of Elastic Instabilities. *J. Rheol.*, 60(5):917–926, 2016.

-
- [142] J. B. Salmon, A. Colin, S. Manneville, and F. Molino. Velocity Profiles in Shear-Banding Wormlike Micelles. *Phys. Rev. Lett.*, 90(22):4, 2003.
- [143] M. E. Helgeson, P. A. Vasquez, E. W. Kaler, and N. J. Wagner. Rheology and Spatially Resolved Structure of Cetyltrimethylammonium Bromide Wormlike Micelles Through the Shear Banding Transition. *J. Rheol.*, 53(2009):727, 2009.
- [144] Y. T. Hu and A. Lips. Kinetics and Mechanism of Shear Banding in an Entangled Micellar Solution. *J. Rheol.*, 49(5):1001–1027, 2005.
- [145] A. K. Gurnon, C. R. Lopez-Barron, A. P. R. Eberle, L. Porcar, and N. J. Wagner. Spatiotemporal Stress and Structure Evolution in Dynamically Sheared Polymer-Like Micellar Solutions. *Soft Matter*, 10(16):2889–2898, 2014.
- [146] E. Fischer and P. T. Callaghan. Is a Birefringence Band a Shear Band? *Europhys. Lett.*, 50(6):803–809, 2000.
- [147] S. M. Fielding. Vorticity Structuring and Velocity Rolls Triggered by Gradient Shear Bands. *Phys. Rev. E*, 76(1):016311, 2007.
- [148] P. Fischer, K. W. Elizabeth, and G. G. Fuller. Shear-Banding Structure Orientated in the Vorticity Direction Observed for Equimolar Micellar Solution. *Rheol. Acta*, 41(1-2):35–44, 2002.
- [149] D. Bonn, J. Meunier, O. Greffier, A. Al-Kahwaji, and H. Kellay. Bistability in Non-Newtonian Flow: Rheology of Lyotropic Liquid Crystals. *Phys. Rev. E*, 58(2):2115–2118, 1998.
- [150] G. M. H. Wilkins and P. D. Olmsted. Vorticity Banding During the Lamellar-to-Onion Transition in a Lyotropic Surfactant Solution in Shear Flow. *Eur. Phys. J. E*, 21(2):133–143, 2006.
- [151] K. Kang, M. P. Lettinga, and J. K.G. Dhont. Is Vorticity-Banding due to an Elastic Instability? *Rheol. Acta*, 47(5-6):499–508, 2008.
- [152] M. A. Fardin, O. Cardoso, B. Lasne, G. Grégoire, J. P. Decruppe, M. Argentina, and S. Lerouge. Taylor-Like vortices in the Shear-Banding Flow of Giant Micelles. *AIP Conf. Proc.*, 1027(July):192–194, 2008.
- [153] P. D. Olmsted and C.-Y. David Lu. Phase Coexistence of Complex Fluids in Shear Flow. *Faraday Discuss.*, 112:183–194, 1999.
- [154] J. K.G. Dhont, M. P. Lettinga, Z. Dogic, T. A.J. Lenstra, H. Wang, S. Rathgeber, P. Carletto, L. Willner, H. Frielinghaus, and P. Lindner. Shear-Banding and Microstructure of Colloids in Shear Flow. *Faraday Discuss.*, 123(1):157–172, 2003.
- [155] K. Kang, M. P. Lettinga, Z. Dogic, and J. K.G. Dhont. Vorticity Banding in Rodlike Virus Suspensions. *Phys. Rev. E.*, 74(2):1–12, 2006.

- [156] J. A. Pathak and S. D. Hudson. Rheo-Optics of Equilibrium Polymer Solutions: Wormlike Micelles in Elongational Flow in a Microfluidic Cross-Slot. *Macromolecules*, 39(25):8782–8792, 2006.
- [157] N. Dubash, P. Cheung, and A. Q. Shen. Elastic Instabilities in a Microfluidic Cross-Slot Flow of Wormlike Micellar Solutions. *Soft Matter*, 8(21):5847, 2012.
- [158] S. J. Haward and G. H. McKinley. Stagnation Point Flow of Wormlike Micellar Solutions in a Microfluidic Cross-Slot Device: Effects of Surfactant Concentration and Ionic Environment. *Phys. Rev. E*, 85(3):031502, 2012.
- [159] S. J. Haward, T. J. Ober, M. S. N. Oliveira, M. A. Alves, and G. H. McKinley. Extensional Rheology and Elastic Instabilities of a Wormlike Micellar Solution in a Microfluidic Cross-Slot Device. *Soft Matter*, 8(2):536–555, 2012.
- [160] S. J. Haward, M. S. N. Oliveira, M. A. Alves, and G. H. McKinley. Optimized Cross-Slot Flow Geometry for Microfluidic Extensional Rheometry. *Phys. Rev. Lett.*, 109(12):1–5, 2012.
- [161] S. Dutta and M. D. Graham. Mechanistic Constitutive Model for Wormlike Micelle Solutions With Flow-Induced Structure Formation. *J. Non-Newton. Fluid Mech.*, 251(November 2017):97–106, 2018.
- [162] R. Gamez-Corrales, J. F. Berret, L. M. Walker, and J. Oberdisse. Shear-Thickening Dilute Surfactant Solutions: Equilibrium Structure as Studied by Small-Angle Neutron Scattering. *Langmuir*, 15(20):6755–6763, 1999.
- [163] J. Ulmius and H. Wennerström. Proton NMR Bandshapes for Large Aggregates; Micellar Solutions of Hexadecyltrimethylammonium Bromide. *J. Magn. Reson.*, 28(2):309–312, 1977.
- [164] J. V. Joshi, V. K. Aswal, and P. S. Goyal. Effect of Sodium Salicylate on the Structure of Micelles of Different Hydrocarbon Chain Lengths. *Phys. B Condens. Matter*, 391(1):65–71, 2007.
- [165] M. Vasudevan, A. Q. Shen, B. Khomami, and R. Sureshkumar. Self-Similar Shear Thickening Behavior in CTAB/NaSal Surfactant Solutions. *J. Rheol.*, 52(2):527–550, 2008.
- [166] T. G. Mason. Estimating the Viscoelastic Moduli of Complex Fluids Using the Generalized Stokes-Einstein Equation. *Rheol. Acta*, 39(4):371–378, 2000.
- [167] T. M. Squires and T. G. Mason. Fluid Mechanics of Microrheology. *Annu. Rev. Fluid Mech.*, 42(1):413–438, 2010.
- [168] P. Schümmer and K.H. Tebel. A New Elongational Rheometer for Polymer Solutions. *J. Non-Newton. Fluid Mech.*, 12(3):331–347, 1983.
- [169] V. M. Entov and E. J. Hinch. Effect of a Spectrum of Relaxation Times on the Capillary Thinning of a Filament of Elastic Liquid. *J. Non-Newton. Fluid Mech.*, 72(1):31–53, 1997.

-
- [170] A.V. Bazilevskii, V.M. Entov, and A.N. Rozhkov. Liquid Filament Microrheometer and Some of Its Applications. In *Third European Rheology Conference and Golden Jubilee Meeting of the British Society of Rheology*, pages 41–43, 1990.
- [171] A. V. Bazilevskii, V.M. Entov, M. M. Lerner, and A. N. Rozhkov. Failure of Polymer Solution Filaments. *Polym. Sci. Ser. A. Chem. Phys.*, 39(3):316–324, 1997.
- [172] A. V. Bazilevskii, V. M. Entov, and A. N. Rozhkov. Breakup of a Liquid Bridge as a Method of Rheological Testing of Biological Fluids. *Fluid Dyn.*, 46(4):613–622, 2011.
- [173] G. H. McKinley. Visco-Elasto-Capillary Thinning and Break-Up of Complex Fluids. *Polymer*, (05):1274–1277, 2005.
- [174] S. L. Anna and G. H. McKinley. Elasto-capillary Thinning and Breakup of Model Elastic Liquids. *J. Rheol.*, 45(1):115–138, 2001.
- [175] C. Clasen, J. P. Plog, W.-M. Kulicke, M. Owens, C. Macosko, L. E. Scriven, M. Verani, and G. H. McKinley. How Dilute are Dilute Solutions in Extensional Flows? *J. Rheol.*, 50(6):849–881, 2006.
- [176] J. Eggers. Nonlinear Dynamics and Breakup of Free-Surface Flows. *Rev. Mod. Phys.*, 69(3):865–930, 1997.
- [177] J. Eggers. Universal Pinching of 3D Axisymmetric Free-Surface Flow. *Phys. Rev. Lett.*, 71(21):3458–3460, 1993.
- [178] Michael P. Brenner, John R. Lister, and Howard A. Stone. Pinching Threads, Singularities and The Number 0.0304. *Phys. Fluids*, 8(11):2827–2836, 1996.
- [179] E. Miller, C. Clasen, and J. P. Rothstein. The Effect of Step-Stretch Parameters on Capillary Breakup Extensional Rheology (CaBER) Measurements. *Rheol. Acta*, 48(6):625–639, 2009.
- [180] L. Campo-Deaño and C. Clasen. The Slow Retraction Method (SRM) for the Determination of Ultra-Short Relaxation Times in Capillary Breakup Extensional Rheometry Experiments. *J. Non-Newton. Fluid Mech.*, 165(23-24):1688–1699, 2010.
- [181] J. Dinic, Y. Zhang, L. N. Jimenez, and V. Sharma. Extensional Relaxation Times of Dilute, Aqueous Polymer Solutions. *ACS Macro Lett.*, 4(7):804–808, 2015.
- [182] D. Sachsenheimer, B. Hochstein, H. Buggisch, and N. Willenbacher. Determination of Axial Forces During the Capillary Breakup of Liquid Filaments – the Tilted CaBER Method. *Rheol. Acta*, 51(10):909–923, 2012.
- [183] M. Raffel, C. E. Willert, F. Scarano, C. J. Kähler, S. T. Wereley, and J. Kompenhans. *Particle Image Velocimetry*. Springer International Publishing, 2018.

- [184] C. D. Meinhart, S. T. Wereley, and M. H. B. Gray. Volume Illumination for Two-Dimensional Particle Image Velocimetry. *Meas. Sci. Technol.*, 11(6):809–814, 2000.
- [185] W. Thielicke and E.J. Stamhuis. PIVlab - Time-Resolved Digital Particle Image Velocimetry Tool for MATLAB (version: 1.41), 2014.
- [186] W. Thielicke and E. J. Stamhuis. PIVlab – Towards User-friendly, Affordable and Accurate Digital Particle Image Velocimetry in MATLAB. *J. Open Res. Softw.*, 2, 2014.
- [187] O. Arnolds, H. Buggisch, D. Sachsenheimer, and N. Willenbacher. Capillary Breakup Extensional Rheometry (CaBER) on Semi-Dilute and Concentrated Polyethyleneoxide (PEO) Solutions. *Rheol. Acta*, 49(11-12):1207–1217, 2010.
- [188] S. Gier and C. Wagner. Visualization of the Flow Profile inside a Thinning Filament During Capillary Breakup of a Polymer Solution via Particle Image Velocimetry and Particle Tracking Velocimetry. *Phys. Fluids*, 24(5):053102, 2012.
- [189] A. Kowalczyk, C. Oelschlaeger, and N. Willenbacher. Visualization of Micro-Scale Inhomogeneities in Acrylic Thickener Solutions: A Multiple Particle Tracking Study. *Polym. (United Kingdom)*, 58:170–179, 2015.
- [190] J. C. Crocker and D. G. Grier. Methods of Digital Video Microscopy for Colloidal Studies. *J. Colloid Interface Sci.*, 179(1):298–310, 1996.
- [191] V. Lutz-Bueno, R. Pasquino, M. Liebi, J. Kohlbrecher, and P. Fischer. Viscoelasticity Enhancement of Surfactant Solutions Depends on Molecular Conformation: Influence of Surfactant Headgroup Structure and Its Counterion. *Langmuir*, 32(17):4239–4250, 2016.
- [192] C. Lin, J. Zhao, and R. Jiang. Nile Red Probing for the Micelle-to-Vesicle Transition of AOT in Aqueous Solution. *Chem. Phys. Lett.*, 464(1-3):77–81, 2008.
- [193] C. Lin and J. Zhao. Nile Red Probing for Sphere-to-Rod-to-Wormlike Micelle Transition in Aqueous Surfactant Solution. *Dye. Pigment.*, 84(3):223–228, 2010.
- [194] J. J. Cardiel, D. Takagi, H.-F. Tsai, and A. Q. Shen. Formation and Flow Behavior of Micellar Membranes in a T-shaped Microchannel. *Soft Matter*, 12(39):8226–8234, 2016.
- [195] P. E. Arratia, C. C. Thomas, J. Diorio, and J. P. Gollub. Elastic Instabilities of Polymer Solutions in Cross-Channel Flow. *Phys. Rev. Lett.*, 96(14):144502, 2006.
- [196] T. T. Perkins, D. E. Smith, and S. Chu. Single Polymer Dynamics in an Elongational Flow. *Science (80-.)*, 276(5321):2016–2021, 1997.
- [197] J. A. Odell and A. Keller. Flow-Induced Chain Fracture of Isolated Linear Macromolecules in Solution. *J. Polym. Sci. Part B Polym. Phys.*, 24(9):1889–1916, 1986.

-
- [198] N. Burshtein, K. Zografos, A. Q. Shen, R. J. Poole, and S. J. Haward. Inertioelastic Flow Instability at a Stagnation Point. *Phys. Rev. X*, 7(4):041039, 2017.
- [199] M. A. Alves. Design of a Cross-Slot Flow Channel for Extensional Viscosity Measurements. In *AIP Conf. Proc.*, volume 1027, pages 240–242, 2008.
- [200] S. J. Haward and G. H. McKinley. Instabilities in Stagnation Point Flows of Polymer Solutions. *Phys. Fluids*, 25(8):083104, 2013.
- [201] S. J. Haward, A. Jaishankar, M. S. N. Oliveira, M. A. Alves, and G. H. McKinley. Extensional Flow of Hyaluronic Acid Solutions in an Optimized Microfluidic Cross-Slot Device. *Biomicrofluidics*, 7(4):1–11, 2013.
- [202] F. Del Giudice, S. J. Haward, and A. Q. Shen. Relaxation Time of Dilute Polymer Solutions: A Microfluidic Approach. *J. Rheol.*, 61(2):327–337, 2017.
- [203] F. J. Galindo-Rosales, M. S. N. Oliveira, and M. A. Alves. Optimized Cross-Slot Microdevices for Homogeneous Extension. *RSC Adv.*, 4(15):7799, 2014.
- [204] S. J. Haward, G. H. McKinley, and A. Q. Shen. Elastic Instabilities in Planar Elongational Flow of Monodisperse Polymer Solutions. *Sci. Rep.*, 6(1):33029, 2016.
- [205] P. C. Sousa, F. T. Pinho, M. S. N. Oliveira, and M. A. Alves. Purely Elastic Flow Instabilities in Microscale Cross-Slot Devices. *Soft Matter*, 11(45):8856–8862, 2015.
- [206] M. Hermans, J. Gottmann, and F. Riedel. Selective, Laser-Induced Etching of Fused Silica at High Scan-Speeds Using KOH. *J. Laser Micro Nanoeng.*, 9(2):126–131, 2014.
- [207] N. Burshtein, S. T. Chan, K. Toda-Peters, A. Q. Shen, and S. J. Haward. 3D-Printed Glass Microfluidics for Fluid Dynamics and Rheology. *Curr. Opin. Colloid Interface Sci.*, 43:1–14, 2019.
- [208] C.-Y. Han and Y.-F. Chao. Photoelastic Modulated Imaging Ellipsometry by Stroboscopic Illumination Technique. *Rev. Sci. Instrum.*, 77(2):023107, 2006.
- [209] S. Nichols, J. Freudenthal, O. Arteaga, and B. Kahr. Imaging with Photoelastic Modulators. In *Proc. SPIE*, volume 9099, page 909912, 2014.
- [210] C. Oelschlaeger, M. Schopferer, F. Scheffold, and N. Willenbacher. Linear-to-Branched Micelles Transition: A Rheometry and Diffusing Wave Spectroscopy (DWS) Study. *Langmuir*, 25(2):716–723, 2009.
- [211] R. G. Larson. The Lengths of Thread-Like Micelles Inferred from Rheology. *J. Rheol.*, 56(6):1363–1374, 2012.
- [212] S. J. Haward, F. J. Galindo-Rosales, P. Ballesta, and M. A. Alves. Spatiotemporal Flow Instabilities of Wormlike Micellar Solutions in Rectangular Microchannels. *Appl. Phys. Lett.*, 104(12):1–6, 2014.

- [213] A. Cortés and M. Valiente. The Effect of a Minimum Amount of Octyl- β -D-Glucoside on Micellar, Nematic, and Hexagonal Phases of the CTAB/Glycerol/Water System. *Colloid Polym. Sci.*, 281(4):319–324, 2003.
- [214] G. D’Errico, D. Ciccarelli, and O. Ortona. Effect of Glycerol on Micelle Formation by Ionic and Nonionic Surfactants at 25°C. *J. Colloid Interface Sci.*, 286(2):747–754, 2005.
- [215] M. Valiente, A.B. Cortés, M. Gradzielski, L. Noirez, and R. Schweins. A SANS Investigation of Micelles in Mixtures of Cetyltrimethylammonium Bromide (CTAB)/octyl- β -d-glucopyranoside (C8G1) in Water/Glycerol Solvent. *Colloids Surfaces A Physicochem. Eng. Asp.*, 375(1-3):117–123, 2011.
- [216] H. Hoffmann and R. Abdel-Rahem. Influence of Co-Solvent on the Rheological Behavior of Aqueous Viscoelastic Surfactant Solutions. *Colloid Polym. Sci.*, 288(6):603–612, 2010.
- [217] L. Böni, P. Fischer, L. Böcker, S. Kuster, and P. A. Rühs. Hagfish Slime and Mucin Flow Properties and Their Implications for Defense. *Sci. Rep.*, 6(1):30371, 2016.
- [218] L. J. Böni, R. Zurflüh, M. Widmer, P. Fischer, E. J. Windhab, P. A. Rühs, and S. Kuster. Hagfish Slime Exudate Stabilization and its Effect on Slime Formation and Functionality. *Biol. Open*, 6(7):1115–1122, 2017.
- [219] L. J. Böni, R. Zurflüh, M. E. Baumgartner, E. J. Windhab, P. Fischer, S. Kuster, and P. A. Rühs. Effect of Ionic Strength and Seawater Cations on Hagfish Slime Formation. *Sci. Rep.*, 8(1):1–12, 2018.
- [220] D. Johansson, M. Stading, C. Diogo-Löfgren, and C. Christersson. Effect of Acid Stimulation on the Dynamic Rheological Properties of Human Saliva. *Annu. Trans. Nord. Rheol. Soc.*, 19:27–31, 2011.
- [221] M. Turcanu, L. F. Tascon, C. Balan, and C. Gallegos. Capillary Breakup Extensional Properties of Whole Human Saliva. In *2015 9th Int. Symp. Adv. Top. Electr. Eng.*, pages 269–274. IEEE, may 2015.
- [222] E. Zussman, A.L. Yarin, and R.M. Nagles. Age-and Flow-Dependency of Salivary Viscoelasticity. *J. Dent. Res.*, 86(3):281–285, 2007.
- [223] C. E Wagner and G. H. McKinley. Age-Dependent Capillary Thinning Dynamics of Physically-Associated Salivary Mucin Networks. *J. Rheol.*, 61(6):1309–1326, 2017.
- [224] D. Briedis, M. F. Moutrie, and R. T. Balmer. A Study of the Shear Viscosity of Human Whole Saliva. *Rheol. Acta*, 19(3):365–374, 1980.

Appendix

List of symbols and abbreviations

Latin symbols

Symbol	Unit	Description
a_0	\AA^2	optimal surface area of surfactant headgroup per molecule
c_{salt}	mM	salt concentration
c_{surf}	mM	surfactant concentration
d	\AA	micelle diameter
d	mm	depth
D	mm	filament diameter
D_0	mm	plate diameter
D_1	mm	initial filament diameter
D_h	mm	hydraulic diameter
D_{min}	mm	minimal filament diameter
D_n	mm	needle diameter
D_p	mm	piston diameter
d_p	μm	particle diameter
G_0	Pa	plateau modulus
G'	Pa	storage modulus
G''	Pa	loss modulus
g	mm s^{-2}	acceleration of gravity
H	mm	immersion depth
h	mm	height
h_f	mm	final displacement
h_i	mm	initial displacement
L	nm	micellar contour length
l_p	nm	persistence length
l_t	\AA	surfactant tail length
M_w	g mol^{-1}	molecular weight
n	-	refractive index
Q	ml min^{-1}	volumetric flow rate
R	-	salt/surfactant ratio
R_a	mm	outer radius
R_i	mm	inner radius

Continued on next page

Symbol	Unit	Description
T	$^{\circ}\text{C}$	temperature
t	s	time
t_c	s	critical time
t_{FIB}	s	time when FIB emerges
t_{fil}	s	filament lifetime
$t_{\text{fil,N}}$	s	filament lifetime, assuming Newtonian flow behavior
t_{ind}	s	induction time
t_m	s	time per measurement point
t_s	ms	strike time
t_{start}	s	start time
U	mm s^{-1}	average flow velocity
V_i	mm^3	initial volume
v	\AA^3	surfactant tail volume
v_p	mm s^{-1}	piston velocity
v_x	mm s^{-1}	velocity component in x direction
v_y	mm s^{-1}	velocity component in y direction
$v_{y,\text{steady}}$	mm s^{-1}	steady velocity in y direction
v_z	mm s^{-1}	velocity component in z direction
w	mm	width
x, y, z	-	Cartesian coordinates

Greek symbols

Symbol	Unit	Description
$\Delta\mu_g^0$	J	standard free energy difference of surfactant aggregate (size g)
δ	-	radii ratio
δ	nm	retardance
δ_s	-	spacing in depth
δt_l	ns	pulse duration laser
δz_m	μm	measurement depth
Γ	mN m^{-1}	surface tension
Γ_i	mN m^{-1}	interfacial tension between surfactant solution and species i
γ	-	deformation
γ_0	-	strain amplitude
γ_c	-	critical deformation
$\dot{\gamma}$	s^{-1}	shear rate
$\dot{\gamma}_c$	s^{-1}	critical shear rate
$\dot{\gamma}_c^*$	s^{-1}	re-entrant critical shear rate in hysteretic regime
$\dot{\gamma}_{\text{nom,C}}$	s^{-1}	nominal shear rate CaBER
$\dot{\gamma}_{\text{nom,O}}$	s^{-1}	nominal shear rate OSCER
$\dot{\gamma}_{\text{wall}}$	s^{-1}	wall shear rate
ε	-	strain
ε_c	-	critical strain
$\dot{\varepsilon}$	s^{-1}	elongation rate
$\dot{\varepsilon}_c$	s^{-1}	critical elongation rate
$\dot{\varepsilon}_{\text{nom,C}}$	s^{-1}	nominal elongation rate CaBER
$\dot{\varepsilon}_{\text{nom,O}}$	s^{-1}	nominal elongation rate OSCER
η	Pa s	shear viscosity
η^+	Pa s	transient shear viscosity
η_0	Pa s	zero shear viscosity
η_e	Pa s	extensional viscosity
$\eta_0^{\text{surf}}/\eta_0^{\text{oil}}$	Pa s	viscosity ratio between surfactant solution and oil
Θ	-	numerical prefactor
Θ	-	angle of high refractive index
θ	-	light collecting angle
Λ_f	-	final aspect ratio
λ	s	relaxation time
λ_0	nm	wavelength of light in vacuum
λ_{break}	s	micellar breakage time
λ_l	nm	laser wavelength
λ_{LED}	nm	LED wavelength
λ_e	s	elongational relaxation time
λ_{rep}	s	micellar reptation time
λ_s	s	shear relaxation time
ρ	g cm^{-3}	density
τ	Pa	shear stress

Continued on next page

Symbol	Unit	Description
ω	rad s ⁻¹	angular frequency
ω_c	rad s ⁻¹	cross-over frequency

Abbreviations

Abbreviation	Meaning
<i>Bo</i>	Bond number
CABER	capillary breakup elongational rheometer
CCD	charge-coupled device
CMC	critical micelle concentration
CMC ₁	first critical micelle concentration
CMC ₂	second critical micelle concentration
CPyCl	hexadecylcetylpyridinium chloride
CR	controlled rate
CS	controlled stress
CTAB	hexadecyltrimethylammonium bromide
CTAC	hexadecyltrimethylammonium chloride
CTAT	hexadecyltrimethylammonium p-toluene sulfonate
DoS	dripping-onto-substrate
EHAC	erucyl bis(2-hydroxyethyl) methylammonium chloride
EIS	elongation-induced structure
<i>El</i>	elasticity number
FENE	finitely-extensible non-linear elastic
FIB	flow-induced birefringence
FIS	flow-induced structure/state
FiSER	filament stretching elongational rheometer
FISP	flow-induced structured phase
LVE	linear viscoelastic
<i>NA</i>	numerical aperture
NaCl	sodium chloride
NaOA	sodium oleate
NaSal	sodium salicylate
NaTos	sodium p-toluenesulfonate
NH ₄ Cl	ammonium chloride
NMR	nuclear magnetic resonance
OS CER	optimized-shape cross-slot extensional rheometer
OTAB	octyltrimethylammonium bromide
PDMS	polydimethylsiloxane
PEO	poly(ethylene oxide)
PIV	particle image velocimetry
PP	packing parameter
<i>Re</i>	Reynolds number
SALS	small-angle light scattering
SANS	small-angle neutron scattering
SIS	shear-induced structure
SRM	slow retraction method
SAOS	small-amplitude oscillatory shear
TEM	transmission electron microscopy

Continued on next page

Abbreviation	Meaning
<i>Tr</i>	Trouton ratio
TTABr	tetradecyltrimethylammonium bromide
<i>Wi</i>	Weissenberg number
<i>Wi_c</i>	critical Weissenberg number
VCM	Vasquez-Cook-McKinley (model)
WLM	wormlike micelles